מכון ויצמן למדע
WEIZMANN INSTITUTE OF SCIENCE

Thesis for the degree
Doctor of Philosophy

עבודת גמר (תזה) לתואר
דוקטור לפילוסופיה

Submitted to the Scientific Council of the
Weizmann Institute of Science
Rehovot, Israel

מוגשת למועצה המדעית של
מכון ויצמן למדע
רחובות, ישראל

By
Tomas Sikorsky

מאת
תומס סיקורסקי

Quantum control of inelastic processes in atom-ion systems

Advisor:
Roee Ozeri

מנחה:
רועי עוזרי

May 2018

מאי 2018

This thesis is dedicated to all people who contributed to it, and to my son Ernest.

Prologue

My first experience with physics research occurred during my undergraduate studies. In 2009 I spent whole summer in Claredon laboratory where I was playing with High-temperature superconductors. Even though we have not discovered anything profound, the fact that I was waking up in the morning and looking forward to going to the lab, convinced that experimental physics is what I should do. After the rainy English summer, I continued my studies in Prague where started to concentrate on atomic physics. I got fascinated by NMR spectroscopy. By its elegance and versatility with which NMR sequences are used to probe molecular and intermolecular interactions through each individual nucleus. After four years working with NMR, I began to feel that NMR is too well-established and I wanted to work on something more exotic. I contacted Roee Ozeri who was at the time building the lab to study ultracold atom-ion interactions. After my visit to Israel, we both agreed, and I joined his research group as a Ph.D. student. The rest of the story is told in this thesis.

Acknowledgments

Almost five years ago I joined the Roee's group. I spend my first year separated from the real lab in room 150 where I was building the Sr MOT. This was the most important year of my Ph.D. I refreshed parts of the high-school physics that I was not using for several years and I improved all my soft skills that were terrible at the time. Here I want to thank Nitzan Akerman who supervised me during this year.

After my first year, we disassembled the Sr MOT and moved the components into the real lab. Here I started to work the most important person of my Ph.D. Ziv Meir. Ziv is a pioneer of atom-ion research in Middle East, and he was already building this lab for two years. Immediately we started to work on combining the Ziv's experimental setup with Rb MOT that was built by Yoni Dallal. Our first challenge was a broken screw that we had to remove from Ziv's vacuum chamber to connect it. This situation looked scary; we had to drill the nut out without breaking the vacuum. But when I saw Guy Han dealing with the problem, I knew that chamber is in good hands, and it is going to be fixed. And it was. Here I want to thank Guy for his fast and effective way of machining all the lab components. Having an effective workshop doorstep away dramatically accelerated our experimental work. I also want to thank other lab members Ruti and Meirav for locking all the lasers when I was running experiment remotely. Special thanks go to administration stuff: Perla, Malka, and Rachel who take care of all the administrative problems and allowed us to fully concentrate on science. Also to Rosti for his original solutions to all technical problems that we had. But mainly to Roee, who is a great supervisor. For his style of leading the research, which allows students to work independently without pushing but with his intensive support. What I appreciated the most was that I could invade his office almost anytime and he always immediately gave me his full attention.

In the end, I want to thank my family. To my parents who raised me in a way they did and to Katka with who we will raise our son Ernest even better.

Contents

List of Figures

Abstract

Almost everything that we know about the microscopic world came from scattering experiments. Collisions between gold atoms and α particles led to the discovery of atomic structure. Collisions between heavy atoms are used to produce and study atoms at the end of the periodic table. High energy collisions in accelerators are used to understand the subatomic structure.

This thesis is about collisions between ultracold atoms and ions. Here, we use the scattering experiments to explore atom-ion interactions. Understanding atom-ion collisions is essential for the new growing field of hybrid systems. These systems are a promising candidate to for quantum chemistry studies and quantum simulations.

In our experiment, we study the spin evolution and chemical reactions of ultracold $^{88}\mathrm{Sr}^+$ ion immersed into a bath of ultracold $^{87}\mathrm{Rb}$ atoms. These experiments were performed in a hybrid setup [46] which overlaps a single of few Sr^+ ions trapped in a Paul trap and a cloud of Rb atoms trapped in an optical dipole trap. We exploit the idea that atoms and ions can be trapped using a mutually independent trapping mechanism which can be spatially overlapped. This allows us to trap and manipulate the atoms and ions independently.

For atom-ion mixtures, prior to this work, there were no experimental realizations of spin coherent or spin conserving collisions [55]. Here we show that Rb atoms can be used for collisional pumping of the Sr^+ ion spin state. The spin state of the ion becomes polarized according to the hyperfine state of the atomic bath after few Langevin collisions. This is an important observation because most of the ultracold atom-ion proposals require atom-ion collisions that conserve the spin angular momentum. Our results demonstrate spin manipulation through spin-exchange collisions which conserve the total spin. Furthermore, we used the spin-exchange collisions to perform ground-state ultracold controlled chemistry between the polarized ion and atoms. By controlling the hyperfine states of the atomic bath and bath-polarized ion, we can change the ratio of the collisions which are projected to a singlet or triplet manifold. Due to Pauli Exclusion Principle, the charge exchange reaction is only allowed for the singlet manifold $\mathrm{Sr}^+ + \mathrm{Rb} \to \mathrm{Sr} + \mathrm{Rb}^+$. We use this effect to control the charge exchange reaction

rates by controlling the hyperfine states of the atomic bath. We also show that the charge exchange reaction rates are temperature dependent.

Chapter 1

Introduction

Hybrid systems which combine ultracold atoms with laser-cooled ions in a single experimental setup benefit from the knowledge accumulated in these highly developed fields of research.

For ultracold atoms, the active control of collisions is a very successful research field. The developed tools allow for controllability with, e.g., magnetic fields [10], light fields [38] and spin-state manipulation of the colliding particles [52]. The control of chemical reactions between ultracold atoms and ions is a young research field. Recently, the collision energy [30] and the ion electronic state [56, 32, 28] were used to control atom-ion interactions.

For laser-cooled ions, the most accurate optical single-ion clock worldwide [35] and the quantum processor with the largest number of qubits [48] are possible thanks to the control of their quantum state. This level of control paved the way for studies of ultracold systems containing both atoms and ions. Atom-ion collisions are much harder to control due to their long interaction range. Atom-ion experiments were performed in several laboratories worldwide.

The research of atom-ion collisions has entered the ultracold regime. Since the original proposal [12], laser-cooled atom-ion hybrid systems have matured into a successful field of research, and many new phenomena have been observed. In recent years several research groups around the world have reached experimental maturity [80, 8, 31, 57, 61] and many goals have been achieved. For example, sympathetic and swap cooling of ions using ultracold atoms [43, 57], three-body recombination [31], non-equilibrium dynamics and the emergence of power-law energy distribution [45], bifurcation of ion energies [61], spin-exchange between atoms and ions [23, 64], controlled charge-exchange reactions with a selective spin-state preparation [64] and many more.

These achievements pave way for future quantum physics proposals, such as emulating solid state physics where ions crystal is used as a lattice and atoms form a band-structure [6]. Another proposal is to use atom-ion long range interaction to implement a double-well bosonic Josephson junction [25]. Spin-dependent atom-ion interactions opens a door for atom-ion quantum gates [21].

The attractive interaction between atoms and ions scales as $1/r^4$ due to long-range polarization potential which extends to 100's of nanometers. The long-range interaction can lead to the formation of quantum macroscopic objects [13] that would preserve quantum features such as Feshbach resonances [67] or shape-resonances [14]. At close distance, the potential energy curves [4] exhibit various properties which allow for quantum control of chemical reactions [64]. Even though this research field is promising, the experiments are currently in elementary stages. The complexity of the combined hybrid systems constrains current experimental research.

The above proposals rely on the atom-ion collisions to occur in the ultracold regime where only single or few partial waves contribute to collisions. Major and Demhelt have shown that atom-ion system with atoms heavier than ions is unstable in a Paul trap [54, 19]. The instability emanates from non-equilibrium dynamics where even collisions with the cold atom far from the trap center perturbs the ion's Mathieu trajectory and could heat the ion [19]. This effect is caused by the spatial gradient of the oscillating electric fields. These fields cause the ion's micromotion when it is displaced from the trap center [5]. Even if the ion is prepared in the center of the trap before the collision, unless the atoms are much lighter than the ion, the collision will displace the ion from the trap center. The work of Ziv Meir has shown that in our system, where atom and ion have similar mass the ion is stable and collisions only cause minor heating [45]. The ion energy reaches $\sim 1\,\mathrm{mK}$ after ~ 10 collisions and few mK after hundreds of collisions. Even though we were not able to reach the ultracold regime in our system due to mass ratio, modest heating rates allowed us to perform several experiments studying spin dynamics and spin-controlled charge-exchange reactions.

In this thesis, we achieved spin-controlled inelastic (spin-exchange) and chemical (charge-exchange) processes. Spin-exchange collisions between the ion and spin-polarized atoms polarize the ion's spin parallel to the atomic spin. We achieved ~90% spin polarization due to the small spin-relaxation. This allowed us to study various spin processes.

We measured and calculated the spin-exchange and spin-relaxation rates with various hyperfine states of the Rb atoms. We also measured the dependence of endoenergetic spin-exchange on a magnetic field. We found that spin-exchange rate we measured deviates from the predictions of random-phase approximation.

After we succeeded to control and maintain the spin of the ion during multiple collisions, the next step was to study spin-controlled chemistry. Charge-exchange collisions involving electron transfer are only allowed for $(\mathrm{RbSr})^+$ colliding in the singlet manifold. Initializing the atoms in various spin states affects the overlap of the collision wave function with the singlet molecular manifold and therefore also the reaction rate. Our observations agree with theoretical predictions.

Chapter 2

Atom-ion physics

In 1975 Hansch and Schawlow [29] proposed that laser light can be used to cool neutral atoms. The early experiments have been very successful, which started a new field of laser cooling and trapping of atoms. Laser-cooled atoms are behind many scientific discoveries including atomic clocks, BEC [3], quantum information technologies [24], atomic interferometry [70] and atom lithography [73]. At the same time in 1975, Wineland and Dehmelt proposed the use of optical cooling of ions in an electromagnetic trap [74]. Three years later two research groups independently reported the first experimental observation of laser-cooled trapped Ba+ and Mg+ ions [49, 75]. These two fields have become important for atomic physics during last two decades of the 20th century. In the early 2000s, Cote and coworkers proposed experiments with laser-cooled ions and ultracold atoms. The proposals include charge transfer [10], collision dynamics [11] and the formation of mesoscopic molecular ions in Bose-Einstein Condensates [12]. Later in 2005 Smith and co-workers proposed an experimental realization of a hybrid trap for both atoms and ions at cold temperatures [13]. Since then hybrid experimental setups have been developed in several laboratories. In these setups, atoms can act as a cold buffer, which can lead to a sympathetic cooling of the ions [14]. Atoms can also be used to manipulate the internal states of the ions, or they can induce chemical reactions. On the other hand, the ion can be used as a charge or spin impurity in an ultracold atomic gas. The ions are also used as are action center for a controlled creation of cold molecules [15].

2.1 Elastic atom-ion collisions

Because electrons which are the carriers of the negative charge in the atom are bound to the positive nucleus in a spherically symmetric potential, the atoms do not possess a permanent dipole moment. In the ground electronic state, the charge distribution is spherically symmetric and all higher moments vanish. In this case, the long-range part of the interaction potential can be expressed as:

$$V(r) = -\frac{C_4}{2r^4} \tag{2.1}$$

C_4 is the leading order term and represents an interaction between the electric field of an ion and the induced dipole moment of an atom. The ion generates an electric field on the atom $\boldsymbol{\varepsilon}(\mathbf{r}) = \frac{e}{4\pi\epsilon_0|\mathbf{r}|^2}\hat{\mathbf{r}}$. This field induces an electric dipole moment $\mathbf{p} = \alpha\boldsymbol{\varepsilon}$. Here, $\mathbf{r}$ is the vector between the atom and the ion, e is the electron charge, ϵ_0 is the permittivity of vacuum, and α is the polarizability of the atom ($\alpha_{Rb} = 5.2 \times 10^{-39}\,\mathrm{C\,m^2\,V^{-1}}$)[steck2001rubidium]. This leads to an attractive force between the atom and ion, $\mathbf{f} = \mathbf{p}\cdot\nabla\boldsymbol{\varepsilon} = \alpha\boldsymbol{\varepsilon}\cdot\nabla\boldsymbol{\varepsilon} = \frac{1}{2}\alpha\nabla(\boldsymbol{\varepsilon}^2)$,

$$\mathrm{V}(r) = -\int_{-\infty}^{r} \mathbf{f}\cdot d\mathbf{r} = -\frac{1}{2}\alpha\boldsymbol{\varepsilon}^2 = -\frac{1}{2}\mathrm{C}_4/r^4. \tag{2.2}$$

Here, $\mathrm{C}_4 = \frac{\alpha e^2}{(4\pi\epsilon_0)^2} = 1.1 \times 10^{-56}\,\mathrm{J\,m^4}$ for Rb.

2.1.1 Classical treatment

During a collision, other than the polarization potential attraction, also the angular momentum repulsive term $\frac{l^2}{2\mu r^2}$ needs to be considered. Here $\mu = \frac{m_1 m_2}{m_1+m_2}$ is the reduced mass of the atom-ion system, and l is a classical angular momentum $l = \mu r^2\dot{\phi} = \mu v b$, where v is the velocity in the center-of-mass frame $v = \sqrt{\frac{2E}{\mu}}$.

$$b_c = \left(\frac{2\mathrm{C}_4}{E}\right)^{\frac{1}{4}} \tag{2.3}$$

Classically, the presence of this centrifugal repulsion forms a centrifugal barrier. The centrifugal barrier position is given by $r_{\text{barrier}} = \sqrt{\frac{2}{l(l+1)}}r^*$ with $r^* = \sqrt{\frac{\mathrm{C}_4\mu}{\hbar^2}}$. The centrifugal barrier height is given by $\mathrm{E}_{\text{barrier}} = \frac{1}{4}l^2(l+1)^2\mathrm{E}^*$ with $\mathrm{E}^* = \frac{\hbar^2}{2\mu r^{*2}}$. For Sr^+/Rb system r^*=265 nm and E^*=80 nK. This results into two scattering modes. If an impact parameter b is below the critical impact parameter $b < b_c$, then outgoing particles are directed almost isotropically. These collisions are called Langevin collisions. The scattering cross-section of Langevin collisions is:

$$\sigma_{\mathrm{L}} = \pi b_c^2 = \pi\sqrt{\frac{2\mathrm{C}_4}{E}}, \tag{2.4}$$

and the corresponding Langevin rate is energy independent:

$$\Gamma_{\mathrm{L}} = n\sigma_{\mathrm{L}}v = 2\pi\sqrt{\frac{\mathrm{C}_4}{\mu}}n. \tag{2.5}$$

Here, n is the atoms density.

On the other hand, if $b > b_c$, then the incoming particle trajectories are only slightly modified. These collisions are called glancing collisions.

2.1.2 Quantum treatment

For an exact description of a collision process, the classical description is not sufficient. First, the potential diverges at $r \to 0$, and one needs to calculate a hard-core short-range repulsion. Second, when temperatures reach μK and lower, only several partial waves contribute to scattering cross-section, and quantum effects become important. The s-wave regime occurs if the energy of the collision energy is below 80 nK and only collisions with zero angular momentum (l=0) contribute to scattering processes.

The Schrödinger equation for the atom and ion interacting through a spherically symmetric potential[Equation 2.1] after a transformation into a center-of-mass reference frame takes the form:

$$\left(-\frac{\hbar^2}{2\mu}\frac{\partial^2}{\partial r^2} + \frac{\hbar^2}{2\mu}\frac{l(l+1)}{r^2} + \mathrm{V}\,(r)\right) u_{l,m}(r) = E u_{l,m}(r). \tag{2.6}$$

Here, $u_{l,m}(r)$ is the radial part of the solution $\Psi(r) = \sum_{l=0}^{\infty}\sum_{m=-l}^{m=l} Y_l^m(\theta,\phi)\frac{u_{l,m}(r)}{r}$, $\Psi(r)$ is the one body part of the wavefunction $\Psi(\mathbf{r}_1, \mathbf{r}_2) = e^{i\mathbf{k}\mathbf{r}_{\mathrm{cm}}}\Psi(r)$ with r as a inter nuclei distance scalar and l is the angular momentum of the atom-ion wave function.

The effective potential consists of the interaction potential Equation 2.1 summed with another term which acts like a centrifugal barrier for wave functions with angular momentum (see Fig. Figure 2.1).

2.1.3 The semi-classical treatment

Most of the processes described in this thesis require the electronic wavefunctions of atom and ion to overlap section 2.2. Thus the Langevine collision is always a prerequisite for them. However, heating and cooling dynamics section 2.4 is slightly modified by glancing collisions. The glancing collision rate is not energy independent. A semi-classical theory can be used to treat these collisions. First, we define a threshold angular momentum number L which determines the highest angular momentum partial wave that penetrates the centrifugal barrier for a given energy. For large $l > 10$ the height of the centrifugal barrier is $E_{barrier} \approx \frac{l^4\hbar^4}{8\mu^2 C_4}$. Which gives the threshold angular momentum to be:

$$L = \tfrac{1}{\hbar}(8\mu^2 C_4 E)^{1/4}. \tag{2.7}$$

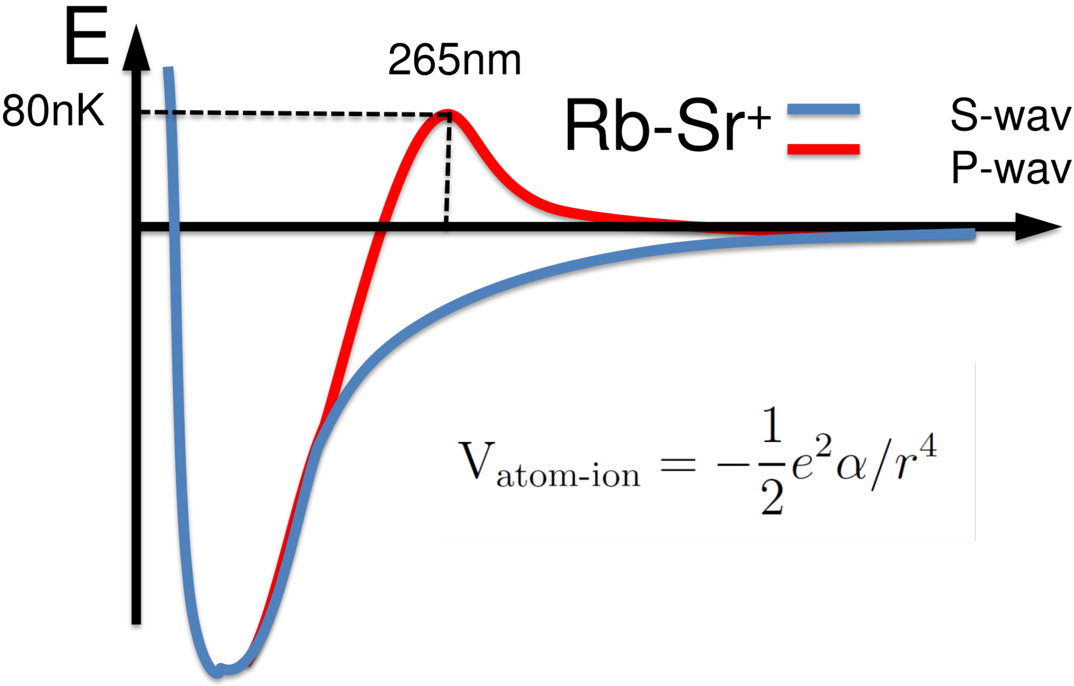

Figure 2.1: Ion-atom interaction potential vs. internuclear separation for s-wave (l=0) and p-wave (l=1) scattering.

Semi-classical approximation treats contributions from $l > L$ and $l < L$ partial waves separately. For $l < L$ we need to know the shape of the short repulsive potential. Since we are calculating contributions from many partial waves, we can assume that phase shifts are distributed homogeneously between $0..2\pi$, and we can replace $\sin^2(\phi_l) = {}^1\!/_2$. The resulting cross-section is:

$$\sigma^{l<L}_{elastic} = \tfrac{4\pi}{k^2} \sum_{l=0}^{l<L} (2l+1) \sin^2 \phi_l = \frac{2\pi L^2}{k^2}. \tag{2.8}$$

Which gives twice the geometrical cross section Equation 2.4. This is called shadow scattering. For collisions with $l > L$ we can approximate the phase shift with [12]:

$$\phi^{l>L}_{l,semi} \approx -\frac{\mu}{\hbar^2} \int_{r_0}^{\infty} \frac{\frac{C_4}{2r^4}}{\sqrt{k^2 - \frac{l+\frac{1}{2}}{r^2}}} \mathrm{d}r = \frac{E\pi\mu^2 C_4}{4l^3\hbar^4}, \tag{2.9}$$

where $r_0 = \sqrt{\frac{l^2}{4E\mu} \pm \sqrt{\frac{l^4}{16E^2\mu^2} - \frac{C_4}{2E}}}$. This semi-classical phase shift gives us following cross-section:

$$\sigma^{l>L}_{elastic} \approx \frac{4\pi}{k^2} \int_{l=L}^{\infty} 2l\phi_{l,semi} \mathrm{d}l = \frac{\pi^3 L^2}{8k^2}. \tag{2.10}$$

This treatment is valid as long as $\phi_{l,semi} < \frac{\pi}{4}$, which is usually valid because the wavefunction does not penetrate the centrifugal barrier for a glancing collisions and phase acquired is very small. Using the Equation 2.8, this condition can be expressed as:

$$l > l_{min} = \left(\frac{\hbar^4}{\mu^2 C_4 E} \right)^{1/3} \tag{2.11}$$

Outside the s-wave regime, we sum Equation 2.8 and Equation 2.10 to obtain the total scattering cross-section:

$$\sigma_{elastic}(E) = \pi \left(\frac{\mu C_4^2}{E\hbar^2} \right)^{1/3} \left(1 + \frac{\pi^2}{16} \right). \tag{2.12}$$

The total elastic cross-section in semi-classical approximation scales as $\sigma \propto E^{1/3}$ as opposed to the Langevin rate which scales as $\sigma \propto E^{1/2}$. Besides energy, it depends on the polarizability and on the masses of colliding particles.

2.2 Inelastic atom-ion collisions

In the previous section, we treated the case where two particles do not change their internal states during a collision. Now we turn to describe the case of inelastic collisions.

The entrance channel of our system is a Sr^+ ion and a Rb atom in the electronic ground state (5S). Exchange interaction splits this channel into two channels at close inter-molecular separation of $< 30\,\mathrm{a}_0$. These channels correspond to the singlet configuration for the $^1\Sigma_0^+$ channel and a triplet configuration for the $^3\Sigma_0^+$ channel. As a result of this splitting, collisions can change internal quantum states of the particles. These are inelastic collisions and classical theory cannot account for them. These collisions can be different such as

- $\mathrm{Rb} + \mathrm{Sr}^+ \rightarrow \tilde{\mathrm{Rb}}^+ + \tilde{\mathrm{Sr}}$ spin-exchange
- $\mathrm{Rb} + \mathrm{Sr}^+ \rightarrow \mathrm{Rb}^+ + \mathrm{Sr}$ charge exchange
- $\mathrm{Rb} + \mathrm{Sr}^+ \rightarrow (\mathrm{RbSr})^+$ molecule formation

To calculate these processes a quantum treatment is needed to solve the atom-ion energy energy potentials. Such calculations have been done for various atom-ion systems. The results for $(\mathrm{RbSr})^+$ system can be found in [4] and are shown in Figure 2.2. From these potential curves we can qualitatively understand the various inelastic processes in $(\mathrm{RbSr})^+$ atom-ion system.

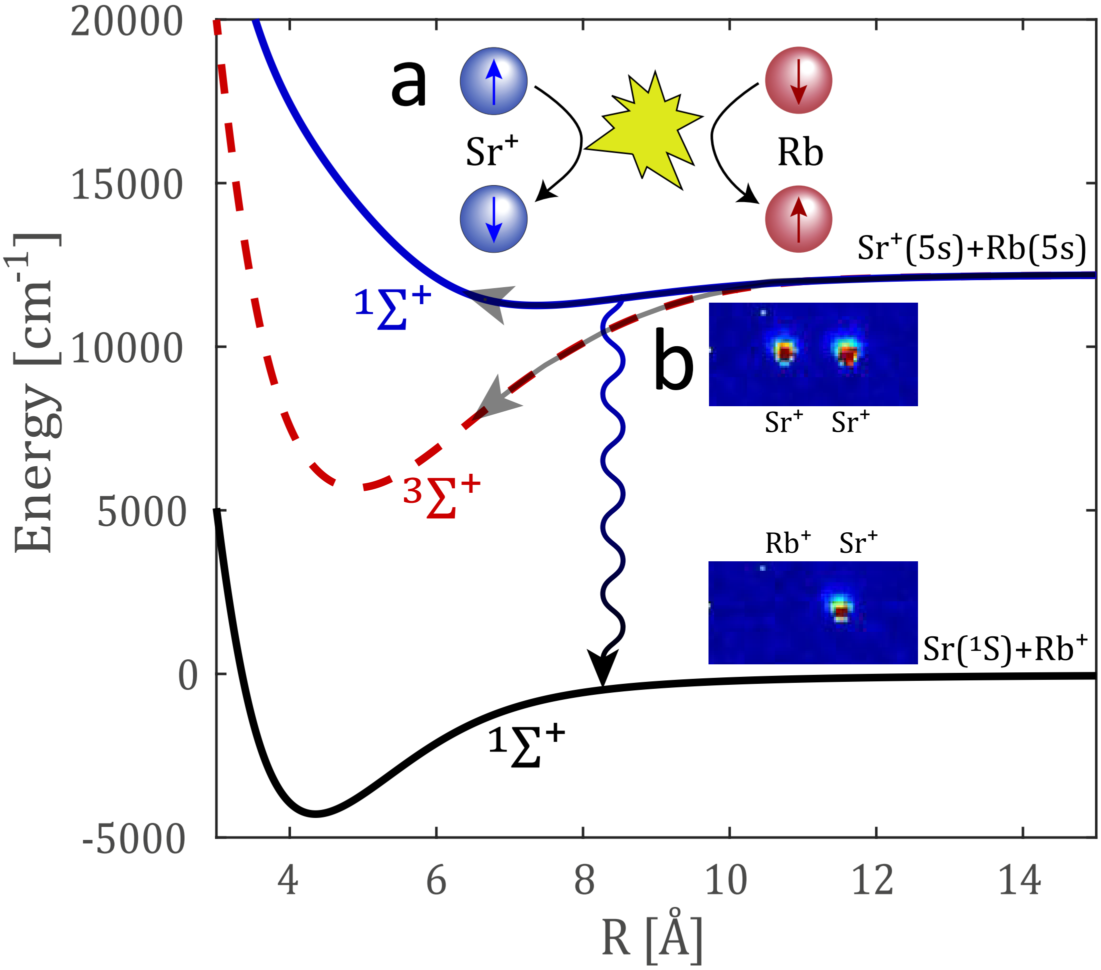

Figure 2.2: Potential energy curves of relevant states. The entrance channel is not a ground state of $(\mathrm{RbSr})^+$. During a collision, asymptotic atomic state (Sr^+(5s)+Rb(5s)) is split into a superposition of singlet $1\sigma^+$ (blue) and triplet state $3\sigma^+$ (red). Pictorial representations of (a) spin-exchange and (b) charge-exchange are shown. Only a singlet state can undergo charge-exchange and decay to the ground state $1\sigma^+$ (black). The energy potential curve calculations ignore the hyperfine interaction of the electrons with the nuclear spin.

2.2.1 The singlet and triplet states of two spin-1/2 particles

Consider an interaction of two distinguishable particles with spin-1/2. The spin state is defined by a pair of commuting operators, such as $[\hat{\mathbf{S}}^2, \hat{S}_z] = 0$. Their eigenvalues are $\hat{\mathbf{S}}^2 |s,m\rangle = \hbar^2 s(s+1) |s,m\rangle$ and $\hat{S}_z |s,m\rangle = \hbar m |s,m\rangle$. The eigenvalues for a spin 1/2 particle are $m = \pm\frac{1}{2}$ and eigenvectors are $|\frac{1}{2}, \frac{1}{2}\rangle = |{\uparrow}\rangle$ and $|\frac{1}{2}, -\frac{1}{2}\rangle = |{\downarrow}\rangle$. The exchange interaction between two spin 1/2 particles is:

$$\hat{\mathcal{H}}^{exch} \propto \hat{\mathbf{S}}_{(1)} \cdot \hat{\mathbf{S}}_{(2)} \tag{2.13}$$

Therefore, the single particle states $|{\uparrow}\rangle$ and $|{\downarrow}\rangle$ are not eigenstates during a collision. We need to define a new operator representing total angular momentum of both particles $\hat{\mathbf{S}}_T = \hat{\mathbf{S}}_{(1)} + \hat{\mathbf{S}}_{(2)}$. The total angular momentum operator squared $\hat{\mathbf{S}}_T^2$ can be written as:

$$\hat{\mathbf{S}}_T^2 = 2 \cdot \hat{\mathbf{S}}_{(1)} \cdot \hat{\mathbf{S}}_{(2)} + \text{constant}. \tag{2.14}$$

This means that when we neglect Zeeman splitting and spin-orbit coupling the eigenvalues of the $\hat{\mathbf{S}}_T^2$ operator are good quantum numbers during a collision. It can be shown that the following set of operators commute: $\hat{\mathbf{S}}_T^2$, $\hat{S}_{T,z}$, $\hat{\mathbf{S}}_{(1)}^2$, $\hat{\mathbf{S}}_{(1)}^2$. Their eigenstates can be obtained as a linear combination of product states $|s_1, m_1\rangle |s_2, m_2\rangle$:

$$|S, m, s_1, s_2\rangle = \sum_{m_1+m_2=m} c_{m_1,m_2,m}^{s_1,s_2,S} |s_1, m_1\rangle |s_2, m_2\rangle . \tag{2.15}$$

The expansion coefficients $c_{m_1,m_2,m}^{s_1,s_2,S}$ are called Clebsch-Gordan coefficients. The total angular momentum has eigenvalues $S = 1$ (triplet) and $S = 0$ (singlet) and its projection along the magnetic field is $|m| =\leq S$. This results in four possible eigenstates:

$$\begin{aligned}
|1,1\rangle &= |{\uparrow}\rangle \otimes |{\uparrow}\rangle = |{\uparrow\uparrow}\rangle \\
|1,0\rangle &= \frac{1}{\sqrt{2}} \left(|{\uparrow}\rangle \otimes |{\downarrow}\rangle + |{\downarrow}\rangle \otimes |{\uparrow}\rangle \right) = \frac{1}{\sqrt{2}} \left(|{\uparrow\downarrow}\rangle + |{\downarrow\uparrow}\rangle \right) \\
|1,-1\rangle &= |{\downarrow}\rangle \otimes |{\downarrow}\rangle = |{\downarrow\downarrow}\rangle \\
|0,0\rangle &= \frac{1}{\sqrt{2}} \left(|{\uparrow}\rangle \otimes |{\downarrow}\rangle - |{\downarrow}\rangle \otimes |{\uparrow}\rangle \right) = \frac{1}{\sqrt{2}} \left(|{\uparrow\downarrow}\rangle - |{\downarrow\uparrow}\rangle \right)
\end{aligned} \tag{2.16}$$

We will use the following molecular term symbol notation, ${}^{2S+1}\Lambda_{\Sigma}^{(\pm)}$, where S is the total spin, Λ is the projection of the orbital angular momentum along the internuclear axis, Σ is the projection of the total angular momentum along the internuclear axis and $(\pm)$ is the reflection symmetry along an arbitrary plane containing the internuclear axis.

2.2.2 Spin-exchange

Because we perform experiments in the electronic ground state of both species (5S), and charge exchange is extremely rare, we are interested in the spin state evolution during collisions. Spin-exchange collisions are collisions where the electronic spin states of the valence electrons of Rb atoms and Sr^+ ion are interchanged. Because the total spin number m is a good quantum number, it remains unchanged. We are interested in spin-exchange collisions $\mathrm{Rb}_\uparrow + \mathrm{Sr}^+_\downarrow \leftrightarrow \mathrm{Rb}_\downarrow + \mathrm{Sr}^+_\uparrow$. The physical origin of the spin-exchange is that when ion and atom spins are prepared in a $\langle\downarrow|_{\mathrm{Sr}^+}\langle\uparrow|_{\mathrm{Rb}}$ or $\langle\uparrow|_{\mathrm{Sr}^+}\langle\downarrow|_{\mathrm{Rb}}$, such a state is projected into a superposition of ${}^1\Sigma_0^+$ and ${}^3\Sigma_0^+$ states. This is allowed because these states are not eigenstates of a $\hat{\mathcal{H}}^{exch}$. They evolve at different rates during a collision. The phase difference between singlet and triplet parts of the wavefunction after a collision is:

$$\phi_{s-t} = \int \frac{V_s - V_t}{\hbar} \mathrm{d}t, \tag{2.17}$$

Here, V_t is the PEC of ${}^3\Sigma_0^+$ state and V_s is the PEC of ${}^1\Sigma_0^+$ state.

The cross-section for the spin-exchange is given by [16, 15]:

$$\sigma_{exch} = |\langle\uparrow\downarrow|\hat{\mathbf{S}}_{(1)} \cdot \hat{\mathbf{S}}_{(2)}|\downarrow\uparrow\rangle|^2 \frac{4\pi}{k^2} \sum_{l=0}^{\infty} (2l+1)\sin^2(\phi_{s-t}), \tag{2.18}$$

where the matrix element is:

$$\langle\uparrow\downarrow|\hat{\mathbf{S}}_{(1)} \cdot \hat{\mathbf{S}}_{(2)}|\downarrow\uparrow\rangle = \frac{1}{\sqrt{2}}(\langle 1,0| - \langle 0,0|) \cdot \frac{1}{\sqrt{2}}\left(\frac{1}{4}|1,0\rangle - \frac{3}{4}|0,0\rangle\right) = \frac{1}{2} \tag{2.19}$$

In Equation 2.19 we used the fact that $\hat{\mathbf{S}}_{(1)} \cdot \hat{\mathbf{S}}_{(2)} = \frac{1}{2}\left(\hat{\mathbf{S}}^2 - \hat{\mathbf{S}}^2_{(1)} - \hat{\mathbf{S}}^2_{(2)}\right)$ where $\hat{\mathbf{S}} = \hat{\mathbf{S}}_{(1)} + \hat{\mathbf{S}}_{(2)}$. The eigenvalue of $\hat{\mathbf{S}}^2$ operator is 1 for a triplet state and 0 for singlet. Eigenvalues for $\hat{\mathbf{S}}^2_{(1)}$ and $\hat{\mathbf{S}}^2_{(2)}$ operators are $\frac{3}{4}$ for both $|\downarrow\rangle$ and $|\uparrow\rangle$.

The Equation 2.19 can also be derived with raising $\hat{\mathbf{S}}_+$ and lowering $\hat{\mathbf{S}}_-$ operators formalism. These operators are defined as $\hat{\mathbf{S}}_x = \frac{1}{2}\left(\hat{\mathbf{S}}_+ + \hat{\mathbf{S}}_-\right)$ and $\hat{\mathbf{S}}_y = \frac{1}{2i}\left(\hat{\mathbf{S}}_+ - \hat{\mathbf{S}}_-\right)$. The only non-vanishing matrix elements are those where both operators flip the spin. Therefore we have to solve the following equation:

$$\langle\uparrow\downarrow|\frac{1}{2}\hat{\mathbf{S}}_{+,(1)} \cdot \hat{\mathbf{S}}_{-,(2)}|\downarrow\uparrow\rangle = \frac{1}{2}. \tag{2.20}$$

Plugging this result in Equation 2.18 we get the spin-exchange cross-section:

$$\sigma_{exch} = \frac{\pi}{k^2} \sum_{l=0}^{\infty} (2l+1)\sin^2(\phi_{s-t}). \tag{2.21}$$

The experimental entrance channel of our system consists of neutral Rb and ionized Sr^+ both in ground electronic states ($\mathrm{Sr}^+(5s)+\mathrm{Rb}(5s)$). This channel at close inter-molecular separation below ~1 nm splits into two channels. These channels correspond to the singlet configuration for the $(2)^1\Sigma^+$ channel and a triplet configuration for the $(1)^3\Sigma^+$ channel. If the atom and the ion are initialized in the triplet state (atoms are prepared in $|\mathrm{F}=2, \mathrm{m_F}=-2\rangle$ state, and the ion is prepared in the $|{\downarrow}\rangle$ state), then spin-exchange is forbidden. But, if the atom and ion are prepared in a singlet/triplet superposition, spin-exchange might occur as the phase accumulated by these two different states during a collision is different and after the collisions, atom and ion might project to a different state.

We can use the random-phase approximation as in Equation 2.8 to obtain the spin-exchange cross-section:

$$\sigma^{l<L}_{\text{spin exch.}} = \frac{\pi}{k^2}\sum_{l=0}^{l<L}(2l+1)\sin^2\phi_l = \frac{\pi L^2}{2k^2} = \pi\sqrt{\frac{\mathrm{C}_4}{2E}}. \tag{2.22}$$

We see that when using the random-phase approximation, the spin-exchange cross section scales like Langevin and is a factor of 2 smaller. This means that for every Langevin collision where atoms and ion are prepared in an opposite spin state the probability for spin-exchange is 50%.

2.2.3 Spin-exchange with hyperfine states

In ^{87}Rb atoms, the nucleus also has a spin of 3/2. The total angular momentum is now $F = I + L + S$. Where S is the electronic spin angular momentum, L is the electronic orbital angular momentum, and I is the intrinsic angular momentum of the nucleus. We are interested in the L=0 case where the total angular momentum can be:

$$\left|\frac{3}{2}-\frac{1}{2}\right| \le F \le \left|\frac{3}{2}+\frac{1}{2}\right|. \tag{2.23}$$

The projection of F can take values $|m| \le F$. Before a collision, when the atom-ion separation is above $> 10\,\text{Å}$ the hyperfine spin-spin interaction between nucleus and valence unpaired electron is dominant over the internuclear spin-spin interaction and state of the atom can be described in a hyperfine basis $|F, m_F\rangle$ Figure 2.3. During a collision the splitting between $^3\Sigma_0^+$ and $^1\Sigma_0^+$ states is much larger ($\sim$ 200 THz) than the hyperfine splitting (6.8 GHz). It is, therefore, appropriate to project the ^{87}Rb hyperfine states on a $|{\uparrow}\rangle$ $|{\downarrow}\rangle$ basis:

$$|F, m_F\rangle = \sum_{m_I+m_S=m_F} c^{F,I,S}_{m_I,m_S,m_F}\,|I, m_I\rangle\,|S, m_S\rangle\,, \tag{2.24}$$

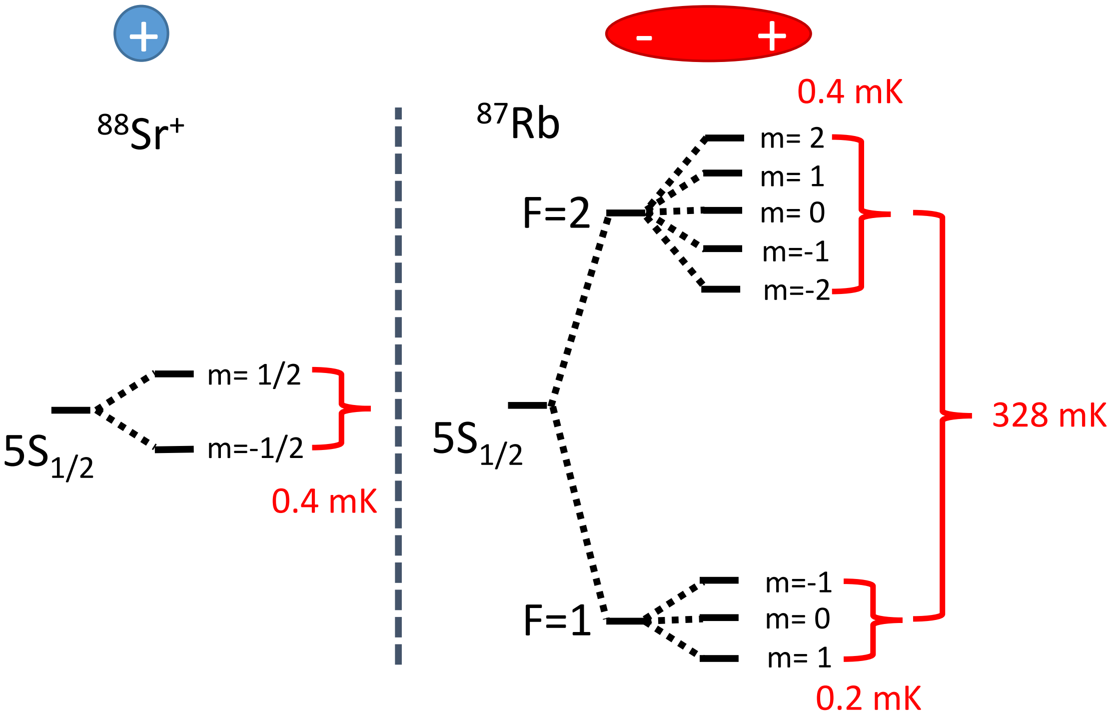

Figure 2.3: Energy levels diagrams of the ^{88}Sr$^+$ Zeeman splitting and hyperfine splitting of the ^{87}Rb. The Zeeman splitting is for B≈3 G.

where:

$$c^{F,I,S}_{m_I,m_S,m_F} = \langle I,S,m_I,m_S|F,m_F\rangle = (-1)^{S-1+m_F}\sqrt{2F+2}\begin{pmatrix} S & I & F \\ m_S & m_I & -m_F \end{pmatrix} \tag{2.25}$$

In this chapter, we discuss the spin-exchange under degenerate internal states (DIS) approximation. This approximation calculates the cross-section under the assumption that the entrance and exit channel have the same energy. We ignore the effect of magnetic field on Zeeman splitting and the hyperfine interaction. Both these interactions are orders of magnitude smaller than the singlet-triplet splitting. Even though this is an uncontrolled approximation, it allows for the quantitative description of the spin-exchange process.

Even though we do not include the hyperfine interaction term in $\hat{\mathcal{H}}^{exch}$ Equation 2.13, we do take it into account when calculating the cross-section. First, we project the state of Rb atom from $|\downarrow\rangle$ $|\uparrow\rangle$ basis to hyperfine basis $|F,m_F\rangle$. Second, because our collision energy is in the order of few mK when the atoms are prepared in the $F=1$ manifold a spin-exchange collision cannot transfer the atoms to the $F=2$ manifold due to the 328 mK hyperfine energy gap. When atoms are prepared in a $|1,-1\rangle$ state and ion is in the $|\downarrow\rangle_{\mathrm{Sr}^+}$ state the only spin-exchange channel possible is:

$$|1,-1\rangle_{\mathrm{Rb}}\,|{\downarrow}\rangle_{\mathrm{Sr}^+} \not\rightarrow |2,-2\rangle_{\mathrm{Rb}}\,|{\uparrow}\rangle_{\mathrm{Sr}^+}\,, \tag{2.26}$$

But this is energetically forbidden due to hyperfine barrier. When we collide atoms prepared in a $|1,-1\rangle$ state with $|{\downarrow}\rangle_{\mathrm{Sr}^+}$ ion, these spin-exchange channels are open:

$$\begin{aligned} |1,-1\rangle_{\mathrm{Rb}}\,|{\uparrow}\rangle_{\mathrm{Sr}^+} &\rightarrow |1,0\rangle_{\mathrm{Rb}}\,|{\downarrow}\rangle_{\mathrm{Sr}^+} \\ |1,-1\rangle_{\mathrm{Rb}}\,|{\uparrow}\rangle_{\mathrm{Sr}^+} &\not\rightarrow |2,0\rangle_{\mathrm{Rb}}\,|{\downarrow}\rangle_{\mathrm{Sr}^+} \end{aligned} \tag{2.27}$$

To calculate the cross-section for spin-exchange, we need to calculate the matrix element of Equation 2.18: $|\langle\langle 1,-1|_{\mathrm{Rb}}\cdot\langle{\uparrow}|_{\mathrm{Sr}^+}\,|\hat{\mathbf{S}}_{(1)}\cdot\hat{\mathbf{S}}_{(2)}|\,|1,m_F\rangle_{\mathrm{Rb}}\cdot|{\downarrow}\rangle_{\mathrm{Sr}^+}\rangle|^2$.

We first expand the atom's hyperfine state in the electron spin basis,

$$|1,-1\rangle_{\mathrm{Rb}}\,|{\uparrow}\rangle_{\mathrm{Sr}^+} = \frac{\sqrt{3}}{2}\,|{\uparrow}\rangle_{\mathrm{elec.}}\,|\tfrac{3}{2},-\tfrac{3}{2}\rangle_{\mathrm{nucl}}\,|{\uparrow}\rangle_{\mathrm{Sr}^+} - \frac{1}{2}\,|{\downarrow}\rangle_{\mathrm{elec.}}\,|\tfrac{3}{2},-\tfrac{1}{2}\rangle_{\mathrm{nucl}}\,|{\uparrow}\rangle_{\mathrm{Sr}^+} \tag{2.28}$$

During a collision when spin-exchange happens, the valence electrons wavefunctions overlap and we project on a singlet/triplet basis,

$$|1,-1\rangle_{\mathrm{Rb}}\,|{\uparrow}\rangle_{\mathrm{Sr}^+} = \frac{\sqrt{3}}{2}\,|1,1\rangle\,|\tfrac{3}{2},-\tfrac{3}{2}\rangle_{\mathrm{nucl}} - \frac{1}{2\sqrt{2}}\,(|1,0\rangle-|0,0\rangle)\,|\tfrac{3}{2},-\tfrac{1}{2}\rangle_{\mathrm{nucl}} \tag{2.29}$$

The final state of spin-exchange collision channel can be expanded as,

$$|1,0\rangle_{\mathrm{Rb}}\,|{\downarrow}\rangle_{\mathrm{Sr}^+} = \frac{1}{\sqrt{2}}\,|{\uparrow}\rangle_{\mathrm{elec.}}\,|\tfrac{3}{2},-\tfrac{1}{2}\rangle_{\mathrm{nucl}}\,|{\downarrow}\rangle_{\mathrm{Sr}^+} - \frac{1}{2}\,|{\downarrow}\rangle_{\mathrm{elec.}}\,|\tfrac{3}{2},\tfrac{1}{2}\rangle_{\mathrm{nucl}}\,|{\downarrow}\rangle_{\mathrm{Sr}^+} \tag{2.30}$$

Similarly as we did for $|1,-1\rangle_{\mathrm{Rb}}\,|{\uparrow}\rangle_{\mathrm{Sr}^+}$ state we project it on a singlet/triplet basis:

$$|1,0\rangle_{\mathrm{Rb}}\,|{\downarrow}\rangle_{\mathrm{Sr}^+} = \frac{1}{2\sqrt{2}}\,(|1,0\rangle+|0,0\rangle)\,|\tfrac{3}{2},-\tfrac{1}{2}\rangle_{\mathrm{nucl}} - \frac{1}{\sqrt{2}}\,|1,-1\rangle\,|\tfrac{3}{2},\tfrac{1}{2}\rangle_{\mathrm{nucl}} \tag{2.31}$$

We now apply a spin-spin operator on the initial state

$$\hat{\mathbf{S}}_{(1)}\cdot\hat{\mathbf{S}}_{(2)}\,|1,-1\rangle_{\mathrm{Rb}}\,|{\uparrow}\rangle_{\mathrm{Sr}^+} = \frac{\sqrt{3}}{8}\,|1,1\rangle\,|\tfrac{3}{2},-\tfrac{3}{2}\rangle_{\mathrm{nucl}} - \frac{1}{2\sqrt{2}}\left(\frac{1}{4}\,|1,0\rangle+\frac{3}{4}\,|0,0\rangle\right)|\tfrac{3}{2},-\tfrac{1}{2}\rangle_{\mathrm{nucl}} \tag{2.32}$$

The nuclear spin is written in red font, to emphasize that spin-spin $\hat{\mathbf{S}}_{(1)}\cdot\hat{\mathbf{S}}_{(2)}$ operator does not affect it. The matrix element squared then equals:

$$\left|\langle 1,0|_{\mathrm{Rb}}\,\langle{\downarrow}|_{\mathrm{Sr}^+}\,\hat{\mathbf{S}}_{(1)}\cdot\hat{\mathbf{S}}_{(2)}\,|1,-1\rangle_{\mathrm{Rb}}\,|{\uparrow}\rangle_{\mathrm{Sr}^+}\right|^2 = \frac{1}{32}. \tag{2.33}$$

Plugging this into equation Equation 2.18 we get the spin-exchange cross-section for $|1,-1\rangle_{\text{Rb}}\,|{\uparrow}\rangle_{\text{Sr}^+} \rightarrow |1,0\rangle_{\text{Rb}}\,|{\downarrow}\rangle_{\text{Sr}^+}$ channel:

$$\sigma_{exch} = \frac{\pi}{8k^2}\sum_{l=0}^{\infty}(2l+1)\sin^2(\phi_{s-t}). \tag{2.34}$$

We see that spin-exchange cross-section in hyperfine basis for non-stretched state is 8 times smaller that would be for a stretched state. This is caused by the fact that non-stretched state has projection to $|{\uparrow}\rangle_{\text{elec.}}\,|{\uparrow}\rangle_{\text{Sr}^+}$ spin configuration and also due to the fact that $|1,-1\rangle_{\text{Rb}}\,|{\uparrow}\rangle_{\text{Sr}^+} \rightarrow |2,0\rangle_{\text{Rb}}\,|{\downarrow}\rangle_{\text{Sr}^+}$ channel is energetically forbidden. Assuming random-phase approximation we expect that spin-exchange rate will be 16 times smaller than Langevin rate Equation 2.4.

2.2.4 Spin-relaxation

If the atom-ion system is initialized in a stretched state, because of conservation of angular momentum the spin state should be preserved during a collision. Because of second-order spin-orbit (SO) coupling and dipole-dipole interaction Equation 2.35, the singlet and triplet states ($^1\Sigma^+$ and $^3\Sigma^+$) are not eigenstates anymore, the total spin-projection is no longer conserved which leads to spin-relaxation. These causes transfer of orbital angular momentum into the spin. The second-order SO coupling and dipole-dipole interaction responsible for spin-relaxation terms have the form:

$$\hat{V}_{\text{dd}}(R) + \hat{V}_{\text{SO}}(R) = \sqrt{\frac{24\pi}{5}}\left[-\frac{\alpha^2}{R^3} + \lambda_{\text{SO}}(R)\right]\sum_q(-1)^q Y^*_{2,-q}(\hat{R})[\hat{\mathbf{S}}_{Rb}\otimes\hat{\mathbf{S}}_{Sr^+}]^{(2)}_q. \tag{2.35}$$

where α is the fine-structure constant and $[\hat{\mathbf{S}}_{Rb}\otimes\hat{\boldsymbol{S}}_{Sr^+}]^{(2)}_q$ is a spherical tensor product of $\hat{\mathbf{S}}_{Rb}$ and $\hat{\mathbf{S}}_{Sr^+}$. The second-order SO coupling term proportional to $\lambda_{\text{SO}}(R)$ is due to the SO interaction between the $^3\Sigma$ electronic state and the electronic states of $^3\Pi$ symmetry [47]. The second-order SO interaction Figure 2.4 couples molecular states with different total spin S at short range, leading to spin-relaxation in heavy ion-atom collisions [68].

2.2.5 Charge-exchange

A charge-exchange reaction between alkali and earth-alkali atoms is a model chemical reaction where open shell reactants exchange an electron and form closed shell products. Charge-exchange in cold atom-ion systems was studied in several experiments [58, 28, 26, 56, 60, 32], but only a few were performed without the presence of resonant laser light with an allowed optical transition of the neutral

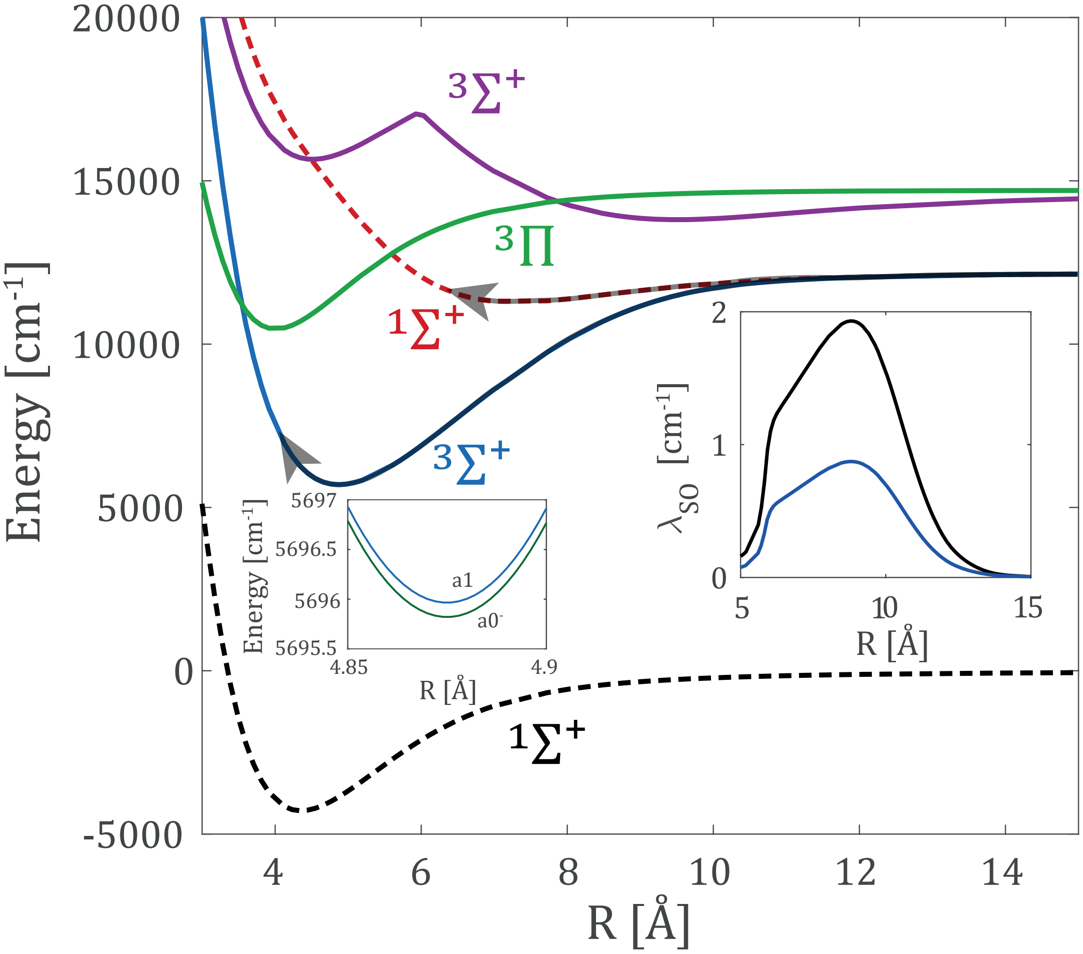

Figure 2.4: Relevant potential energy curves (PECs) of the $(\mathrm{RbSr})^+$ complex [4]. Left inset shows the splitting of the $^3\Sigma^+$ state into a0$^-$ and a1 components. Right inset shows the second-order spin-orbit coupling coefficient ($\lambda_{\mathrm{SO}}(R)$). Black line represents that obtained by calculation and blue line is the λ_{SO} scaled to match our measured SR rate.

atoms and therefore without populating higher molecular states [56, 60, 32]. In our case, charge exchange is not a resonant process, and the ionization energy difference between Sr^+ and Rb has to be released or absorbed. Charge exchange can proceed in several different ways. As a radiative charge-exchange where the excess energy is released with a photon or as a non-adiabatic crossing between molecular potentials where energy transfers into motional degrees of freedom. Alternatively, at high densities ($>10^{-18}\,\mathrm{m}^{-3}$), the nonradiative charge exchange can proceed through a three-body recombination process where the atom an ion re-combine on the charge exchanged molecular potential, and the excess energy is carried away by a third atom [31].

In our experiment, due to an absence of singlet-singlet curve crossings in the entrance channel and mild densities ($\sim 10^{-17}\,\mathrm{m}^{-3}$), we expect charge exchange to be radiative. Sr has higher ionization energy than Rb. Therefore the entrance channel $\mathrm{Sr}^{+}(5\mathrm{s})+\mathrm{Rb}(5\mathrm{s})$ does not represent the absolute ground state but corresponds to an excited molecular state of $(\mathrm{RbSr})^{+}$ (Figure 2.2). Charge exchange involves both valence electrons moving into the $5\mathrm{s}^2$ state of the Strontium atom. In the absence of spin-orbit coupling, radiation cannot couple the singlet and triplet state. As a result, chemical reactions are triggered or suppressed by preparing the collision in a specific singlet/triplet state projection. Because the atomic bath governs the spin of the ion, the control of the spin state of ultracold atoms determines the reaction rate. Unlike previous experiments where the charge-exchange rate was modified by initializing atoms in different excited states. In our experiment, both atoms and ion are initialized in their ground electronic states.

2.3 Ion Paul trapping

Ions can be trapped in Penning, Paul, multipole and optical dipole traps [34, 53, 72, 18]. In our experiment we use a Paul trap. Because of Laplace equation, $\nabla^2\Phi\left(\mathbf{r}\right)=0$ static electric fields are not sufficient to confine a charged particle in all three dimensions. We use a combination of radiofrequency (rf) oscillating and static (dc) electric field. Paul traps form a ponderomotive potential that confines the ion. In linear segmented Paul traps ponderomotive potential confines, the ion in two axes (radial axis) and additional DC electric field is used to harmonically confine the ion in the axial dimension. The resulting potential is:

$$\mathrm{V}\left(x,y,z,t\right)=\frac{\mathrm{V_{rf}}}{2}\left(1+\frac{x^2-y^2}{r_0^2}\right)\cos(\Omega t)+\frac{\mathrm{V_{dc}}}{z_0^2}\left[z^2-\frac{1}{2}\left(x^2+y^2\right)\right]+\frac{\mathrm{V_{bias}}}{2}\left(1+\frac{x^2-y^2}{r_0^2}\right). \tag{2.36}$$

Here, Ω is the angular frequency of the oscillating electric field,V_{rf}, V_{dc} and V_{bias} are the voltages of oscillating, static and bias electric field, r_0 is the effective center of the trap to electrode distance and z_0 is the effective center of the trap to electrode distance. Bias electric field is applied in order to remove the degeneracy of the two radial modes.

If the rf field frequency Ω is much higher than the resulting trapping frequencies Equation 2.41 the effective motion of the ion the trap is is well described by Mathieu equation,

$$\ddot{u}_i+u_i\left[a_i+2q_i\cos(\Omega t)\right]\frac{\Omega^2}{4}=0. \tag{2.37}$$

where u_i is the displacement of the ion from trap center along each axis $i=x,y,z$

and parameters a_i and q_i, are:

$$\begin{aligned} a_{x/y} &= -\frac{4e}{m\Omega^2}\left(\frac{\mathrm{V}_{\mathrm{dc}}}{z_0^2} \pm \frac{\mathrm{V}_{\mathrm{bias}}}{r_0^2}\right) \\ a_z &= \frac{8e}{m\Omega^2}\frac{\mathrm{V}_{\mathrm{dc}}}{z_0^2} \end{aligned} \tag{2.38}$$

$$\begin{aligned} q_x = -q_y &= \frac{2eV_{rf}}{mr_0^2\Omega^2} \\ q_z &= 0. \end{aligned} \tag{2.39}$$

e is the charge of the ion.

If $q_i^2 << 1$, the solution for Eq. (2.37) in the first order of q is [76]:

$$u_i \approx \left[u_i^{\mathrm{dc}} + A_i\cos(\omega_i t + \phi_i)\right]\left[1 + \frac{q_i}{2}\cos(\Omega t)\right], \tag{2.40}$$

The ion follows a Mathieu trajectory which is a superposition of secular motion $A_i\cos(\omega_i t + \phi_i)$, inherent micromotion $A_i\cos(\omega_i t + \phi_i)\left(\frac{q_i}{2}\cos(\Omega t)\right)$ and excess micromotion $u_i^{\mathrm{dc}}\left(\frac{q_i}{2}\cos(\Omega t)\right)$ [5, 76].

ϕ_i is the phase, A_i are secular amplitudes of the motion and ω_i are secular frequencies defined as [76]:

$$\omega_i \approx \frac{1}{2}\Omega\sqrt{a_i + \frac{1}{2}q_i^2}, \tag{2.41}$$

In segmented linear Paul traps, the axial confinement ($i = z$) is harmonic $q_z = 0$. The energy oscillates between kinetic and potential energy like in a classical harmonic oscillator. On the other hand in radial axes ($i = x/y$) the energy oscillates between secular kinetic energy and micromotion kinetic energy. The inherent micromotion is caused by the finite secular energy of an ion. Due to the secular kinetic energy the ion has a trajectory outside the center of the trap and couples rf oscillating electric fields. Inherent micromotion can be minimized by cooling the ion to ground state. Excess-micromotion (EMM), is caused by mechanical imperfections of the trap. These cause the displacement u_i^{dc} in Equation 2.40.

The micromotion affects the dynamics during atom-ion collisions. For every collision, the collisions disturbs the Mathiew trajectory and Paul trap can pump or withdraw energy from the ion depending on the rf phase during the collision and the position of the ion at the moment of the collision.

2.4 Collisional dynamics in a Paul trap

From thermodynamics, we know that two isolated systems that are brought into contact will thermalize to equal temperature. Sympathetic cooling is the process in which the temperature of a system is reduced by bringing it into contact with a larger and colder reservoir. There are many prospects for using sympathetic cooling to cool dark ions, anions, molecular ions for which the laser cooling is not possible.

In our experiment, the ions are trapped using rf electric fields. These oscillating fields can pump or withdraw energy into and out of the ion. We studied the effect of these fields on a sympathetic cooling. As a refrigerator, we use laser-cooled Rb atoms.

In our system we observe a non-equilibrium dynamics due to following mechanism. Since the atoms are trapped in a shallow potential (3 µK) after every atom-ion collision when they exchange energy and momentum, the atom leaves the trap and the temperature of the Rb atomic cloud remains unchanged. This is because the ion's temperature is above 100s of μK.

2.4.1 Effect of excess micromotion on sympathetic cooling

In 1968 Major and Demhelt studied sympathetic cooling of RF trapped ions in the presence of cooled buffer gas of atoms [42]. They showed that in Paul traps, sympathetic cooling is stable only for system with lighter atoms than ions ($\mathrm{m}_i > \mathrm{m}_a$). Equal mass was shown to result in neither cooling nor heating. For light ions colliding with heavy atoms ($\mathrm{m}_i < \mathrm{m}_a$), exponential heating of the ion due to consecutive collisions was predicted. This heating finally leads to ion loss from the trap.

2.4.2 Hard-sphere collisions simulation

We perform two type of atom-ion collision simulations. The simpler type treats only hard-sphere collisions. In a more involved simulation (Sec. subsection 2.4.4) we also include the effect of the polarization potential on the ion's motion.

The dynamics of atom-ion collisions can me modeled as hard-spheres where polarization potential and Pauli exclusion principle are modeled with a δ potential. This model is enough to capture the collision dynamics [45, 80].

Together with Ziv Meir and Nitzan Akerman, we performed a Monte Carlo simulation. The simulation begins with sampling the ion's initial total energy ($\mathrm{E}_{\mathrm{ion}}$) according to a Maxwell-Boltzmann distribution. We set the ion's amplitudes by the equipartition theorem: $A_i = \sqrt{\frac{2\mathrm{E}_{\mathrm{ion}}}{3m\omega_i^2}}$. The initial phases, ϕ_i, are chosen from

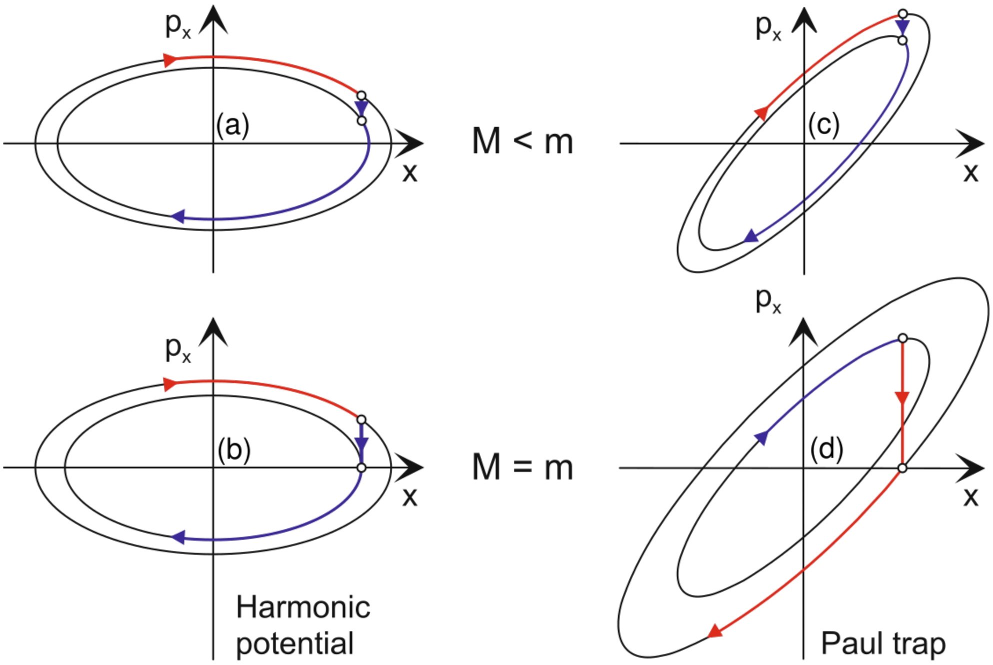

Figure 2.5: The ion trajectory in phase space. m is the mass of an ion, and M is the mass of atoms. We assume that a collision brings ion to rest instantaneously. We see that while in the case of harmonic potential such collisions always decrease the energy. In ponderomotive potential of Paul trap even stopping collision (M=m) can lead to increase in ion energy. The reason for this is that the phase space trajectory of an ion in a Paul trap is not static but changes with a frequency of the RF field. We also see that increasing the mass of atoms, decreases this heating effect. This figure was adapted from [62].

a uniform random distribution. The motion of the ion in between the collisions follows a Mathieu trajectory (Equation 2.40) and the ion's velocity before the collision is:

$$v_i\left(t_c\right) \approx -A_i \omega_i \sin\left(\omega_i t_c + \phi_i\right) - \left(A_i \cos\left(\omega_i t_c + \phi_i\right) + u_i^{dc}\right) \Omega \frac{q_i}{2} \sin\left(\Omega t_c\right). \tag{2.42}$$

Here, the first term is the secular velocity and the second term is the micromotion. t_c represents the time between consecutive collisions. The atomic velocity is sampled assuming a thermal distribution (3 µK). The collisions are modeled as instantaneous, therefore the position of the ion remains fixed before and after the collision, $\mathbf{u}^{'} = \mathbf{u}$:

$$A_i \cos(\omega t_c + \phi) = A_i^{'} \cos(\omega t_c + \phi^{'}). \tag{2.43}$$

Where, $A_i^{'}$'s and $\phi_i^{'}$'s are the ion's amplitudes, and phases after the collision and the velocity is determined by energy-momentum conservation:

$$\mathbf{v}^{'} = (1-\beta)(\mathbf{v}-\mathbf{v}_a) + \beta\Re(\mathbf{v}-\mathbf{v}_a) + \mathbf{v}_a. \tag{2.44}$$

Here, $\mathbf{v}^{'}$ and $\mathbf{v}$ are the ion's velocity after and before the collision, $\mathbf{v}_a$ is the atom's velocity before the collision, $\beta = \frac{m_a}{m_a+m_i}$ and $\Re$ is a rotation matrix which defines scattering angles [80].

To get the secular velocity we subtract the micromotion velocity:

$$v^{'}_{i_{|sec}}(t_c) = v_i^{'}(t_c) + \left(A_i\cos(\omega_i t_c + \phi_i) + u_i^{dc}\right)\Omega\frac{q_i}{2}\sin(\Omega t_c), \tag{2.45}$$

which is used to extract the secular position,

$$u^{'}_{i_{|sec}}(t_c) = u_i^{dc} + A_i^{'}\cos\left(\omega_i t_c + \phi_i^{'}\right) = u_i^{dc} + A_i\cos(\omega_i t_c + \phi_i). \tag{2.46}$$

From the above equation we extract new amplitudes and phases:

$$u^{'}_{i_{|sec}}(t_c) - u_i^{dc} = A_i^{'}\cos\left(\omega_i t_c + \phi_i^{'}\right) \tag{2.47}$$

$$v^{'}_{i_{|sec}}(t_c) = -A_i^{'}\omega_i\sin\left(\omega_i t_c + \phi_i^{'}\right). \tag{2.48}$$

Using these equations we analytically calculate the change of secular amplitude and therefore the ion's velocity during a collision. With new parameters, we continue to the subsequent collision. After reaching the steady state E_{mode}, we repeat the simulation ~10,000 times and extract the ion's energy distribution.

2.4.3 Hard-sphere collisions with hyperfine energy release

During collisions, if Rb atoms are initialized in the F=2 state of the hyperfine manifold, they can relax to F=1 state. This relaxation involves a release of 328 mK of energy. This leads to the heating of the ion. Since this is a stochastic process to extract the energy distribution of the ion after multiple collisions with F=2 Rb atoms we used a numerical simulation.

In the simulation we assume that $\frac{\mu}{m_{Rb}}328\,\text{mK} = 165\,\text{mK}$ is carried away by the colliding atom and remaining $\frac{\mu}{m_{Sr^+}}328\,\text{mK} = 163\,\text{mK}$ energy is coupled to the motion of the ion following a collision. To include this effect in the simulation, we assume that energy is released instantaneously right after the collision when $(\text{RbSr})^+$ molecular state is projected on Rb and Sr^+ atomic states. In the simulation, we add this process after Equation 2.44. We first transfer into the center of mass frame of reference:

$$\begin{aligned}\mathbf{v}_a^{''} &= \mathbf{v}_a^{'} - \mathbf{v}_{\text{com}} \\ \mathbf{v}^{''} &= \mathbf{v}^{'} - \mathbf{v}_{\text{com}},\end{aligned} \tag{2.49}$$

where:

$$\mathbf{v}_{\text{com}} = \frac{\mathbf{v}_a^{'} m_{\text{Rb}} + \mathbf{v}^{'} m_{\text{Sr}^+}}{m_{\text{Rb}} + m_{\text{Sr}^+}}. \tag{2.50}$$

It this frame the total momentum of the system before and after the release of the hyperfine energy is zero:

$$\mathbf{v}_a^{''} m_{\text{Rb}} + \mathbf{v}^{''} m_{\text{Sr}^+} = \mathbf{v}_a^{'''} m_{\text{Rb}} + \mathbf{v}^{'''} m_{\text{Sr}^+} = 0. \tag{2.51}$$

Due to energy-momentum conservation the hyperfine energy release $\mathbf{v}^{'''} = \mathbf{v}^{''} + \mathbf{v}_{\text{HF}}$ increases the velocity in the direction of $\hat{\mathbf{v}}^{''}$ such that the kinetic energy of ion increases by:

$$\Delta E_{HF} = \frac{m_{\text{Sr}^+}}{2} \left(v_{\text{HF}}^2 - v_{\text{HF}} \cdot v^{''} \right) \tag{2.52}$$

Since $\mathbf{v}_{\text{HF}}$ and $\mathbf{v}^{''}$ are collinear we drop the vectors and work with scalar quantities $|\mathbf{v}| = v$. Since the collision always increases the energy by increasing the speed we solve Equation 2.52 and we drop the solution that decreases the velocity:

$$v_{\text{HF}} = \frac{v^{''} + \sqrt{v^{''2} - \frac{8E_{\text{HF}}}{m_{\text{Sr}^+}}}}{2}. \tag{2.53}$$

We now transform:

$$\mathbf{v}^{'''} = \mathbf{v}^{''} + v_{\text{HF}} \cdot \hat{\mathbf{v}}^{''}, \tag{2.54}$$

into the lab reference frame:

$$\mathbf{v}^{'} = \mathbf{v}^{'''} + \mathbf{v}_{\text{com}} \tag{2.55}$$

And continue the simulation by plugging the $\mathbf{v}^{'}$ into Equation 2.45. The simulation is performed such that hyperfine energy release occurs with a certain probability. We study the effect of this probability on the resulting energy distribution.

On Figure 2.6 we see the effect of hyperfine energy release on energy distribution. We performed the simulation with excess micromotion energy $E_{EMM} = 3\,\text{mK}$ and 7.92% probability to release hyperfine energy. $E_{EMM} = 3\,\text{mK}$ was used to mimic the effect of collisions induced micromotion subsection 2.4.4, we see that results in a Tsallis energy distribution $T = 3.2\,\text{mK}$, $n = 4$ and $E_{mode} = 2 \cdot \frac{nT}{n-2} = 12.8\,\text{mK}$.

$$\text{P}\left(\text{E}\right) = \frac{(n-3)(n-2)(n-1)}{2(n\text{T})^3} \frac{\text{E}^2}{\left(1 + \frac{\text{E}}{n\text{T}}\right)^n}. \tag{2.56}$$

The atomic radial Gaussian width is $\sigma_{\text{atom}}^{\text{rad}} = 5\,\mu\text{m}$ and axial is $\sigma_{\text{atom}}^{\text{axias}} = 30\,\mu\text{m}$. The ion trap parameters are: $[\omega_x, \omega_y, \omega_z]$=$2\pi\times$[0.61, 0.6, 0.1] kHz.

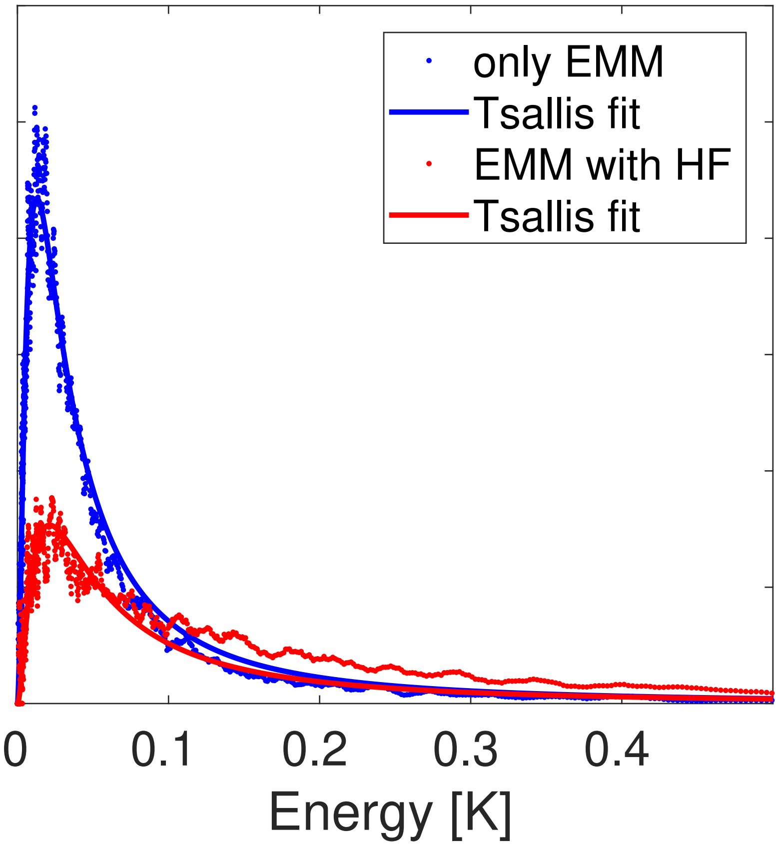

Figure 2.6: Molecular dynamics simulation of the ions energy distribution for different hyperfine energy release probabilities. Blue $p_{HF} = 0\%$, red $p_{HF} = 7.92\%$.

2.4.4 Simulation with the long-range potential

The simulations performed in the previous section with contact interaction, capture the heating of the ion induced by EMM or hyperfine energy relase. The long-range polarization potential $V(r) = -C_4/2r^4$ in combination with rf electric fields of the Paul trap further affects the dynamics of atom-ion collisions. This effect is particularly important if the hyperfine energy relase and EMM are absent.

Cetina et al. [8] showed that even a zero temperature ion without EMM colliding with zero temperature atoms leads to heating. The atom during a collision temporarily pulls the ion from the center of the trap. This induces a micromotion, and such collision can lead to heating.

To study this effect, we performed a more involved simulation in which we treat the ion and atoms colliding due to a $-1/r^5$ attractive force. Apart from the polarization potential force, the ion is also affected by the Paul trap electric fields while atoms are modeled as free particles. The EMM was assumed to be fully compensated. To obtain the energy distribution, we simulate the process with multiple consecutive collisions several times. The ion initial energies are sampled from a Maxwell-Boltzmann distribution with a temperature of 0.05 mK, and the phases are sampled uniformly.

Similarly to hard-sphere simulation, we define the atoms cloud size and trap parameters. To include the repulsive exchange interaction we add a 5 nm repulsive delta potential. The simulation is repeated with every atom randomly generated while the ion motion is preserved between consecutive collisions.

In Figure 2.7 we show an example of the energy distribution resulting from our simulation with polarization potential. Unlike the simple hard-sphere simulation, our analytic theory (Tsallis distribution) is not fully adequate. There is a deviation from power-law tail above $\sim 300\,\mathrm{mK}$ due to the numerical simulation error.

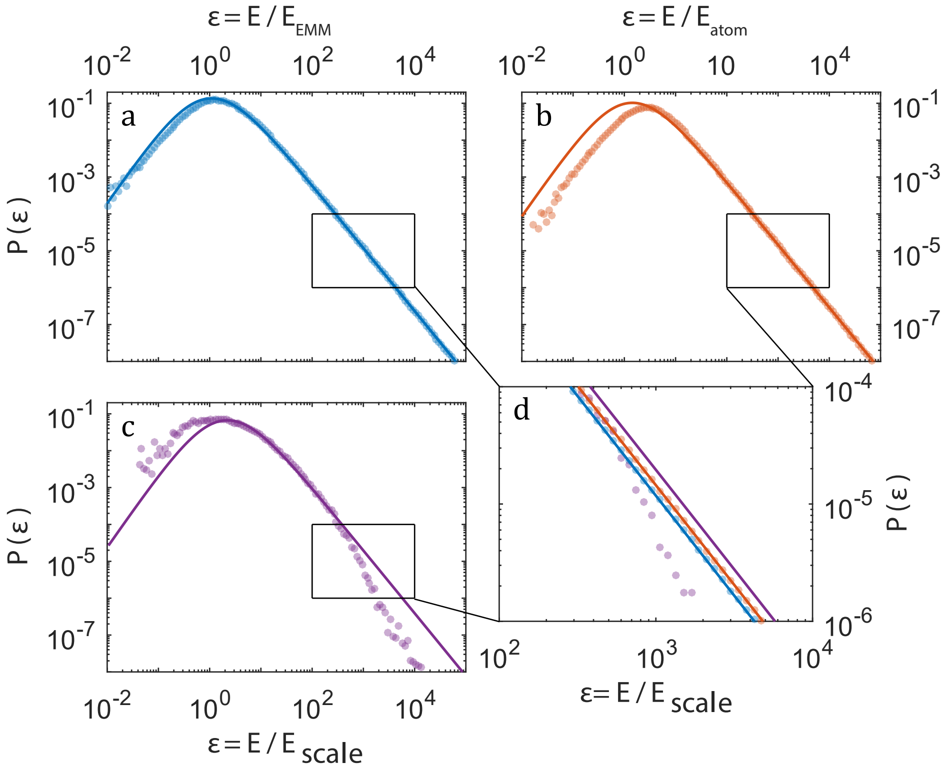

Figure 2.7: Molecular dynamics simulation of the ion's energy distribution for different heating mechanisms. Energy distribution where the heating is dominated by EMM (a) and the temperature of the atoms (b). The curve represents a fit to a Tsallis distribution (Equation 2.56). c) Simulation without EMM where $^1/_{r^4}$ polarization potential is included and heating is dominated by the collision-induced micromotion during a collision. d) An enlarged view of the power-law tail. The figure was adapted from [46].

Chapter 3

Experimental setup

3.1 Cold atom experimental system

Our hybrid experimental setup consists of two vacuum chambers (ion's chamber and atom's chamber) Figure 3.1. The chambers are connected by a thin tube such that vacuum conductivity is so low that differential pressure between them has 1:10 ratio[1]. We load $\sim 10^6$ Rb atoms into a magneto-optical trap (MOT) from Alvatec oven. Then we decrease the cooling laser intensity and further red-detune it to increase the density and lower the temperature (dark MOT).

Atoms are then transferred into a single focused beam CO2 dipole trap ($\lambda = 10.6\,\mu\mathrm{m}$) which is focused to the center of MOT. In the CO2 dipole trap atoms are evaporatively cooled by decreasing the beam power to several μK (Figure 3.2). We then ramp down the CO2 beam such that atoms are adiabatically loaded into YAG laser 1D lattice ($\lambda = 1064\,\mathrm{nm}$) which is composed of two counter-propagating beams. We then transport the atoms to the ion's chamber by changing the relative frequency between the two lattice beams.

Because in the YAG lattice atoms density is modulated with a period of half the optical wavelength we load the atoms into crossed YAG dipole trap 50 µm above the position of the ion. Here, $\sim 10^5$ atoms are spin-polarized using a combination of resonant microwave pulses and 780 nm laser light subsection 3.1.1. Using a piezo-driven mirror, the YAG crossed dipole trap is moved to the position of the ion and interactions begin. During atom-ion interaction all lasers beams are mechanically blocked except for the off-resonant dipole trap lasers at 1064 nm. After the desired interaction time, we release the atoms from the trap. After time-of-flight, we detect the number of atoms and their temperature using absorption imaging. The measured density and temperature are used for the atom density estimation.

---

[1] 10^{-11} Torr for atom's chamber and 10^{-12} Torr for ion's chamber

3.1.1 Preparation of spin-polarized atomic clouds

After loading Rb atoms into are loaded into the the YAG crossed dipole trap we need to prepare them in a specific spin state of hyperfine manifold (see Figure 2.3). Because optical trapping is spin-independent, we can prepare ^{87} Rb atoms in any state from the hyperfine manifold. The YAG dipole trap is initially positioned 60 µm above the ion. This allows us to manipulate the state of the atoms a few ms before the interactions with the ion begin. We are mainly interested in states $|1,1\rangle$ and $|2,2\rangle$ because if the ion spin is aligned they are protected against spin-exchange because of angular momentum conservation ($|2,2\rangle$) and hyperfine energy barrier ($|1,1\rangle$). For state preparation we use the following protocol:

1. Atoms are prepared in a F=1 manifold using a depump laser beam tuned to $5S_{1/2}$(F=2) $\leftrightarrow$ $5P_{3/2}$(F=2) transition.
2. A MW π-pulse on transitions connecting $|1,0\rangle \leftrightarrow |2,0\rangle$ and $|1,-1\rangle \leftrightarrow |2,-1\rangle$ is applied to depopulate $|1,0\rangle$ and $|1,-1\rangle$.
3. Repeat step 1.

The pumping procedure is repeated 20 times Figure 3.3. To prepare the atoms in a $|2,2\rangle$ Rb state a single additional adiabatic pulse is applied after pumping. The pulse connects the $|1,1\rangle \leftrightarrow |2,2\rangle$ states, has a duration of 1ms, and starts 200kHz red detuned and finishes 200kHz blue detuned. The fidelity of a Zeeman state preparation is above >99%.

3.1.2 Density of ultracold atomic cloud

One of the properties of $-{}^{1}/{}_{r^4}$ polarization potential is that the Langevin collision rate is temperature independent (see Equation 2.5). This means that all we need to measure to get the average number of collisions is the interaction time and density of atoms. Measuring the density of the atomic cloud is a hard task because many systematic effects can bias this measurement. To this end we need to measure the number of atoms, dipole trap frequencies, and temperature.

The number of atoms, N, is determined using the resonance time-of-flight absorption imaging. The shadow that the atoms create is logarithmically proportional to a number of atoms. The trap frequencies are measured by resonant excitation spectroscopy. The potential trap depth is modulated at various frequencies. When we hit twice the trap frequency, the atoms are heated, and we observe the loss of atoms from the trap. We measured the trap frequencies to be $[\omega_x, \omega_y, \omega_z]$=$2\pi\times$[0.61, 0.6, 0.1] kHz.

The temperature is determined using a time-of-flight (TOF) method. We measure the expansion of a cloud after [0.4, 0.6, 0.8, and 1] ms. To get enough signal on a camera exposure time of at least 100 µs is required. Because the exposure time introduces a systematic effect, we performed measurements at various values of exposure time and extrapolate the results to zero exposure.

Due to the very long and complicated procedure of loading, evaporating and transporting atoms from MOT into YAG dipole trap, both temperature, and density of resulting atomic cloud were always fluctuating. On Figure 3.5 we show an example of time-of-flight measurement. In every experiment, the density was monitored on the fly, and its results were used in data analysis. We calculate the density in two separate ways, using the atomic profile:

$$n = \frac{N}{(2\pi)^{3/2}} \frac{1}{\sigma_{0,x}\sigma_{0,y}\sigma_{0,z}}, \tag{3.1}$$

or using the temperature and dipole trap frequencies:

$$n = N \left(\frac{m\bar{w}^2}{2\pi \mathrm{k_B T}} \right)^{3/2}. \tag{3.2}$$

N is the number of atoms, σ are the Gaussian widths of the cloud and $\bar{\omega} = (\omega_x \omega_y \omega_z)^{1/3}$ is the effective dipole trap frequency.

Because our absorption imaging measures only $\sigma^0_{y/z}$ but using the parametric excitation technique we measured frequencies $[\omega_x, \omega_y, \omega_z]$=$2\pi\times$[0.61, 0.6, 0.1] kHz we use this to calculate the $\sigma_x = \sigma_y \frac{\omega_y}{\omega_x}$ and for temperature we assume that $T_x = T_y$.

3.2 Ion's experimental system

In Ion's chamber, we trap $^{88}\mathrm{Sr}^+$ ions in a linear segmented Paul trap. Inside this trap, Sr atoms are loaded from a home-build oven. The oven is heated to 100s of K in by passing a current through it. After the oven is heated the atomic beam directed towards the center of the trap emerges. Neutral Sr atoms are ionized with a combination of 405 nm and 461 nm nm laser beams (see Figure 3.6); Doppler cooled to 0.5 mK with a combination of 422 nm and 1092 nm lasers. Then using 674 nm narrow transitions, we detect and minimize the excess micromotion (EMM) and ground state cool them.

Our Paul trap has a linear segmented design (see Figure 3.7). The red electrodes generate an rf oscillating electric quadrupole field $(-\mathrm{q}, \mathrm{q}, 0)$. The green electrodes generate a static electric quadrupole field which traps the ion axially and anti-traps it radially $(-\mathrm{a}, -\mathrm{a}, 2\mathrm{a})$. The blue bias electrodes produce a radial electric field which lifts the degeneracy of radial modes$(-\mathrm{a}', \mathrm{a}', 0)$.

The trap is build of 0.5 mm thick titanium. Thin blades design allowed us to maintain the NA=0.38 numerical aperture needed for the ion's imaging system.

3.2.1 Doppler cooling

After ionization and trapping, the ion has temperature of 100s of Kelvin. We cool the ion with a 422 nm laser red-detuned from the $\mathrm{S}_{1/2} \rightarrow \mathrm{P}_{1/2}$ dipole transition, and 1092 nm repump laser on-resonance with the $\mathrm{D}_{3/2} \rightarrow \mathrm{P}_{3/2}$ dipole transition (see Figure 3.1). We cool the ion in two stages. First, off-resonance cooling utilizes 200 MHz red detuned 422 nm laser tuned to high power and then using on-resonance cooling which consists of low-power 422 nm laser tuned near a dark resonance. The off-resonance cooling is robust and fast but due to recoil heating cools the ion to few mK. The on-resonance cooling cools the ion to approximately $\sim 0.5\,\mathrm{mK}$. For a more detailed description of Doppler cooling and Doppler thermometry (see chapter 4).

3.2.2 Imaging system and detection

For imaging the Rb atoms and Sr^+ ions, we use a single bi-chromatic imaging system (see Figure 3.8). Achromatic objective has a focal distance of f=30 mm, numerical aperture of NA=0.38 and a long working distance of WD=16 mm. After the imaging system, the light is split with 90%/10% ratio. 10% of the light reaches slow EM-CCD for 422 nm ion's fluorescence imaging. The magnification of this Luca EM-CCD is x10.The remaining 90% is diverted with a dichroic mirror into either a photon multiplier (PMT) or a fast Pixelfly CCD camera. The pixelfly CCD camera is used for 780 nm absorption imaging detection and the fast PMT is used for 422 nm ion's fluorescence detection.

3.3 Narrow linewidth Rabi spectroscopy

The narrow linewidth 674 nm laser working on a quadrupole $\mathrm{S}_{1/2} \rightarrow \mathrm{D}_{3/2}$ transition is used to manipulate and measure the ion's motional and spin states. The meta-stable $\mathrm{D}_{3/2}$ state has a lifetime of 390 ms which allows for coherent manipulation of ion's electronic state. The static magnetic field (3 Gauss) allows us to spectroscopically separate individual Zeeman levels.

3.3.1 Light-atom interaction

The Hamiltonian of atom-ion interaction is composed of the electronic, motional and interaction parts. The electronic part defines the electronic levels involved in the interaction $\hat{\mathcal{H}}^{elec} = \hbar\frac{\omega_0}{2}\hat{\sigma}_z$. ω_0 is the energy difference between the two levels involved and $\hat{\sigma}_z$ is the Pauli operator.The motional part is a result of the Mathieu equations, neglecting the micromotion can be written as: $\hat{\mathcal{H}}_i^{motion} = \hbar\nu_i(\hat{a}_i\hat{a}_i^\dagger + \frac{1}{2})$.

Interaction part is $\hat{\mathcal{H}}^{int} = \frac{\hbar\Omega_0}{2}\sigma_z(e^{i(\mathbf{kx}-\omega t+\phi)}+e^{-i(\mathbf{kx}-\omega t+\phi)})$. ω is the laser frequency, k is the laser wave-vector, and Ω_0 is the Rabi frequency.

$$\hat{\mathcal{H}} = \hat{\mathcal{H}}^{elec} + \sum_{i=x,y,z} \hat{\mathcal{H}}_i^{motion} + \hat{\mathcal{H}}^{int}. \tag{3.3}$$

Moving into the interaction representation $\hat{\mathcal{H}}_{int} = e^{i/\hbar\hat{\mathcal{H}}_0^{\dagger}t}\hat{\mathcal{H}}e^{-i/\hbar\hat{\mathcal{H}}_0 t}$ where $\hat{\mathcal{H}}_0 = \hat{\mathcal{H}}^{elec}+\sum_{i=x,y,z}\hat{\mathcal{H}}_i^{motion}$ and neglecting fast oscillating terms $(\omega_0+\omega)$ (rotating-wave approximation) we obtain:

$$\hat{\mathcal{H}}_{int} = \frac{\hbar}{2}\Omega_0\hat{\sigma}_+ \exp\{i\sum_i \eta_i(\hat{a}_i e^{-i\nu_i t} + \hat{a}_i^{\dagger}e^{i\nu_i t})\}e^{i(\phi-(\omega-\omega_0)t)}. \tag{3.4}$$

$\hat{\sigma}_+ = \frac{1}{2}(\hat{\sigma}_x + i\hat{\sigma}_y)$ is the spin raising operator, $\eta_i = \mathrm{k}_i\sqrt{\frac{\hbar}{2m\nu_i}}$ is the Lamb-Dicke parameter, and Ω_0 is the Rabi frequency of the ground state cooled ion.

3.3.2 Resolved sideband cooling

Due to the $\hat{\mathcal{H}}_i^{motion}$ term the $\mathrm{S}_{1/2} \rightarrow \mathrm{D}_{5/2}$ transition can be addressed when the 674 nm laser is detuned by the sum of integer multiples of various ion's secular frequencies $\omega_0 - \omega = n_x \cdot \nu_x + n_y \cdot \nu_y + n_z \cdot \nu_z$ where $\{n_x, n_y, n_z\} \in \mathbb{Z}$. It can be shown that the first order sidebands where $|n_x| + |n_y| + |n_z| = 1$ emerge from Equation 3.4 if $\eta_i \ll 1$.

$$\hat{\mathcal{H}}_{int} \approx \frac{\hbar}{2}\Omega_0\hat{\sigma}_+\{1 + i\sum_i \eta_i(\hat{a}_i e^{-i\nu_i t} + \hat{a}_i^{\dagger}e^{i\nu_i t})\}e^{i(\phi-(\omega-\omega_0)t)}. \tag{3.5}$$

This is called Lamb-Dicke regime and is valid when the size of ion's wavefunction is smaller than the laser wavelength.

By tuning the 674 nm laser on $\mathrm{S}_{1/2} \rightarrow \mathrm{D}_{5/2}$ transition we excite the carrier transition. Such an excitation does not change the motional state of the ion $|n, S\rangle \rightarrow |n, D\rangle$. If the laser is tuned to one of the sidebands $\omega_0 - omega = \pm\nu_i$ (see Figure 3.9), these transitions involve the change in the motional quanta of the ion: $|n, S\rangle \rightarrow |n \pm 1, D\rangle$. For the red sidebands, the laser is red-detuned from carrier transition, and these transitions involve a decrease of motional quanta. We use these transitions for ground-state cooling the ion. Because the Lamb-Dicke parameter in our trap is around $\eta \approx 0.1$ the second order sidebands are also detectable (see Figure 3.9).

3.3.3 Optical pumping

The static magnetic field causes the degeneracy of both Rb atom and Sr^+ ion Zeeman states. The 3 Gauss magnetic field that we use causes splitting on the order of a few MHz. The narrow linewidth 674 nm laser (20 Hz) allows us to manipulate individual Zeeman states (see Figure 3.10). For optical pumping of the ion to its Zeeman ground-state $S_{1/2}$(m=-1/2), we pulse the 674 nm laser on the $S_{1/2}$(m=1/2)→$D_{5/2}$(m=-3/2) and a 1033 nm repump laser on the $D_{5/2}$ →$P_{3/2}$ transition. After repeating these two pulses several times, the ion's population is pumped to the $S_{1/2}$(m=-1/2) Zeeman ground-state with $> 99.9\%$ fidelity.

3.3.4 Rabi thermometry

Besides using the 674 nm laser for cooling the motional and controlling the spin states of the ion, we can also use it for measuring these states, i.e., ion thermometry. In Equation 3.4 Ω_0 is the Rabi frequency for $n_x = n_y = n_z = 0$. The transitions that do not change the motional states (carrier transition) but the ion is not in the ground state the Rabi frequency is:

$$\Omega_{n_x n_y n_z} = \Omega_0 \prod_i e^{-\frac{\eta_i^2}{2}} \mathrm{L}_{n_i}\left(\eta_i^2\right). \tag{3.6}$$

$\mathrm{L}_n(x)$ is the Laguerre polynomial of n-th degree, $\mathrm{L}_n(x) = \sum_{m=0}^{n} (-1)^m \binom{n}{n-m} \frac{x^m}{m!}$.

With the ion in the ground state, the population in D-level during the Rabi experiment evolves in time as $P_D(t) = \sin^2(\Omega_0 t)$. When the ion is in the thermal state which is a mixture of different vibrational states, the population evolves as

$$\mathrm{P}_D(t; \bar{n}_x, \bar{n}_y, \bar{n}_z) = \sum_{n_x, n_y, n_z} \mathrm{P}_{\bar{n}_x}(n_x) \mathrm{P}_{\bar{n}_y}(n_y) \mathrm{P}_{\bar{n}_z}(n_z) \sin^2(\Omega_{n_x n_y n_z} t). \tag{3.7}$$

Here, $\mathrm{P}_{\bar{n}_i}$ are the probabilities to occupy the n-th level $\mathrm{P}_{\bar{n}_i}(n_i) = \frac{1}{\bar{n}_i + 1} \left(\frac{\bar{n}_i}{\bar{n}_i + 1} \right)^{n_i}$.

For the ground state cooled ion or for the ion in a well-defined Fock state the Rabi flop curve follows a sine trajectory. However for a thermal distribution we observe a dephasing which is faster for higher temperatures. From the time evolution of the dephasing we can extract the ion's temperature (see Figure 3.11).

3.3.5 Micromotion compensation

Micromotion was discussed in section 2.3. Here we show how this micromotion can be detected using laser spectroscopy. The effect of micromotion on Rabi spectroscopy can be analyzed by moving into the reference frame of the ion. If the ion oscillates with rf frequency of the Paul trap Ω_{rf}: $\mathbf{k} \cdot \mathbf{u}_{\mathrm{EMM}}(t) = \beta \cos(\Omega_{rf} t + \delta)$, where we define β as the modulation index:

$$\beta = \sqrt{\left(\sum_i \mathrm{k}_i \mathrm{u}_i^{\parallel} \right)^2 + \left(\sum_i \mathrm{k}_i \mathrm{u}_i^{\perp} \right)^2}, \tag{3.8}$$

with a phase shift $\delta = \tan^{-1}\left(\frac{\sum_i \mathrm{k}_i \mathrm{u}_i^{\perp}}{\sum_i \mathrm{k}_i \mathrm{u}_i^{\|}}\right) - \frac{\pi}{2}$.

In Equation 3.8, the micromotion is decomposed to in-phase $|\mathbf{u}^{\|}|$ and quadrature $|\mathbf{u}^{\perp}|$ components. The electric field from ion's point of view is [5]:

$$\mathbf{E}(t) = \mathrm{Re}[\mathbf{E}_0 \exp\left(i\mathbf{k}\cdot(\mathbf{u}_0 + \mathbf{u}_{\mathrm{EMM}}) - i\omega + \phi\right)]. \tag{3.9}$$

From Equation 3.9 we see that we can excite the $\mathrm{S}_{1/2} \rightarrow \mathrm{D}_{5/2}$ transition by detuning the laser by $\omega = \omega_0 \pm \Omega$. The modulation index β which determines the amplitude of micromotion is measured by measuring the Rabi frequency of first-order micromotion sideband Ω_1:

$$\frac{\beta}{2} \approx \frac{\Omega_1}{\Omega_0} = \frac{\mathrm{J}_0(\beta)}{\mathrm{J}_1(\beta)}. \tag{3.10}$$

The presence of radial dc electric fields $\mathbf{E}_{\mathrm{dc}}$ in the center of the trap causes the misalignment of the ion from the trap center where the ion experiences micromotion.

$$\mathbf{u}_i^{\|} = \frac{e\mathbf{E}_{\mathrm{dc}\cdot\hat{u}_i}}{m\omega_i^2}\frac{q_i}{2} \tag{3.11}$$

This formula relates the $\mathbf{u}_{\mathrm{EMM}}$ with the stray electric field in the center of the trap. Using Equation 3.8 and Equation 3.10 we see that by maximizing the Ω_1 we minimize the DC electric field in the center of the trap. On Figure 3.12 we see the linear dependence of excess micromotion amplitude on the compensation voltage electrodes as predicted by Equation 3.11.

With the method described above, we only detect the projection of micromotion on the laser's k-vector. To compensate micromotion in all spatial dimensions, we use three 674 nm detection beams, where each beam detects the projection of EMM amplitude along its direction.

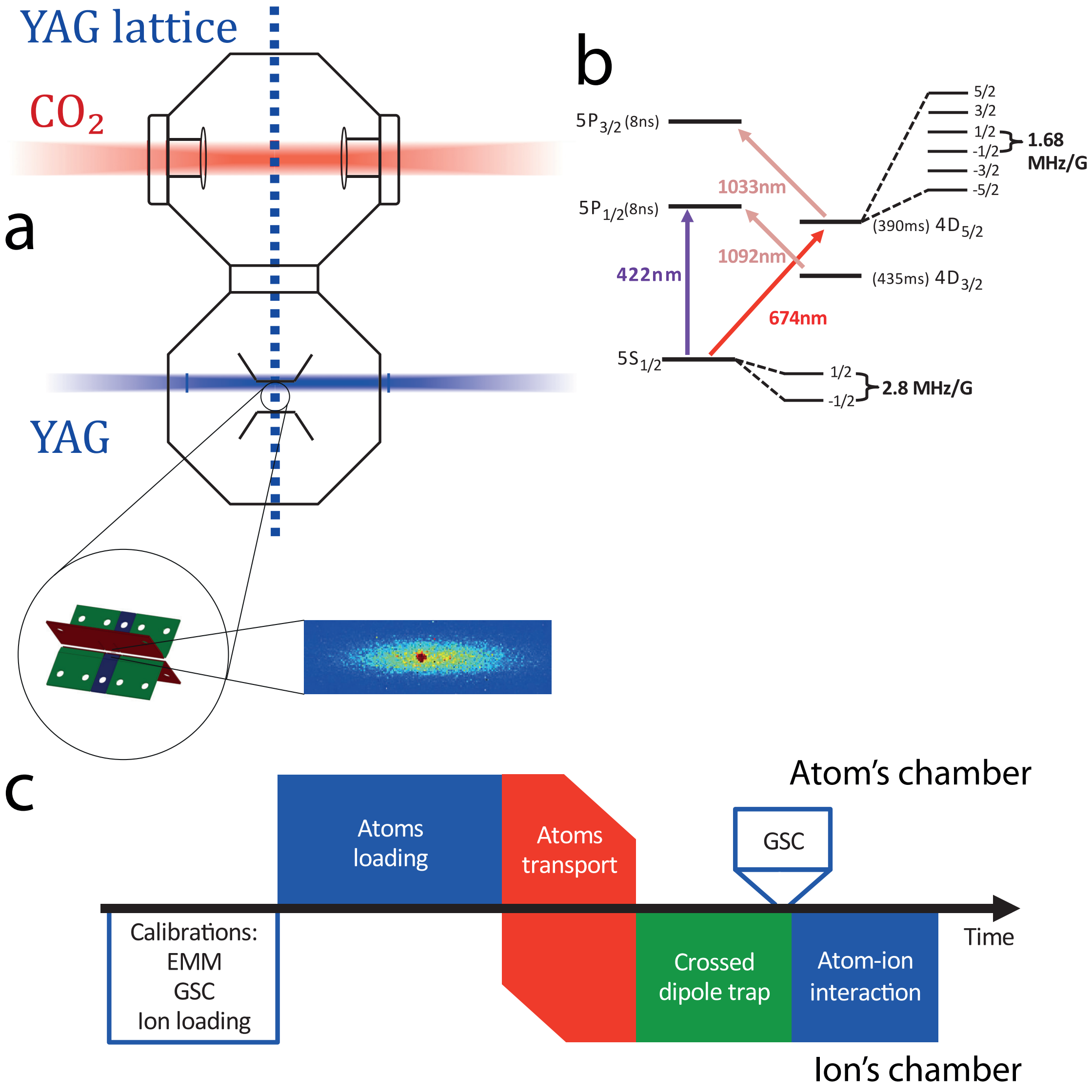

Figure 3.1: a) A schematic layout of experimental apparatus. The left inset shows the segmented linear ion trap. The right inset shows trapped ion inside an ultracold bath of atoms. b) $^{88}\mathrm{Sr}^{+}$ energy levels. Doppler cooling and fluorescence detection is performed on $S_{1/2} \rightarrow D_{5/2}$ transition at 422 nm. Repump lasers are working at 1092 nm and 1033 nm to depopulate the D levels. The Zeeman structure of S and D states is also shown. 422 nm narrow laser addressing is used to manipulate the state of an ion on this structure.c) The experimental sequence which includes Ion loading, Excess micromotion compensation (EMM), ground state cooling (GSC) performed in ion's chamber. Atoms loading and transporting from atom's chamber to ion's chamber. Transfering atoms into YAG crossed dipole trap during which ground state cooling continues and finally overlapping atoms and ion.

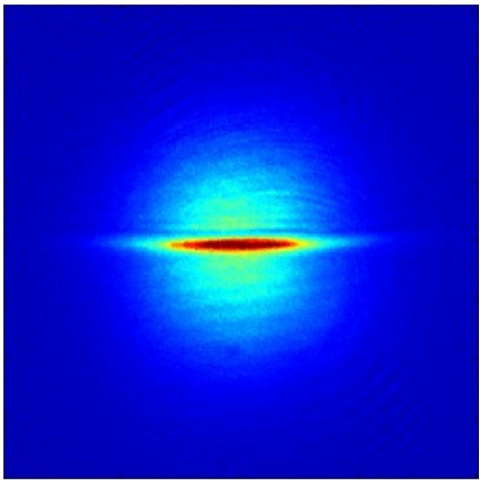

Figure 3.2: An absorption image of ^{87}Rb atoms loaded into the CO2 dipole trap. The waist of the CO2 beam is 26 µm and the Rayleigh range is 0.2 mm. We can load 10^6 atoms with temperature 170 µK. After evaporation, we can reach 0.2 µK with 10^5 atoms.

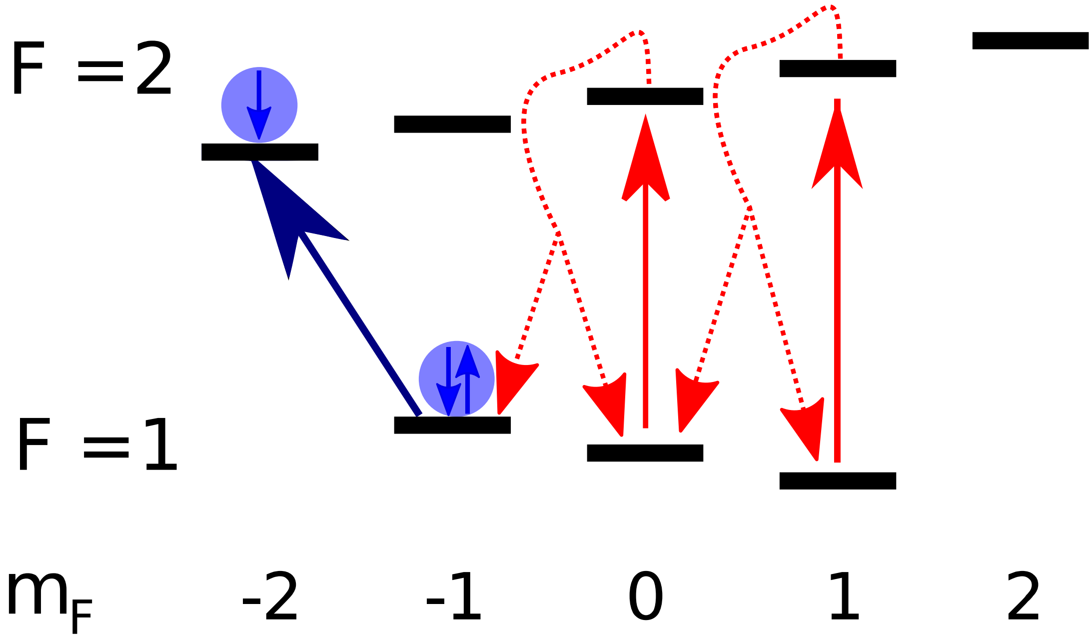

Figure 3.3: Experimental procedure for pumping the Rb atoms into a selected hyperfine state.

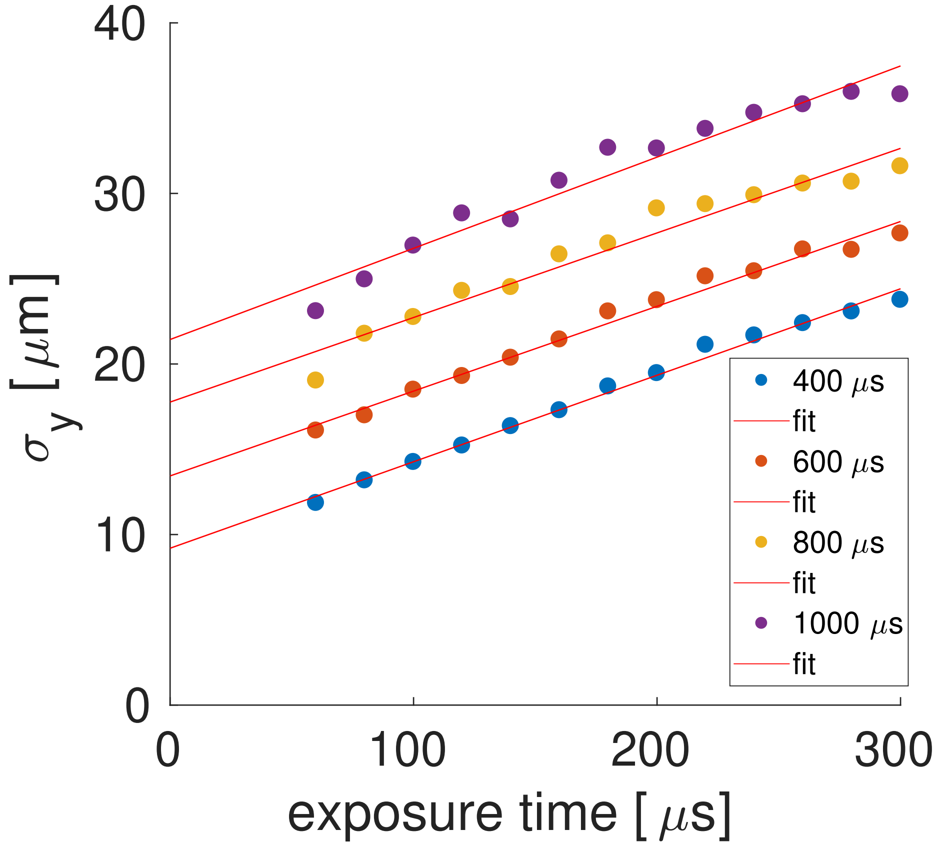

Figure 3.4: Time-of-flight measured width of atom's cloud as a function of camera exposure time. These data are used to extrapolate σ and eliminate the effect of finite exposure time.

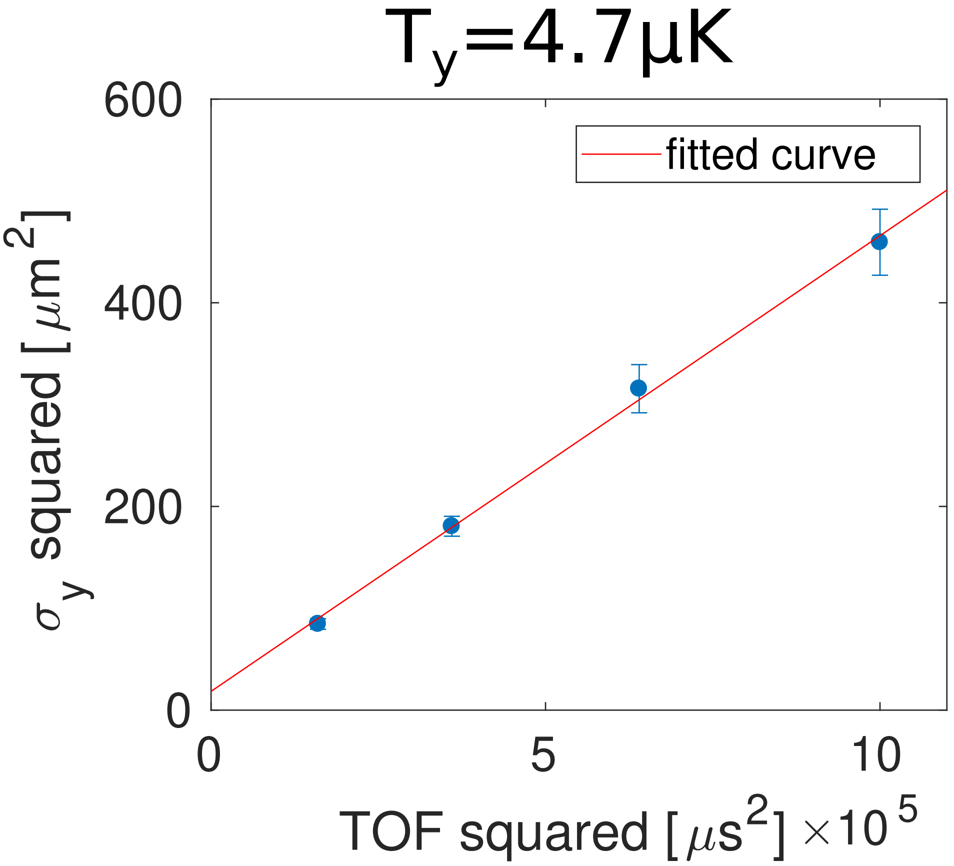

Figure 3.5: Time-of-flight measurement of the properties of Rb atomic cloud. Both temperatures $T_{y/z}$ and Gaussian widths $\sigma^0_{y/z}$ are extracted for every axis from this measurement.

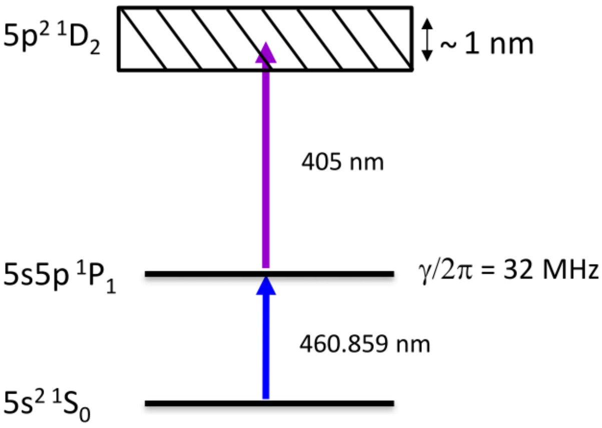

Figure 3.6: Level structure of relevant energy levels of ^{88}Sr atom that are used for ionization.

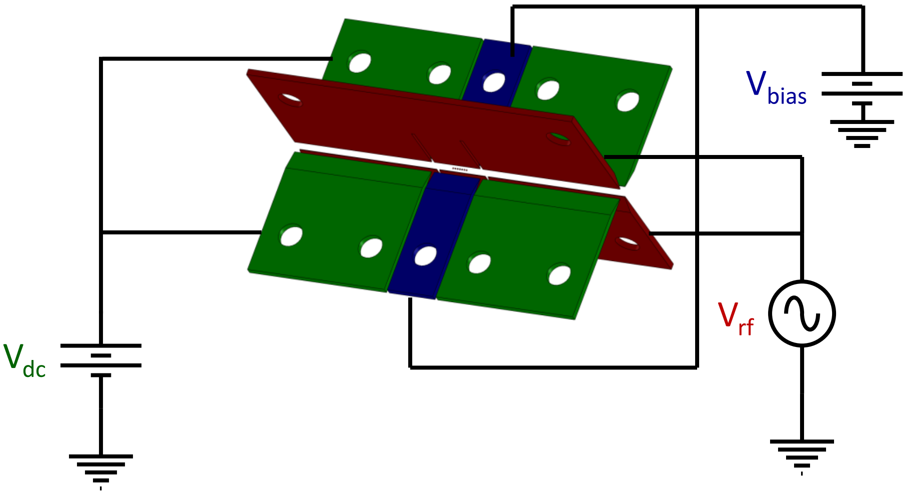

Figure 3.7: CAD model of Paul trap electrodes.

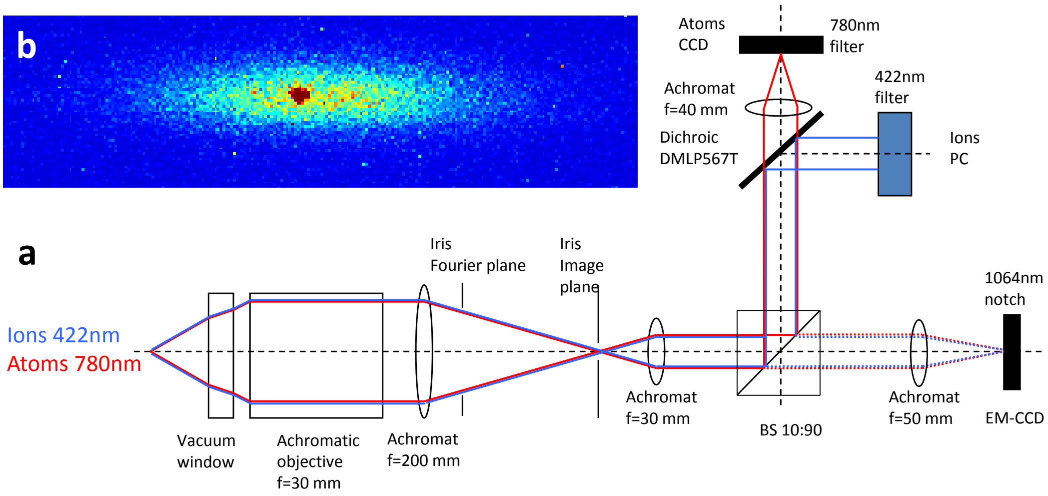

Figure 3.8: a) A diagram of the absorption and fluorescence imaging systems. b) Fluorescence imaging picture of single ion overlapped with the atoms cloud.

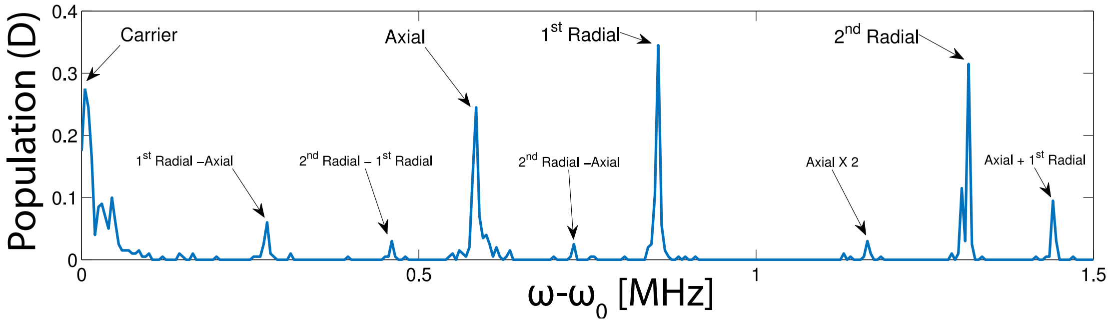

Figure 3.9: Ions secular motional modes spectroscopy. We scan the detuning of the 674 nm laser and measure the population in the D state. Each peak in the spectrum corresponds to a specific combination of secular modes (see Equation 3.4).

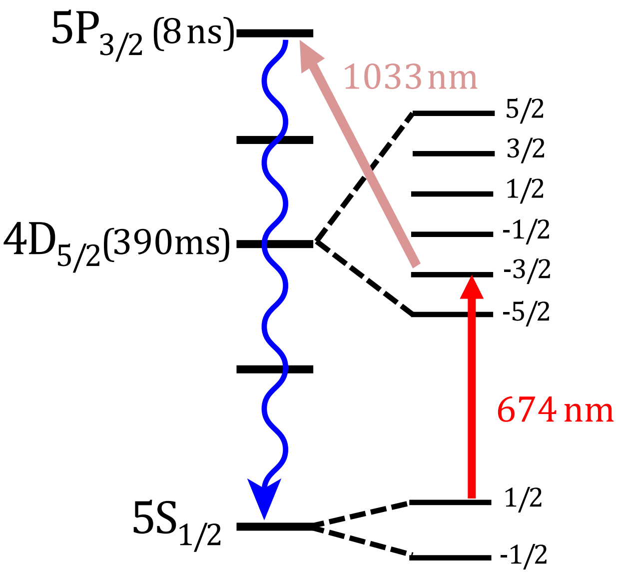

Figure 3.10: Optical pumping scheme. The population in $5S_{1/2}$(m=1/2) is coherently transferred into $5P_{3/2}$ state where it spontaneously decays back to $5S_{1/2}$. After repeating this procedure several times the ion is pumped into $5S_{1/2}$(m=-1/2) state.

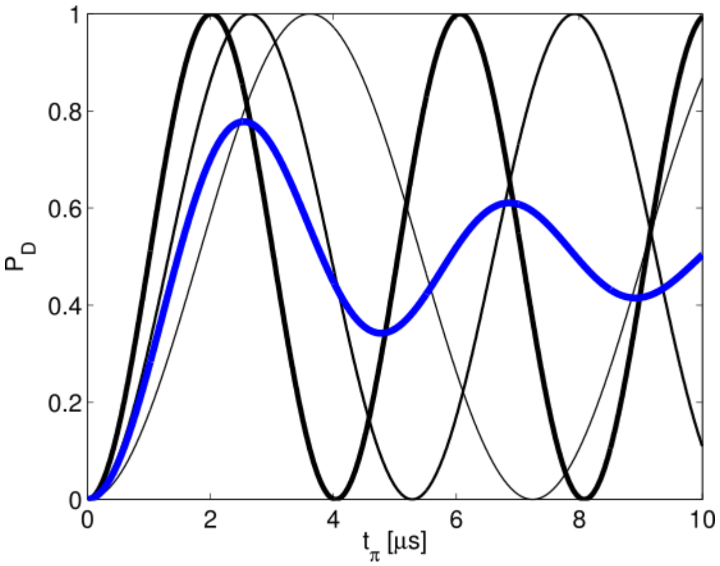

Figure 3.11: An example of Rabi flop thermometry calculation. The black lines are the Rabi flops for Fock states of different n_i. In blue we have an averaged Rabi flop. We see that averaging causes decay of oscillations. For higher temperature, the oscillations decohere faster.

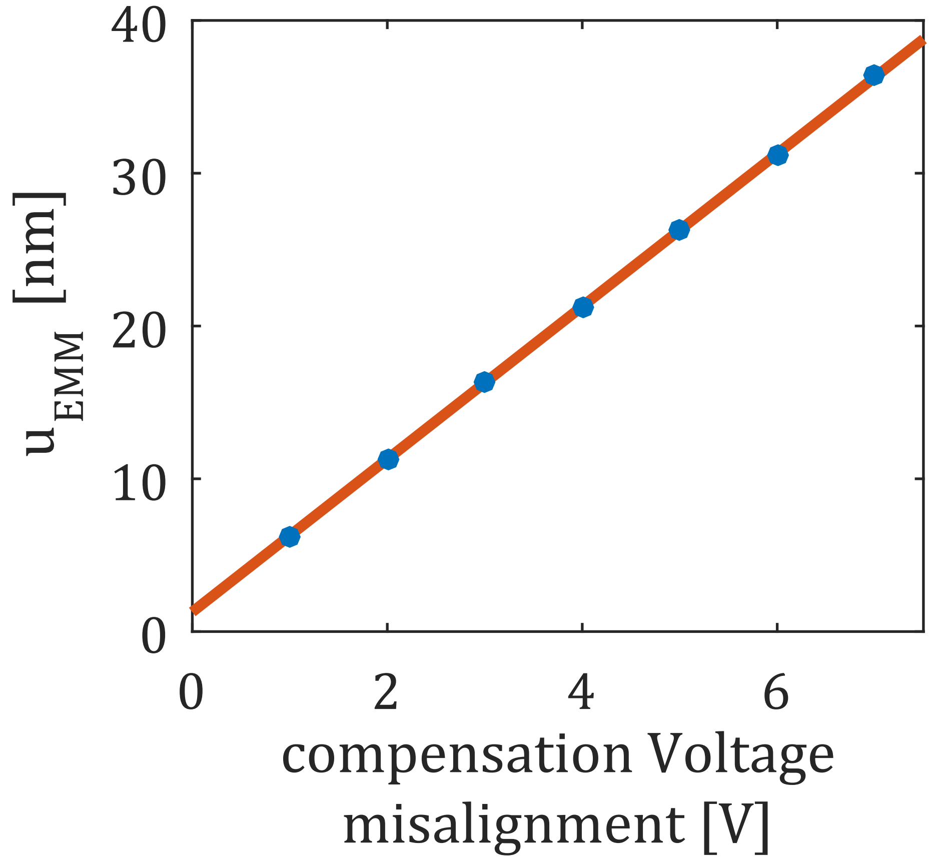

Figure 3.12: $\mathbf{u}_{\mathrm{EMM}}$ as a function of the relative compensation voltage (0 represents the compensated value). To compensate the radial excess micromotion we use two separate beams working on the $S_{1/2}(-1/2) \rightarrow D_{5/2}(-5/2)$ transition.The nonvanishing value of EMM is due to rf-Zeeman induced systematic shift [46]. Errorbars are too small to be presented in this figure.

Chapter 4

Doppler cooling thermometry[1]

The 674 nm Rabi thermometry described in the subsection 3.3.4 is suitable for energies up to few mK. Above these energies the Rabi flob oscillations decohere very fast, disallowing us to extract the temperature from the flop. In order to measure the ion energy above a few mK, we used a Doppler effect on dipole-allowed transition. $S_{1/2} \rightarrow P_{1/2}$ transition the has a line-width of 20.4 MHz and is suitable to be used for ion thermometry in range of 10's mK to 10's K. Below 10 mK Doppler shifts are too small to induce an appreciable change to the scattering rate, thus Doppler cooling thermometry loses its sensitivity.

Doppler cooling is based on the fact that if the cooling laser is red-detuned from the transition, an atom moving against the laser propagation direction has a higher probability of scattering photons than an atom moving along the laser direction. Photon scattering thus cools the atom until it reaches the Doppler temperature limit, typically in the mK range,

$$T_{\mathrm{Doppler}} = \frac{\hbar\gamma}{2k_{\mathrm{B}}}, \tag{4.1}$$

γ is a natural linewidth of cooling transition.

Doppler cooling thermometry is based on the fact that the ions' kinetic energy influences the fluorescence rate due to the Doppler effect. The time dependence fluorescence during Doppler cooling of an initially hot ion was proposed and demonstrated as a tool for the evaluation of the ion energy [22, 71]. This method applied for ions thermometry in many works [27, 2, 7, 66, 79, 33, 69, 78, 1, 17]. The Doppler cooling thermometry used in these experiments assumes a simple two-level cooling transition. However, in many of these experiments, the cooling transition involved multiple levels in a Λ transition structure. The use of a two-level model produces

---

[1] This chapter is based on the article [63]: Sikorsky, Tomas, et al. "Doppler cooling thermometry of a multilevel ion in the presence of micromotion." *Physical Review A* 96.1 (2017): 012519.

inaccurate results. We extended this method to multilevel atoms and also take into account the effect of micromotion in both strong and weak binding regime.

4.1 Two-level system

For a two-level system, the steady state scattering rate can be expressed analytically. When the ion is placed into a polarized laser beam resonant with $\mathrm{S}_{1/2} \rightarrow \mathrm{P}_{1/2}$ transition the steady state population of the excited state is given by:

$$\rho_{ee} = \frac{{}^{s}\!/_{2}}{1 + s + \left(\frac{2(\delta+\delta_D}{\Gamma}\right)^2}. \tag{4.2}$$

s is the saturation parameter, δ is the detuning, and δ_D is the Doppler shift $\delta_D = -\mathbf{k} \cdot \mathbf{v}$. The scattering rate is proportional to steady-state population $\frac{\mathrm{d}N}{\mathrm{d}t} = \Gamma \rho_{ee}$. The scattering rate is, therefore, temperature dependent. To measure this scattering rate experimentally, the ion needs to scatter thousands of photons and this scattering effects the temperature of the ion. This is one of the many examples in physics where the measurement significantly affects the measured quantity.

To determine the initial temperature of an ion, we monitor the fluorescence of an initially hot ion. The ion interacts with red detuned polarized laser beam. As the ion scatters photons, its temperature is decreasing towards the cooling limit, and its fluorescence rate is increasing. We developed a model describing the time dependence of a fluorescence rate. From this model, we obtain the initial temperature of an ion.

Consider a ${}^{88}\mathrm{Sr}^{+}$ ion trapped in a 3D harmonic potential of frequencies ω_i ($i = x, y, z$). The ion is in the weak binding regime ($\Gamma_{422} >> \omega_i$) where the line-width of the transition (20.4 MHz) is more than an order of magnitude lower than trapping frequencies ($\omega_i \sim 1\,\mathrm{MHz}$). We consider an event where an ion scatters a photon. From conservation of energy and momentum, we can show that the energy of an ion in each mode ($i = x, y, z$) will change by:

$$\Delta E_i = \hbar \left(k_i^{inc} - k_i^{scatt}\right) v_i + \frac{1}{3} \frac{\left(\hbar \left|k\right|\right)^2}{2m} \left(\hat{k}^{inc} - \hat{k}^{scatt}\right)^2. \tag{4.3}$$

Here, v_i is the initial velocity of the ion, k_i^{inc} is the incident photon k-vector and k_i^{scatt} is the scattered photon k-vector projected on the i-th axis. In the non-relativistic limit, the magnitude of the k-vector changes by order of $\sim v/c$ which is small and can be neglected. Since the re-scattered photon is isotropically emitted [41], we can integrate k_i^{scat} over all scattering angles and Equation 4.3 simplifies to,

$$\Delta E_i = \hbar k_i^{inc} v_i + \frac{2}{3} \frac{\left(\hbar \left|k\right|\right)^2}{2m}. \tag{4.4}$$

The cooling rate is now given by $\frac{\mathrm{d}E_i}{\mathrm{d}t} = \gamma\left(\mathbf{par}, \delta_D\right)\Delta E_i$, where γ is the instantaneous scattering rate which for two-level system is given by Equation 4.2. The scattering rate depends naturally on the Doppler shift, δ_D, and also on **par** which is a vector of experimental parameters such as laser frequencies and intensities and magnetic field. These parameters are energy independent and therefore do not change during the cooling process.

4.2 Eight-level system

Because the Doppler cooling scheme of Sr^+ ion involves 8-levels (see Figure 4.1) Equation 2.5 can no longer be used.

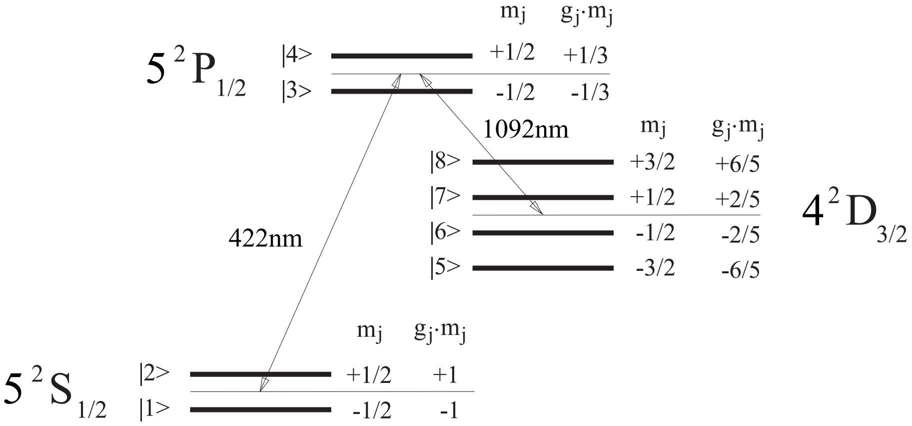

Figure 4.1: The level scheme of $^{88}\mathrm{Sr}^+$ with the Zeeman splitting relevant to the Doppler cooling model. g_j is the Lande factor.

To calculate the P state population $\rho_{P_{1/2}}$ as a function of laser power and temperature we numerically evaluate the steady-state solution of coupled Bloch equations for all involved levels with given laser couplings and decay channels (section 4.3). The levels of interest are the $5S_{1/2}$ ground-state and the $4D_{3/2}$ meta-stable state, with a lifetime of 390 ms. These levels are connected via allowed dipole transitions to the $5P_{1/2}$ excited state at transition wavelengths of 422 nm and 1092 nm respectively. The lifetime of the $5P_{1/2}$ level is 8 ns. Including all Zeeman states of these levels we obtain 64 coupled Bloch equations. We calculate the scattering rate, $\gamma = \Gamma\rho\left(P_{1/2}\right)$, from the steady-state population of the excited $5P_{1/2}$ states. To experimentally calibrate our laser parameters, we measure the scattering rate as a function of the 422 nm laser detuning (Figure 4.2). From a fit to the spectrum we find the Rabi frequencies and exact detuning of both lasers. As seen, the experimental data agrees well with the numerical solution.

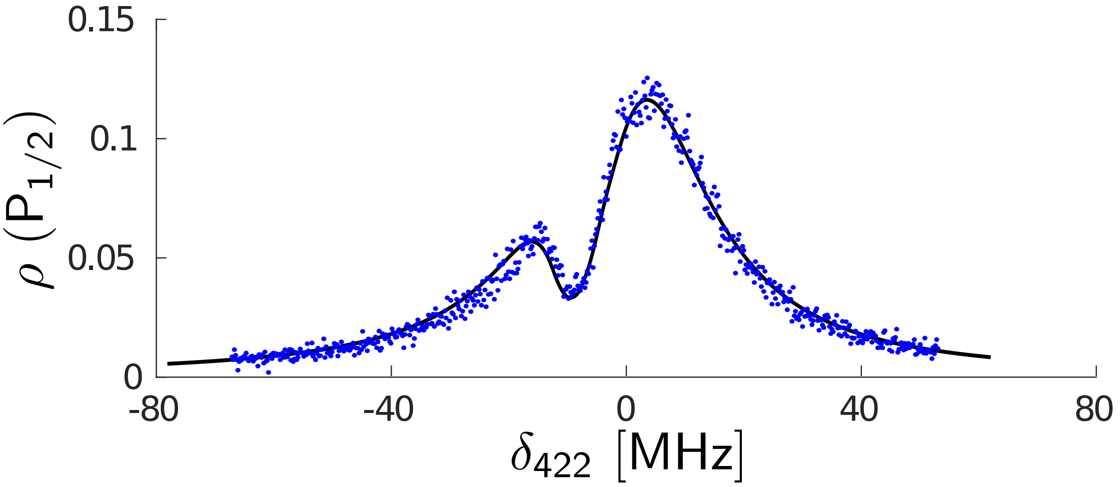

Figure 4.2: A spectroscopic scan of the $\mathrm{S}_{1/2} \rightarrow \mathrm{P}_{1/2}$ transition. The green line is ion fluorescence counts detected during a 1 µs long laser pulses as a function of the 422 nm laser detuning δ_{422}. We detect one out of ∼200 photons emitted by ion. The black line is a fit to the steady-state solution of the 8-level optical Bloch equations, which yields the following laser parameters: $\Omega_{422}/2\pi = 9.3 \pm 0.07$ MHz, $\Omega_{1092}/2\pi = 7.0 \pm 0.32$ MHz, $\delta_{1092} = -9.0 \pm 0.14$ MHz. A magnetic field of B=3.02 Gauss and laser polarizations were measured independently. The magnetic field was measured with a spectroscopy of the different Zeeman transitions of the $\mathrm{S}_{1/2} \rightarrow \mathrm{D}_{5/2}$ transitions. The 422 nm and 1092 nm beams polarizations were measured to be 0 and 45 degrees to the magnetic field respectively.

After obtaining all laser parameters, we calculate the ion scattering rate as a function of the Doppler shift. Here the Doppler shifts from both transitions are related through $\delta_D = \delta_{422} = \frac{1092}{422}\delta_{1092}$, where, $\delta_{422} = \mathbf{k_{422}} \cdot \mathbf{v}$ and $\delta_{1092} = \mathbf{k_{1092}} \cdot \mathbf{v}$ and we assume that both lasers are co-linear. The solid green line in Figure 4.3 shows the calculated Doppler shifted spectrum of the ion.

4.3 Numerical solution of eight level coupled Bloch equations

In this section we follow the derivation of [51]. The Lindblad master equation gives the time evolution of the density operator $\hat{\rho}$:

$$\begin{aligned} \frac{\mathrm{d}\hat{\rho}}{\mathrm{d}t} &= \mathcal{L}[\hat{\rho}], \\ \mathcal{L} &= -\frac{i}{\hbar}\left[\hat{H}, \hat{\rho}\right] + \hat{D}. \end{aligned} \tag{4.5}$$

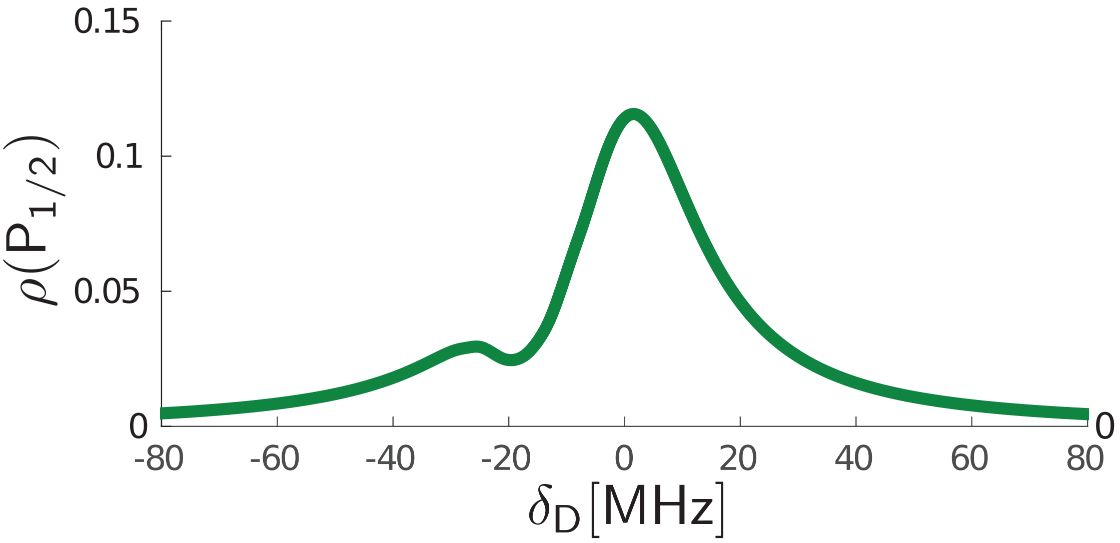

Figure 4.3: Excited state population $\rho(P_{1/2})$ as a function of the Doppler shift, $\delta_D = \delta_{422} = \frac{422}{1092}\delta_{1092}$. Laser parameters are the same as in the Figure 4.2.

Here, $\hat{H}$ is the Hamiltonian of the system and the $\hat{D}$ is a Lindblad operator describing non-unitary processes. In our case these are spontaneous decay and finite laser linewidths. Decay occurs from the P level to the S level and from the P level to the D level. The dissipative operator $\hat{D}$ has the form:

$$\hat{D} = -\frac{1}{2}\sum_i \hat{C}_i^\dagger \hat{C}_i \rho + \rho \hat{C}_i^\dagger \hat{C}_i - 2\hat{C}_i^\dagger \rho \hat{C}_i. \tag{4.6}$$

The damping terms, $\hat{C}_{1:6}$, describe spontaneous decay from the P level:

$$\begin{aligned}
\hat{C}_1 &= \sqrt{\frac{2}{3}\Gamma_{P\to S}}|1\rangle\langle 4|, & \hat{C}_4 &= \sqrt{\frac{\Gamma_{P\to D}}{6}}\left(\sqrt{3}|5\rangle\langle 3| + |6\rangle\langle 4|\right), \\
\hat{C}_2 &= \sqrt{\frac{2}{3}\Gamma_{P\to S}}|2\rangle\langle 3|, & \hat{C}_5 &= \sqrt{\frac{\Gamma_{P\to D}}{6}}\left(|7\rangle\langle 3| + \sqrt{3}|8\rangle\langle 4|\right), \\
\hat{C}_3 &= \sqrt{\frac{\Gamma_{P\to S}}{3}}\left(|1\rangle\langle 3| - |2\rangle\langle 4|\right), & \hat{C}_6 &= \sqrt{\frac{\Gamma_{P\to D}}{3}}\left(|6\rangle\langle 3| + |7\rangle\langle 4|\right).
\end{aligned} \tag{4.7}$$

Here, $|i\rangle$ are the eigenstates of the atomic Hamiltonian (Figure 2.3). $\Gamma_{P\to S} = 128\,\text{MHz}$ and $\Gamma_{P\to D} = 7.46\,\text{MHz}$ [77]. The effect of finite lasers linewidths is described by:

$$\begin{aligned}
\hat{C}_7 &= \sqrt{2\Gamma_{422}}\left(|1\rangle\langle 1| + |2\rangle\langle 2|\right), \\
\hat{C}_8 &= \sqrt{2\Gamma_{1092}}\left(|5\rangle\langle 5| + |6\rangle\langle 6| + |7\rangle\langle 7| + |8\rangle\langle 8|\right).
\end{aligned} \tag{4.8}$$

Γ_{422} and Γ_{1092} express the cooling and repump laser linewidths which are on the order of 100's of kHz. The atomic part of the Hamiltonian has the form:

$$\hat{H}_{atom} = \sum_{i}^{8} \hbar\omega_i |i\rangle\langle i| = \sum_{i=1}^{2} \hbar\omega_S |i\rangle\langle i| + \sum_{i=3}^{4} \hbar\omega_P |i\rangle\langle i| + \sum_{i=5}^{8} \hbar\omega_D |i\rangle\langle i|. \tag{4.9}$$

For co-propagating laser beams that are perpendicular to the magnetic field, the part of the Hamiltonian, $\hat{H}$, that describes the coupling between all eight eigenstates by two laser lights, have the following matrix elements:

$$\begin{aligned}
\hat{H}_{1,3} &= +\frac{1}{\sqrt{3}}\Omega_{422}\cos(\alpha)e^{i\omega_{422}t}, & \hat{H}_{1,4} &= -\frac{1}{\sqrt{3}}\Omega_{422}\sin(\alpha)e^{i\omega_{422}t},\\
\hat{H}_{2,3} &= -\frac{1}{\sqrt{3}}\Omega_{422}\sin(\alpha)e^{i\omega_{422}t}, & \hat{H}_{2,4} &= +\frac{1}{\sqrt{3}}\Omega_{422}\cos(\alpha)e^{i\omega_{422}t}\\
\hat{H}_{5,3} &= -\frac{1}{2}\Omega_{1092}\sin(\beta)e^{i\omega_{1092}t}, & \hat{H}_{5,4} &= 0,\\
\hat{H}_{6,3} &= -\frac{1}{\sqrt{3}}\Omega_{1092}\cos(\beta)e^{i\omega_{1092}t}, & \hat{H}_{6,4} &= -\frac{1}{2\sqrt{3}}\Omega_{1092}\sin(\beta)e^{i\omega_{1092}t},\\
\hat{H}_{7,3} &= +\frac{1}{2\sqrt{3}}\Omega_{1092}\sin(\beta)e^{i\omega_{1092}t}, & \hat{H}_{7,4} &= -\frac{1}{\sqrt{3}}\Omega_{1092}\cos(\beta)e^{i\omega_{1092}t},\\
\hat{H}_{8,3} &= 0, & \hat{H}_{8,4} &= +\frac{1}{2}\Omega_{1092}\sin(\beta)e^{i\omega_{1092}t}.
\end{aligned} \tag{4.10}$$

The Rabi frequencies, Ω_{1092} and Ω_{422} are defined as $\Omega = \frac{E\cdot D}{2\hbar}$. α and β are the linear polarization angles of the 422 nm and 1092 nm beams, respectively, to the magnetic field axis. ω_{422} and ω_{1092} are the laser beams frequencies. Finally, we move to the interaction representation using the unitary operator:

$$\hat{U} = \sum_{i=1}^{2} e^{-i\omega_{422}t}|i\rangle\langle i| + \sum_{i=5}^{8} e^{-i\omega_{1092}t}|i\rangle\langle i|. \tag{4.11}$$

In the interaction representation, $\hat{H}$ and ρ transform according to:

$$\hat{H}' = \hat{U}\hat{H}\hat{U}^\dagger - i\hbar\hat{U}\frac{\mathrm{d}\hat{U}^\dagger}{\mathrm{d}t}, \tag{4.12}$$

$$\rho' = \hat{U}\rho\hat{U}^\dagger. \tag{4.13}$$

The detunings are now included in $\hat{H}'$,

$$\begin{aligned}
\Delta_{422} &= \omega_{422} - (\omega_P - \omega_S),\\
\Delta_{1092} &= \omega_{1092} - (\omega_P - \omega_D).
\end{aligned} \tag{4.14}$$

To obtain the optical Bloch equations, we rewrite $\hat{\rho}'$ into a vector form:

$$\rho' = (\rho_{11}, \rho_{12}, ..., \rho_{87}, \rho_{88}) \tag{4.15}$$

In the vector notation we omitted the prime for clarity. The time evolution of the density matrix is now given by:

$$\frac{\mathrm{d}\rho_{rs}}{\mathrm{d}t} = \sum_{kj} L_{rs,kj}\rho_{kj}. \tag{4.16}$$

Here, L is the Liouville matrix that is given by:

$$L_{rs,kj} = -\frac{i}{\hbar}\left(\mathcal{H}_{rk}\delta_{js} - \mathcal{H}^{\dagger}_{js}\delta_{rk}\right) + \sum_{m} (C_m)_{rk}\left(C^{\dagger}_m\right)_{js}, \tag{4.17}$$

where $\mathcal{H} = \hat{H}' - \frac{i}{2\hbar}\sum_m \hat{C}^{\dagger}_m \hat{C}_m$.

To obtain the spectrum, the steady-state solution is required. This is obtained by solving the equation: $\sum_{kj} L_{rs,kj}\rho_{kj} = 0$.

4.4 Doppler cooling of a trapped ion

In previous sections, we evaluated the effect of ion's motion on the scattering rate $\frac{\mathrm{d}N}{\mathrm{d}T}$. In this section, we are going to look at the cooling rate.

4.4.1 Weak binding limit

Calculating the energy-time-dependent problem of the scattering rate of a trapped ion in a laser field is a computationally intensive task. One has to solve the optical Bloch equations for an eight-level system which are also coupled with motion due to Doppler shifts to get the cooling rate. To develop a computationally efficient model which also gives a physical insight into the dynamics of Doppler cooling, several approximations have to be made. The first approximation is that of weak binding, which assumes that level populations, and therefore the fluorescence rate, reach steady-state faster than the ion is moving in the trap. This approximation was also used in the case of a two-level ion [71, 22].

In the case of two-level atoms [71, 22] where the two levels are connected with a strong dipole transition (natural linewidth of several 10's MHz), the time scale over which populations reach steady state is given by the lifetime of the excited state and is independent of the laser intensity or detuning [50]. For a multi-level atom, Doppler cooling involves additional re-pump transitions; the 1092 nm transition in our case. Typically, these transitions have a natural linewidth about an order

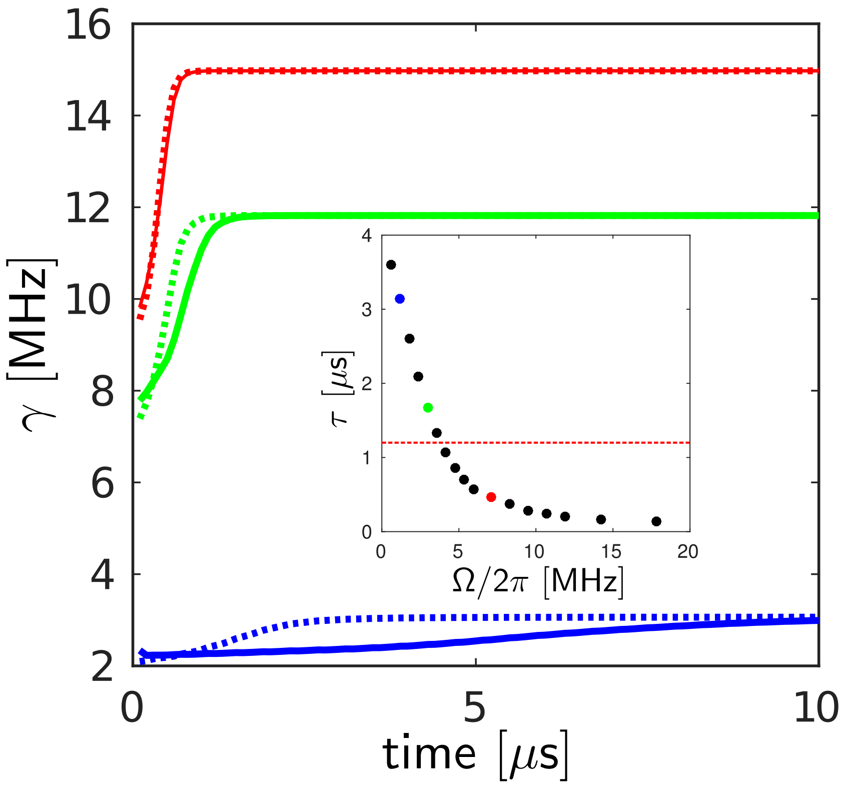

Figure 4.4: Comparison between the fluorescence rate predicted by OBS (solid lines) and Doppler cooling model (dashed lines). The initial energy in both methods is set to 1 K$\cdot$k$_B$ in the axial direction. We neglect recoil heating in this comparison. Different colors correspond to different repump Rabi frequencies. In the inset, we show the time scale in which the excited state reaches steady-state as a function of the repump Rabi frequency. Colored dots indicate the repump Rabi frequency used in the main figure. Red dashed line indicates the weak binding threshold: $\tau_{th} = \frac{2}{\omega} = 1.2\mu$s. Laser parameters are $\Omega_{422}/2\pi = 12.2$ MHz, $\Omega_{1092}/2\pi = 6.53$ MHz, $\delta_{422} = 0$ MHz and $\delta_{1092} = -7.7$ MHz. The magnetic field, laser polarizations, and linewidths are same as in Figure 4.2.

of magnitude smaller. The timescale over which populations reach steady state will depend on the intensity of the re-pump laser and will typically be an order of magnitude slower.

The timescale τ, in which the excited state reaches steady state depends greatly on the laser parameters. From a numerical solution of the eight-level Bloch equations, we observe that by saturating the $D_{3/2} \rightarrow P_{1/2}$ transition we can reduce τ and hence regain the weak-binding limit (inset of Figure 4.4). The timescale also depends on laser detuning and polarization. It is important to verify the validity of the weak binding approximation before using the Doppler cooling model.

To validate our model, we compare it with the result of an optical Bloch simulation (OBS) in which we do not assume steady state [44]. Instead, in OBS we obtain the instantaneous scattering rate by propagating in time the 64 coupled dynamical Bloch equations of the 8-level system together with the equations of motion of the ion in the presence of a scattering force [44]. The OBS is computationally very demanding and time-consuming which makes it impractical as a regular thermometry tool. Furthermore, the OBS does not provide any physical insight into the mechanisms that affect Doppler cooling. However, it does produce an exact result and can be used in regimes where the assumption of our model are no longer valid.

Figure 4.4 compares the photon scattering rate dynamics calculated by our model to the OBS result using different repump parameters. As expected, for weak repump intensities the weak-binding limit does not hold, and our model does not reproduce the OBS result, while for strong repump we see good agreement between the OBS and our model.

4.4.2 Harmonic trap

In this subsection, we concentrate on the effect of multi-level structure on Doppler cooling and ignore the effect of both inherent and excess micromotion. In linear Paul traps, the electric field in the axial direction is static. The simplified model of this section is appropriate for the determination of the ions' energy along the axial mode. The effects of micromotion and the extension of our model to motion in the radial directions are discussed in the subsection 4.4.3.

One dimensional treatment

First, we obtain a Doppler shift distribution for a particle in a 1D harmonic trap. Such particle undergoes a periodic motion resembling a classical harmonic oscillator:

$$\begin{aligned} x(t) &= Asin(\omega t), \\ v(t) &= \omega Acos(\omega t), \\ a(t) &= -A\omega^2 sin(\omega t). \end{aligned} \tag{4.18}$$

The amount of time $\mathrm{d}t$ a particle spends in a given velocity interval is $\mathrm{d}t = \frac{\mathrm{d}v}{\mathrm{d}v/\mathrm{d}t} = \frac{\mathrm{d}v}{a}$. The probability that the particle will be found in this region of $\mathrm{d}v$ is the ratio of the time it spends in this velocity to the time it takes to oscillate a half traversal. To get the probability distribution function as a function of velocity, we need to express acceleration as a function of velocity. For a harmonic oscillator, this is straightforward:

$$a = -A\omega^2\sqrt{1 - sin^2(\omega t)} = -A\omega^2\sqrt{1 - \left(\frac{v}{A\omega}\right)^2} = -\omega\sqrt{A^2\omega^2 - v^2}. \tag{4.19}$$

Because the maximum velocity that a particle obtains is $v_{max} = A\omega$, the probability distribution can be written as:

$$P(v) = \frac{1}{\pi\sqrt{v_{max}^2 - v^2}}. \tag{4.20}$$

Transforming from velocity distribution do a Doppler shift distribution $\delta_D^i = k_i v_i$ (seeFigure 4.3):

$$P_{\mathrm{1D}}^i\left(\delta_M^i, \delta^i\right) = \frac{1}{\pi\sqrt{(\delta_M^i)^2 - (\delta^i)^2}}. \tag{4.21}$$

Here, δ_M^i is the maximal Doppler shift for a given ion energy, E_i, in a given trap direction ($i = x, y, z$), $\delta_M^i = \frac{k_i}{2\pi}\sqrt{\frac{2E_i}{m}}$ and k_i is the projection of the laser k-vector on a given trap axis.

The scattering rate averaged over the motion for the 1D case is: (see Figure 4.3)

$$\frac{\mathrm{d}N}{\mathrm{d}t}\left(\delta_M^i, \delta\right) = \int \sigma_{free}\left(\delta_D^i, \delta\right) P_{1D}\left(\delta_M^i, \delta_D^i\right) d\delta_D^i. \tag{4.22}$$

Since the average energy change per scattering event is $-\delta_D$, the cooling rate is obtained using Equation 4.4:

$$\frac{\mathrm{d}E_i}{\mathrm{d}t}\left(\delta_M^i, \delta\right) = -\hbar\int \delta_D\sigma_{free}\left(\delta_D, \delta\right) P_{1D}\left(\delta_M^i, \delta_D\right) d\delta_D + \frac{2}{3}\frac{(\hbar k)^2}{2m}\frac{\mathrm{d}N}{\mathrm{d}t}. \tag{4.23}$$

Three-dimensional treatment

The ion is confined in a 3-D harmonic trap. The scattering rate is:

$$\frac{\mathrm{d}N}{\mathrm{d}t}\left(\delta_M^i, \delta\right) = \iiint \sigma_{free}\left(\sum_i \delta_D^i, \delta\right)\prod_i P_{1D}\left(\delta_M^i, \delta_D^i\right) d\delta_D^i. \tag{4.24}$$

It can be shown that this 3D integral can be transformed into a 1D integral. We use the fact that the Doppler shift is a scalar quantity and we define a scalar quantities $\delta_M^{x,y,z} = \delta_M^x + \delta_M^y + \delta_M^z$ and $\delta_D = \delta^x + \delta^y + \delta^z$. It is convenient to write a distribution of the Doppler shift in 3D as a function of a single scalar quantity δ_D and parameters $\delta_M^{x,y,z}$. Following the derivation of [71] we convolve the P_{1D}^i for all axis and obtain a 3D Doppler shift distribution Figure 4.5:

$$P_{3D}\left(\delta_M^{x,y,z}, \delta_D\right) = P_{1D}^x\left(\delta_M^x, \delta_D\right) * \left(P_{1D}^y\left(\delta_M^y, \delta_D\right) * P_{1D}^z\left(\delta_M^z, \delta_D\right)\right). \tag{4.25}$$

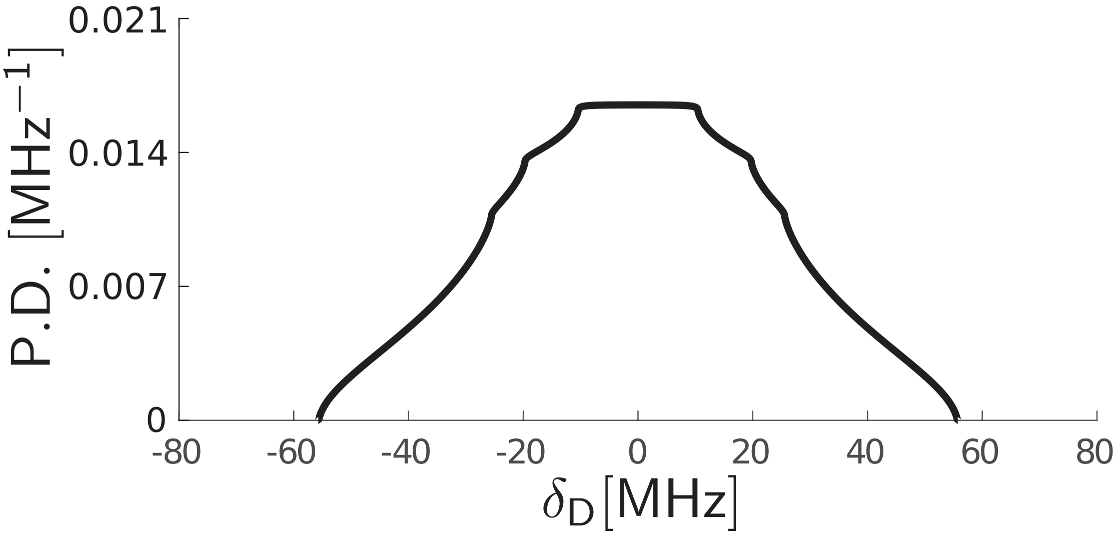

Figure 4.5: A combined Doppler shift distribution, P_{3D}, for an ion with 1 K energy in each axis ($E_x = E_y = E_z = 1$ K$\cdot$k$_\mathrm{B}$).

Integrating such 3D velocity distribution with Doppler-free line-shape, we obtain scattering rate as a function of $\delta_M^{x,y,z}$ and detuning from the resonance δ.

$$\frac{\mathrm{d}N}{\mathrm{d}t}\left(\delta_M^{x,y,z},\delta\right) = \int \sigma_{free}\left(\delta_D,\delta\right) P_{3D}\left(\delta_M^{x,y,z},\delta_D\right) d\delta_D. \tag{4.26}$$

The dashed line in Figure 4.5 shows the convolved 3D Doppler shift distribution for an ion with a 1 K $\cdot$ k$_\mathrm{B}$ energy in each direction. The average energy change per scattering event is $\hbar\mathbf{k_{422}}\cdot\mathbf{v} = \hbar\delta_D$. We use this fact and rewrite Equation 4.4 as,

$$\frac{\mathrm{d}E_i}{\mathrm{d}t}\left(\delta_M^{x,y,z}\right) = -\hbar\iiint \delta^i\cdot\frac{\mathrm{d}N}{\mathrm{d}t}\left(\delta_M^{x,y,z},\delta\right)\prod_{i=x,y,z} P_{\mathrm{1D}}\left(\delta_M^i,\delta^i\right) d\delta^x d\delta^y d\delta^z + \frac{2}{3}\frac{(\hbar k)^2}{2m}\gamma. \tag{4.27}$$

Equation 4.26 and Equation 4.27 together determine the time-dependent fluorescence rate of the ion during Doppler cooling. While Equation 4.27 determines the average change in energy per unit of time, Equation 4.26 is used to calculate the scattering rate as a function of energy.

Equation 4.27 takes into account only the momentum transfer due to the cooling light because the scattering rate contains information only on the 422 nm scattering. The repump light also imparts momentum on the ion, however, this effect is smaller by a factor of $\frac{|\mathbf{k_{1092}}|}{|\mathbf{k_{422}}|}\frac{\Gamma_{1092}}{\Gamma_{422}} \approx 0.02$. We can include this effect by scaling the $\gamma' \to \gamma\cdot\frac{\Gamma_{1092}}{\Gamma_{422}}$ and $\delta'^i \to \delta^i\cdot\frac{|\mathbf{k_{1092}}|}{|\mathbf{k_{422}}|}$ in Equation 4.27 and summing both contributions.

Equations 4.26 and 4.27 are inter-dependent, the scattering rate depends on energy, which is changing over the time the code solves the problem in discrete steps (50 µs). It is assumed that both the fluorescence rate and recooling rate are constant during this interval. We justify this discrete approach because the recooling process takes about 50 ms and the recooling scattering curves are smooth.

Experimental verification of the harmonic trap model.

To experimentally validate our model, we compare two different thermometry methods on a single $^{88}\mathrm{Sr}^{+}$ ion. We initialize the ion in a classical coherent state by driving the ion resonantly on the axial trap frequency ($\omega_{ax} = 417.5\ kHz$). We prepare the ion at different energies by changing the rf drive pulse length.

We perform Doppler cooling thermometry such that at the end of the ion's initialization, we turn on the cooling and repump lasers and monitor the ion's fluorescence for 10 ms with 30 μs binning. We repeat this process 200 times. In Figure 4.6 we show the experimental results together with a single parameter fit (initial energy) to the Doppler cooling model. The good agreement between the model and the experimental time-dependent fluorescence signal suggests that the ion was prepared in well-defined energy and that our model is valid.

To compare the results of Doppler cooling thermometry with an alternative thermometry method, we image the ion on a CCD camera and extract its energy from the shape of the intensity profile. For a 1D classical coherent state, the intensity profile is given by:

$$I\left(x\right) = \int_{0}^{\frac{2\pi}{\omega}} C \exp\left(-\frac{\left(x - A\cos\left(\omega t\right)\right)^{2}}{2\sigma^{2}}\right) \mathrm{d}t. \tag{4.28}$$

Here, σ is the width of our imaging system point-spread-function, and A is the ion's oscillation amplitude with frequency $\omega/2\pi$ from which we determine the energy of the ion: $E = \frac{1}{2} m A^{2} \omega^{2}$. We used on-resonance light such that Doppler shifts do not affect the ion's energy during detection. In the analysis, we neglect the Doppler shift effect on the intensity profile since we are interested only in the oscillation amplitude. To prevent any mechanical effects of laser light on the energy of the ion, we image the ion with low laser intensity ($\Omega_{422} \approx 0.1$ MHz) during 10 ms CCD exposures and repeat the measurement 5000 times to improve the signal-to-noise ratio. The experimental images are also shown in Figure 4.6.

A comparison between the energy extracted from the Doppler cooling fit and the CCD images for different energies are shown in Figure 4.6. There is a good agreement between energies obtained from these two methods.

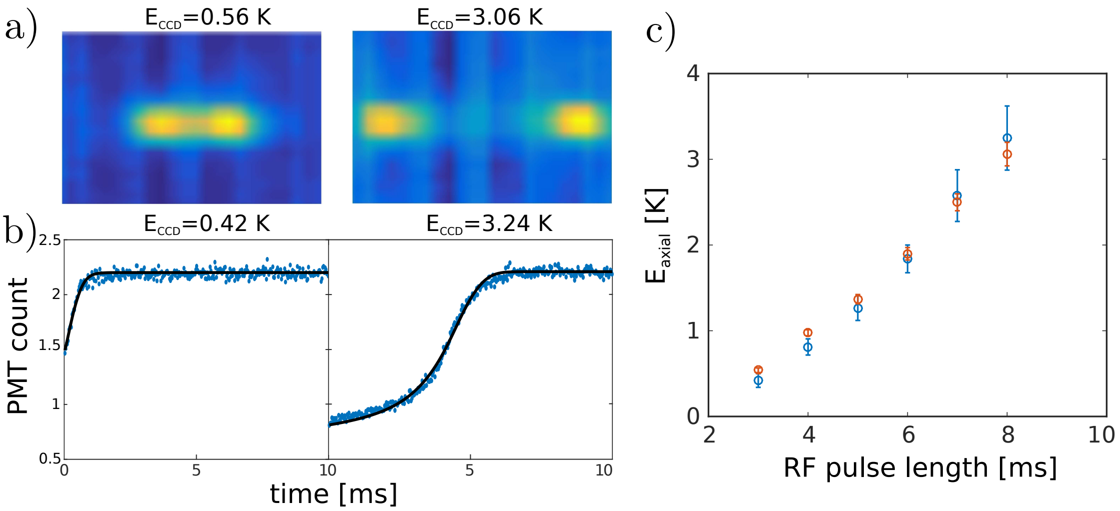

Figure 4.6: a) Time-averaged CCD images of an ion prepared in classical coherent states with different amplitudes. We extract the ions' energy by fitting the intensity profile to Equation 4.21. b) Experimentally measured ions' fluorescence during Doppler cooling (blue dots) for the same initialization as in a,b respectively. We extract the ion's energy from a single parameter fit (energy) to our model (black line). Laser parameters for the model are the same as in Figure 4.2. We set the 422 nm laser detuning to $\delta_{422} = -2.0$ MHz. c) A comparison between the two methods; Blue circles indicate energies derived from fitting the fluorescence signal of the Doppler cooling to our model and red circles are energies obtained from the intensity profile on the CCD. Error bars are 95% confidence intervals.

4.4.3 Paul trap

In the preceding sections, we discussed the dynamics of Doppler cooling in a static harmonic potential neglecting micromotion (see subsection 3.3.5). In Paul traps, the motion of the ion is a superposition of a slow frequency (ω_i) and fast frequency (Ω) Equation 2.40.

The micromotion velocity typically changes faster than the time in which the internal states of the atom reach steady-state, the absorption and emission of a photon cannot be localized in phase space, and the weak binding approximation does not hold. The analysis of the cooling process, therefore, requires a more involved approach.

Micromotion sidebands

Micromotion affects Doppler recooling by modifying the spectrum. Analogously with Equation 3.10, we move to the excess micromotion reference frame. In this reference frame, the ion still undergoes a secular motion, but there is no micromotion. This is an equivalent point of view because micromotion is driven motion and Doppler cooling will not affect it. Thus the effect of micromotion is viewed as a modulation of laser field:

$$\begin{aligned}\mathbf{E}\left(t\right) =&\mathbf{E_0}e^{i\left(\mathbf{k}\cdot\left[\mathbf{x_0}(t)+\frac{q}{2}\mathbf{A^{emm}}\cos(\Omega_{\mathrm{rf}}t)\right]-\omega_{laser}t\right)}\\ =&\mathbf{E_0}e^{[i\mathbf{k}\cdot\mathbf{x_0}(t)]}\sum_n J_n\left(\beta^{emm}\right)e^{i(n(\Omega_{\mathrm{rf}}t+\pi/2)-\omega_{laser}t)}.\end{aligned} \tag{4.29}$$

$\mathbf{x_0}(t)$ is the secular and inherent micromotion parts of the ion's motion and $\beta^{emm} = \frac{1}{2}\sum_{i=x,y} q_i k_i A_i^{emm}$ is the excess-micromotion modulation index. To first order in β^{emm}, excess-micromotion adds two sidebands to the ion spectrum at $\omega_{laser} \pm (\Omega_{\mathrm{rf}})$. Now we are going to look on the effect of inherent micromotion on the spectrum. The inherent micromotion part of $\mathbf{x_0}(t)$ modulates the electric field twice, once in the harmonic trap frequency ω_i and second in the rf frequency Ω_{rf}. The electric field in the presence of inherent micromotion can be written as:

$$\begin{aligned}\mathbf{E_0}e^{[i\mathbf{k}\cdot\mathbf{x_0}(t)]} =&\mathbf{E_0}\prod_i e^{ik_i\left(A_i^{sec}\cos\left(\omega_i t\right)+A_i^{sec}\frac{q_i}{2}\cos\left(\omega_i t\right)\cos\left(\Omega_{\mathrm{rf}}t\right)\right)}\\ =&\mathbf{E_0}\prod_i e^{ik_i\left(A_i^{sec}\cos\left(\omega_i t\right)+A_i^{sec}\frac{q_i}{4}\left(\cos\left((\Omega_{\mathrm{rf}}+\omega_i)t\right)+\cos\left((\Omega_{\mathrm{rf}}-\omega_i)t\right)\right)\right)}.\end{aligned} \tag{4.30}$$

In first order in the inherent micromotion modulation index, $\beta_i^{imm} = \frac{1}{4}q_i k_i A_i^{sec}$, this modulation adds four more additional sidebands at $\pm(\Omega_{\mathrm{rf}} \pm \omega_i)$ for each of the radial modes, $i = x(y)$. The modified spectrum is obtained by recalculating the spectrum with amplitudes of sidebands which are obtained from the Bessel series expansion as we did in Equation 4.29. The relative intensities of the inherent micromotion sidebands in first order can be expressed as a square of electric field components at frequency $\omega_{laser} \pm \Omega_{\mathrm{rf}} \pm \omega_{x(y)}$ (section 4.4.3). The scattering rate is calculated by using the modified spectrum in Equation 4.26.

Numerical solution of eight level coupled Bloch equations in the presence of micromotion

To calculate the spectrum of an ion in the presence of a micromotion sidebands, we need to modify the detunings that appear after transforming the Hamiltonian into a rotating frame in Equation 4.12.

$$\begin{aligned}\delta_{422} &= \omega_{422} - (\omega_P - \omega_S)\\ \delta_{1092} &= \omega_{1092} - (\omega_P - \omega_D)\end{aligned} \tag{4.31}$$

Sidebands appear because the laser detunings are modulated:

$$\begin{aligned}\delta_{422} &= \delta_{422}^{0} + k_{422}v_x^{inh}\left\{\cos\left(\left(\Omega+\omega_x\right)t\right)+\cos\left(\left(\Omega-\omega_x\right)t\right)\right\}\\ \delta_{1092} &= \delta_{1092}^{0} + k_{1092}v_x^{inh}\left\{\cos\left(\left(\Omega+\omega_x\right)t\right)+\cos\left(\left(\Omega-\omega_x\right)t\right)\right\}\end{aligned} \tag{4.32}$$

Here we treat the case of inherent micromotion due to motion along the x axis. $v_x^{inh} = \frac{q\Omega A_x^{sec}}{4}$

Because L is a linear matrix of the detunings, it is possible to separate the detuning by introducing unit Liouville matrices.

$$\begin{aligned}\Delta L_{422} &= L\left(1,0,par\right) - L\left(0,0,par\right)\\ \Delta L_{1092} &= L\left(0,1,par\right) - L\left(0,0,par\right)\end{aligned} \tag{4.33}$$

Where $L\left(\delta_{422},\delta_{1092},par\right)$ is a function of both detunings and all other laser parameters which are fixed. The modified Liouville matrix now gives the time evolution:

$$L = L_0 + 2\Delta L\left\{\cos\left(\Omega+\omega_x\right)t + \cos\left(\Omega-\omega_x\right)t\right\} \tag{4.34}$$

$$\Delta L = \frac{v_x^{inh}}{2}\left\{k_{422}\Delta L_{1092} + k_{1092}\Delta L_{422}\right\} \tag{4.35}$$

We will treat only first-order sidebands. In the long time we expect the solution with frequency components only at multiples of $\Omega+\omega_x$ and $\Omega-\omega_x$:

$$\rho = \rho_{0,0} + \rho_{1,0}e^{i(\Omega+\omega)t} + \rho_{-1,0}e^{-i(\Omega+\omega)t} + \rho_{0,1}e^{i(\Omega-\omega)t} + \rho_{0,-1}e^{-i(\Omega-\omega)t} \tag{4.36}$$

Combining eq. (20, 18 and 11) we get following equations for $\rho_{i,i}$.

$$L_0\rho_{0,0} + \Delta L\left(\rho_{1,0}+\rho_{-1,0}+\rho_{0,1}+\rho_{0,-1}\right) = 0 \tag{4.37}$$

$$\begin{aligned}\left(L_0 - i\left(\Omega+\omega\right)\right)\rho_{1,0} + \Delta L\rho_{0,0} &= 0\\ \left(L_0 + i\left(\Omega+\omega\right)\right)\rho_{-1,0} + \Delta L\rho_{0,0} &= 0\\ \left(L_0 - i\left(\Omega-\omega\right)\right)\rho_{0,1} + \Delta L\rho_{0,0} &= 0\\ \left(L_0 + i\left(\Omega-\omega\right)\right)\rho_{0,-1} + \Delta L\rho_{0,0} &= 0\end{aligned} \tag{4.38}$$

We can now express $\rho_{i,j}$ in terms of $\rho_{0,0}$

$$\begin{aligned}\rho_{1,0} &= -\Delta L\rho_{0,0}\left(L_0 - i\left(\Omega+\omega\right)\right)^{-1}\\ \rho_{-1,0} &= -\Delta L\rho_{0,0}\left(L_0 + i\left(\Omega+\omega\right)\right)^{-1}\\ \rho_{0,1} &= -\Delta L\rho_{0,0}\left(L_0 - i\left(\Omega-\omega\right)\right)^{-1}\\ \rho_{0,-1} &= -\Delta L\rho_{0,0}\left(L_0 + i\left(\Omega-\omega\right)\right)^{-1}\end{aligned} \tag{4.39}$$

Plugging Equation 4.39 into Equation 4.37 we can write the Liouville matrix as

$$L = L_0 - \Delta L^2 \left(\left(L_0 - i\left(\Omega + \omega\right)\right)^{-1} + \left(L_0 + i\left(\Omega + \omega\right)\right)^{-1} + \left(L_0 - i\left(\Omega - \omega\right)\right)^{-1} + \left(L_0 + i\left(\Omega - \omega\right)\right)^{-1} \right) \tag{4.40}$$

To compare with experiment, we fit the laser parameters to experimentally measured spectrum without excess micromotion. Then, we recalculate spectra adding the excess micromotion and compare it to experimental spectra with excess micromotion but same laser parameters Figure 4.7 (EMM amplitude is determined using 674nm narrow transition sideband spectroscopy). As seen, there is good agreement between the spectra obtained using our model and those obtained experimentally.

In the treatment above we approximated the effect of the micromotion by including the first-order sidebands only. We now examine the validity of this approximation at different ion temperatures and EMM levels. The optical power in each sideband is proportional to the square of the electric field amplitude at its frequency. This amplitude can be obtained by expanding Equation 4.30 into a Bessel series. $I_i^{j,k}$ is the electric field intensity at frequency of a corresponding i-th axis $|j| + |k|$ order sideband. The frequency can be expressed as $j\left(\Omega + \omega_i\right) + k\left(\Omega - \omega_i\right)$.

$$\begin{aligned}
I_x^{\pm1,0} &= \left(J_{\pm1}(\beta^x) \cdot J_0(\beta^x) \cdot J_0(\beta^y) \cdot J_0(\beta^y) \cdot J_0(\beta^{emm})\right)^2 \\
I_x^{0,\pm1} &= \left(J_0(\beta^x) \cdot J_{\pm1}(\beta^x) \cdot J_0(\beta^y) \cdot J_0(\beta^y) \cdot J_0(\beta^{emm})\right)^2 \\
I_y^{\pm1,0} &= \left(J_{\pm1}(\beta^x) \cdot J_0(\beta^x) \cdot J_{\pm1}(\beta^y) \cdot J_0(\beta^y) \cdot J_0(\beta^{emm})\right)^2 \\
I_y^{0,\pm1} &= \left(J_0(\beta^x) \cdot J_0(\beta^x) \cdot J_0(\beta^y) \cdot J_{\pm1}(\beta^y) \cdot J_0(\beta^{emm})\right)^2
\end{aligned} \tag{4.41}$$

.

The carrier power is given by,

$$I^{0,0} = \left(J_0(\beta^x) \cdot J_0(\beta^x) \cdot J_0(\beta^y) \cdot J_0(\beta^y) \cdot J_0(\beta^{emm})\right)^2 . \tag{4.42}$$

Since the Doppler cooling thermometry is usually performed below saturation, it is important to verify whether calculating the spectrum up to 1st order micromotion sidebands is sufficient. As a figure of merit, we verify that the sum of the Bessel functions Equation 4.43 up to first order is close to one. The sum of optical power vs. temperature is shown in Figure 4.8. As seen, up to a temperature of 1 K almost all optical power (>90%) is included by the first sideband approximation. Above 1 K more sidebands have to be included.

$$I = I^{0,0} + 2 \cdot \left(I_x^{1,0} + I_x^{0,1} + I_y^{1,0} + I_y^{0,1}\right) . \tag{4.43}$$

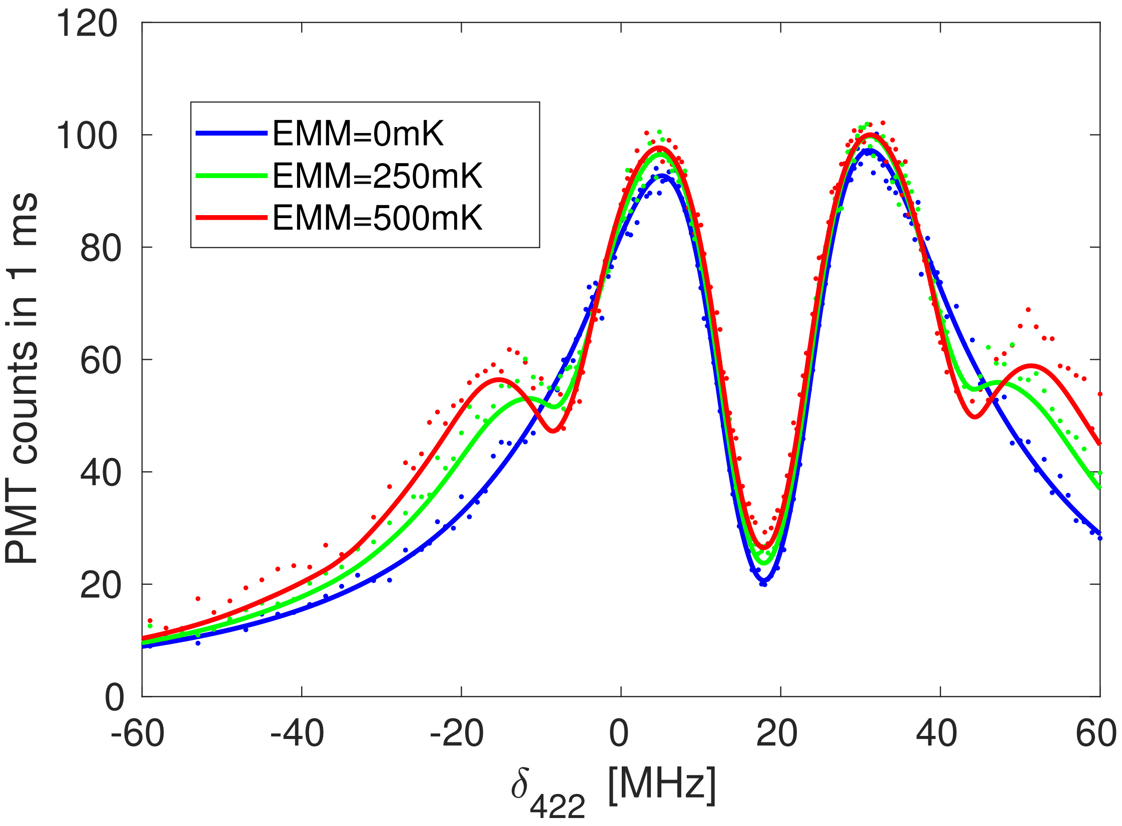

Figure 4.7: A spectroscopic scan of the $S_{1/2} \to P_{1/2}$ transition for various EMM. Points are the number of photons detected on a Photon-counter which is proportional to the excited state population. The solid lines are fit to the steady-state solution of the 8-level optical Bloch equations. Experimental parameters are: $\Omega_{422}/2\pi = 15.6 \pm 0.05$ MHz, $\Omega_{1092}/2\pi = 10.7 \pm 0.22$ MHz, $\delta_{1092} = -0.66 \pm 0.06$ MHz. These parameters are extracted from $EMM = 0$ (blue) fit. Beams polarizations are 6 and 35 degrees to the magnetic field for the 422 nm and 1092 nm laser respectively.

Experimental verification of the Paul trap model.

In section 4.4.3 we have shown how micromotion affects the scattering rate by adding sidebands. Here we will investigate the effect of these sidebands on Doppler recooling thermometry.

Similarly, to what we did in section 4.4, we compare our results to those of OBS. Extension of OBS from harmonic trap to Paul trap is straightforward [44]. In Figure 4.9 we compare the time evolution of fluorescence under Doppler cooling of an ion with initial energy $E = 1\ \mathrm{K} \cdot \mathrm{k_B}$ in the y direction calculated using OBS, and our model with and without including first-order micromotion sidebands. As

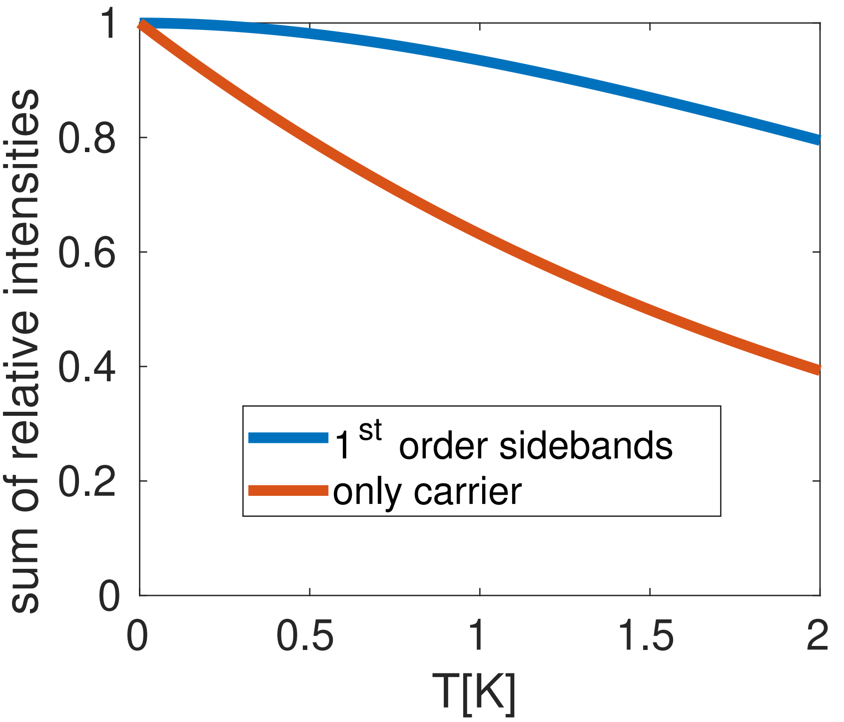

Figure 4.8: Proportion of a laser field captured by zero order (red) and first order (blue) Bessel series. We see that zero order becomes insufficient at temperatures above 0.2 K while first order treatment captures most of the power ($> 90\%$) at temperatures of 1 K. Above 1 K, second order sidebands are required. The trap frequencies are $\omega_{\mathrm{x}} = 0.73$ and $\omega_{\mathrm{y}} = 0.99$ MHz.

seen, incorporating micromotion sidebands is necessary for our model to better match with the OBS result. With the inclusion of higher-order sidebands, the agreement is expected to improve. The need to include higher order sidebands increases with higher initial energies.

As an application of our model we determine the energy distribution of an ion in two different cases. Generally, the ion is not found in a specific energy state but rather in a statistical distribution of energies, $P\left(E\right)$. The averaged scattering rate is obtained from our model by weighting the fluorescence curves according to the distribution,

$$\left\langle \frac{\mathrm{d}N}{\mathrm{d}t} \right\rangle = \int P\left(E\right) \left.\frac{\mathrm{d}N}{\mathrm{d}t}\right|_{E_0=E} \mathrm{d}E. \tag{4.44}$$

Here, we test our model with two different distributions (Figure 4.10). The thermal distribution, $P(E) \propto E^2 e^{-E/\mathrm{k_B}T}$, is produced by applying white voltage

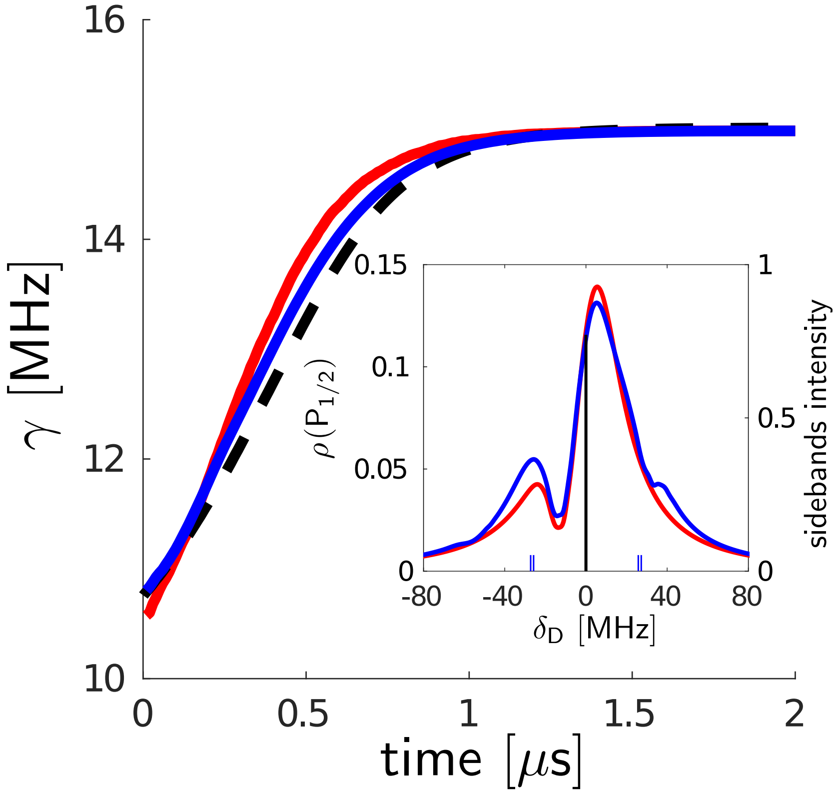

Figure 4.9: The effect of micromotion sidebands on the Doppler cooling fluorescence signal. Our model including 1^{st}-order micromotion sidebands (blue) is in good agreement with the OBS result (dashed black curve). The red curve is calculated without micromotion sidebands. The inset shows the effect of these sidebands on the spectrum. The red curve is the ions' spectrum without sidebands. The blue curve is the spectrum including micromotion sidebands. Vertical lines represent the position of the 422 nm carrier (black) and inherent micromotion (blue) sidebands. The height of the lines is proportional to their relative power J^2. The ion's energy is set to $E_y = 1\ \mathrm{K} \cdot \mathrm{k_B}$, $E_x = E_z = 0.001\ \mathrm{K} \cdot \mathrm{k_B}$. Laser parameters are the same as in Figure 4.2.

noise to one of the trap electrodes for one second. We determine the heating rate due to white noise using carrier Rabi spectroscopy on a narrow linewidth transition. The Rabi spectroscopy is performed at short heating times during which the ion heated up to temperatures up to 10 mK. We then linearly extrapolate the ion temperature for extended pulse times and compared this result to a direct measurement using Doppler cooling thermometry. The heating rate was measured by first preparing the ion in the ground state of all of its modes ($\bar{n} < 0.1$). During heating, we stopped ground state cooling on the mode of interest but continued to ground state cool on the remaining two modes. The extracted heating rates are: $[28 \pm 2, 393 \pm 19, 495 \pm 24]$ mK $\cdot$ $\mathrm{k_B}$/sec for x, y and z axis respectively Figure 4.11.

The Doppler cooling model measures the ions' temperature $T_{\text{model}} = 1080 \pm 50$ mK. The temperature is partitioned between all motional modes according to Rabi thermometry. This temperature agrees within a 20% with the heating rate extrapolation of $T_{\text{extrap}} = 915 \pm 45$ mK using Rabi thermometry [40].

The second distribution we study is Tsallis distribution, $P(E) \propto E^2/(1 + E/n\mathrm{k_B}T)^n$, which evolves after the ion collides multiple times with ultracold atoms [20, 80, 9, 59]. In our example, the energy scale, $\mathrm{k_B} \cdot \mathrm{T}$, is determined by the intense excess micromotion, $E_{emm} = 250$ mK $\cdot$ $\mathrm{k_B}$, induced in this experiment. The power-law, $n = 4$, of the distribution is determined from a molecular-dynamics simulation [45, 46].

We use our model to extract the distribution from the experimental fluorescence curves. For the ion with a Tsallis energy distribution (red in Figure 4.10) the cooling rate is slower due to the broader energy distribution. We extract the ion's "temperature" [45], $T_{\text{ion}} = Tn/(n-2)$, from a fit to our model. The temperature, $T_{\text{model}} = 155 \pm 13$ mK agrees with the dynamics simulation results, $T_{\text{sim}} = 0.62 * E_{emm} + 7 = 162$ mK [46]. The temperature is partitioned between all motional modes equally because of atom-ion collisions. The scaling is slightly different than in the referenced article due to different trap parameters used in this experiment [45].

Comparing the multi-level model with a two-level model.

To compare the results of our model with the two-level model we fit the spectrum to a Lorentzian. We fit the 422 nm laser detuning δ_{422} such that we obtain the best fit ($\delta_{422} = -2.5$ MHz). We see that fit does not capture the recooling dynamics which would make it impossible to extract the distribution for non-coherent states Figure 4.12. Furthermore, the energy obtained from a two-level model is almost a 50% higher.

4.5 Discussion

In this chapter, we discussed a Doppler cooling thermometry of a single multi-level ion trapped in a radiofrequency Paul trap. Our analysis considers the effects of both excess and inherent micromotion. Our model gives an insight to dynamics of Doppler cooling.

This model can be used for ion thermometry in the range of 10's mK to 10's K. Below 10 mK Doppler shifts are too small to result in sufficient changes to the scattering rate. Above 10's K more and more micromotion sidebands have to be included which complicates the calculation significantly. With a good experimental signal-to-noise ratio, the model can also be used to distinguish between different energy distributions. We have also tested our model using coherent, thermal and non-thermal Tsallis energy distributions for energies between 0.5 to 3 $\mathrm{K} \cdot \mathrm{k_B}$, and obtained a good agreement with alternative measurement methods and simulations. Doppler recooling thermometry is a simple method because it requires only the set of lasers that are already used for Doppler cooling.

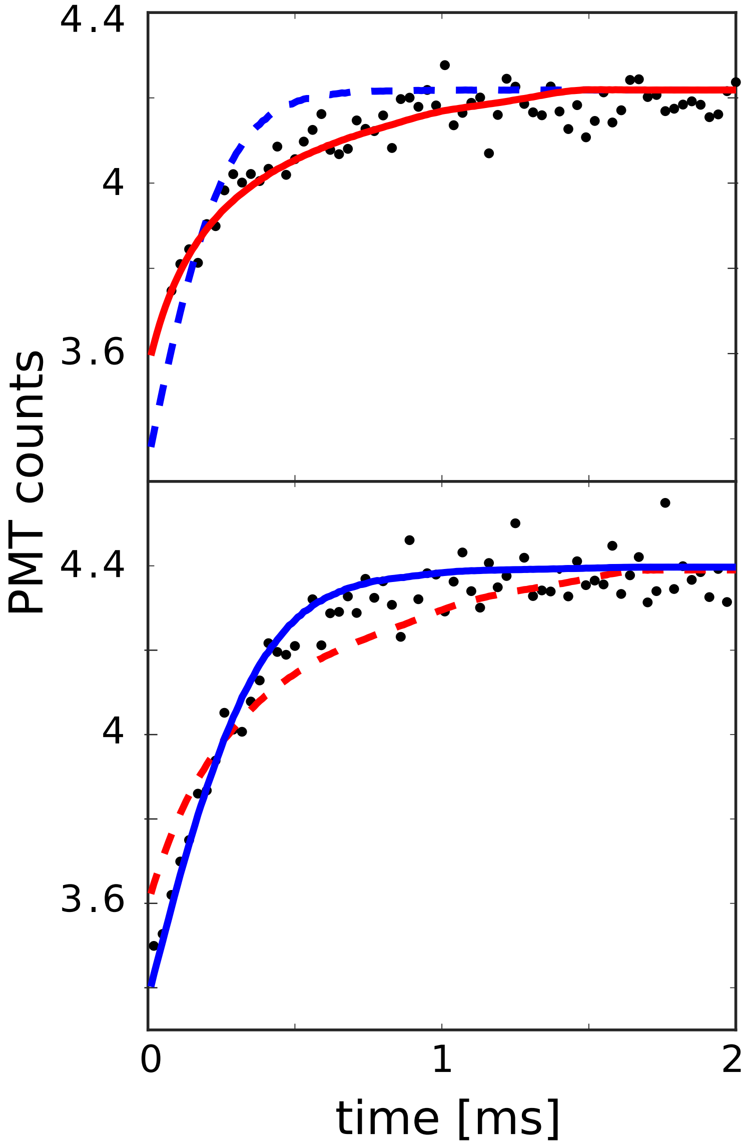

Figure 4.10: Fluorescence during Doppler cooling for different energy distributions together with a fit to a model. Data points (black) are number of photons collected at 50 μs intervals and averaged over 200 experimental realizations. Upper: Ion was prepared in a non-thermal Tsallis distribution. Lower: Ion was prepared in a thermal state. The curves are single parameter fits of the scattering rate assuming the Tsallis distribution (red) with $n = 4$ and Maxwell-Boltzmann distribution (blue). Experimental parameters for this experiment can be found in Figure 4.7. 422 nm laser detuning is $\delta_{422} = -18.57 \pm 0.059$ MHz.

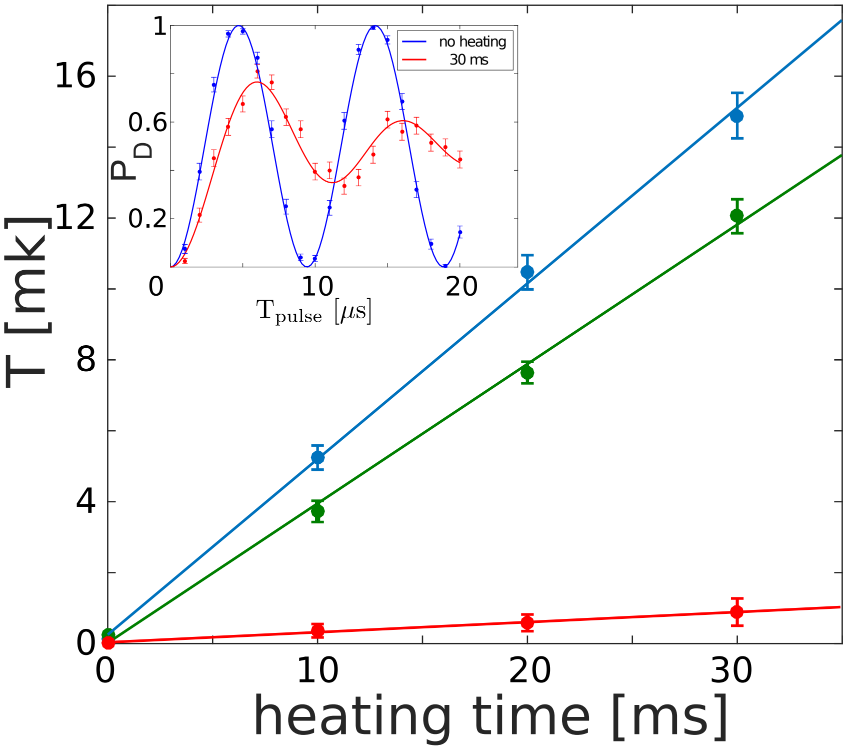

Figure 4.11: Ion temperature of each mode measured as a function of the white-noise pulse duration. The solid lines represent a linear fit for each axis: x (red), y (green) and z (blue). The inset shows examples of carrier Rabi spectroscopy for a ground-state cooled ion (blue) and for z-axis after 30ms heating pulse. We scanned the shelving pulse time and measured the shelving probability P_D. Each data point corresponds to 200 repetitions. Error bars are binomial distribution standard deviation. We fitted the data assuming a thermal distribution in a single mode since other modes are kept near the ground-state.

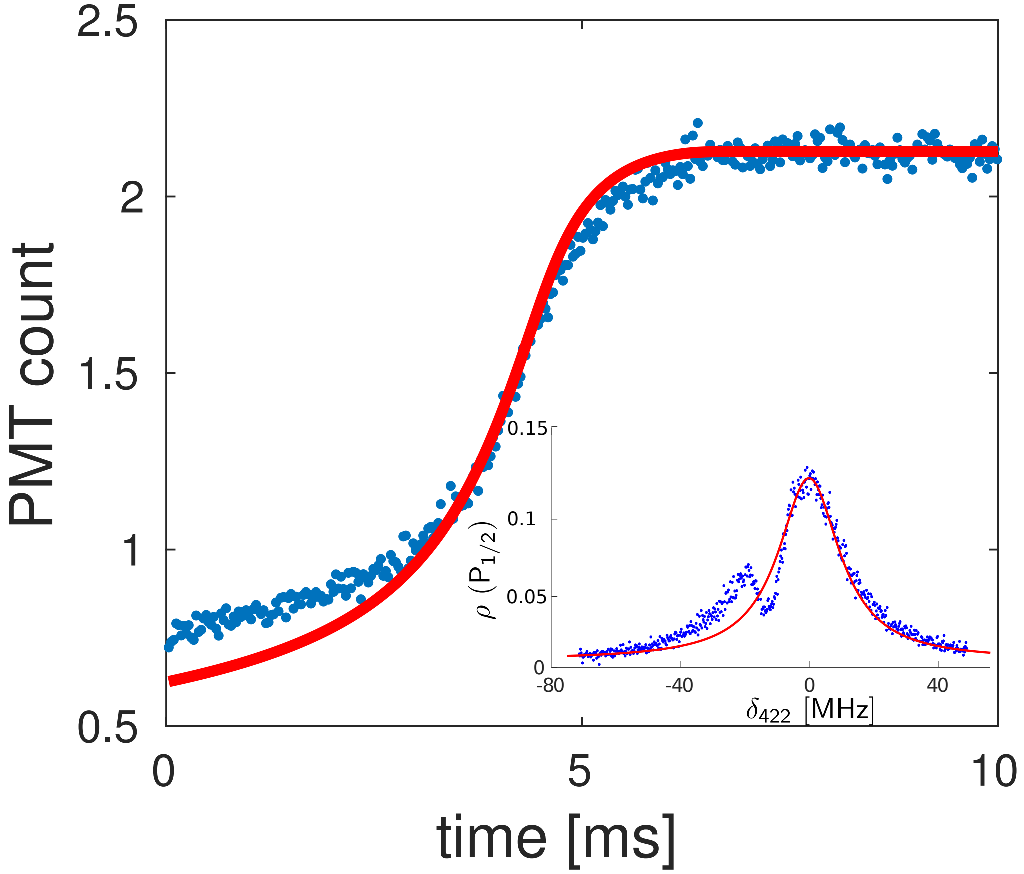

Figure 4.12: A two-level model is used to extract the energy of an ion prepared in a coherent state excited with RF pulse length of 8 ms (see Figure 4.6). We extract the ion's energy from a two parameter fit (energy and laser detuning) with a two-level model (red line). $E = 4.5 \pm 0.16\ \mathrm{K} \cdot \mathrm{k_B}$ and $\delta_{422} = -2.5$ MHz. Inset: Laser parameters are extracted from a Lorentzian fit to a spectrum of Figure 4.2.

Chapter 5

Spin dynamics[1]

The theory of spin-exchange dynamics was discussed in section 2.2. In this chapter, we are going to perform quantum scattering calculations and compare them to experimental spin-exchange results. We also performed a controlled charge-exchange experiment, in which we initialized the atoms in various spin states. This affected the overlap of the collision wave function with the singlet molecular manifold and therefore also the reaction rate.

5.1 The log derivative method

If only a few partial waves contribute to the scattering, the random-phase approximation is not valid, and a quantum mechanical calculation of the phases is necessary. To perform a quantum mechanical calculations of the acquired phase, the potential energy curves (PEC) are required. We obtained these potential curves from [4]. They were calculated using CCSD(T) [11].

Because the potential of the atom is spherically symmetric, we can write the solution in the basis set of Legendre polynomials and radial part as a combination of spherical Bessel and Neumann functions:

$$\psi\left(r,\theta\right)=\sum_{l}R_{l}\left(k,r\right)P_{l}\left(\cos(\theta)\right). \tag{5.1}$$

The asymptotic solution of the radial part of the wavefunction is:

$$R_{l}\left(k,r\right)|_{r\to\infty}=B_{l}\cdot j_{l}\left(kr\right)+C_{l}\cdot n_{l}\left(kr\right), \tag{5.2}$$

---

[1] This chapter is based on the articles [64, 65]:
Sikorsky, Tomas, et al. "Spin-controlled atomion chemistry." *Nature communications* 9.1 (2018): 920,
Sikorsky, Tomas, et al. "Phase-locking between different partial-waves in atom-ion spin-exchange collisions." *manuscript in preparation.*

where

$$\varphi = \tan^{-1}\left(-\frac{C_l}{B_l}\right). \tag{5.3}$$

By using the Ricatti-Bessel and Ricatti-Neumann functions, we can calculate the tangent phase shift,

$$\tan(\varphi) = \frac{y_N J_l - J_l'}{y_N N_l - N_l'}. \tag{5.4}$$

Here, y_n is the logarithmic derivative of the wavefunction. J and N are Ricatti-Bessel and Ricatti-Neumann functions, which are Bessel and Neumann functions multiplied by their argument. Reformulating the Schrödinger equation in terms of the log-derivative is an efficient numerical method for determining the phase shift. This is because the Schrödinger equation becomes the first-order differential equation and the value of the log-derivative at asymptote can be calculated.

To calculate the y_N we use the Johnson integration method [37]. We iterate the log-derivative value from $x = 5.0\,a_0$ to $10^4\,a_0$ in steps of h=0.002 a_0. The initial value of log derivative is estimated by the WKB approximation $y_0 \approx \sqrt{V(x_0)}$, where V is the potential energy of a given state.

We chose the $x_0 = 5.0\,a_0$ value such that the integration starts at the classically forbidden region and x_N=$10^4\,a_0$ such that the integration ends behind the l=1 centrifugal barrier $r^* = 5047\,a_0$. The integration step $h = 0.002\,a_0$ was chosen such that it is about an order of magnitude smaller than the shortest de Broglie wavelength. The maximum depth of a triplet potential is $0.029\,E_h$ which corresponds to $\lambda \approx 0.09\,a_0$. We chose the integration step size ~50 times smaller.

We calculate the phase shift for the singlet and triplet state and then use the equation 2.34 to obtain the cross-section.

5.2 Spin-exchange cross-sections and rates

We calculated the contribution to a spin-exchange cross-section from first 30 partial waves. The energy of a collision was scanned from 10 nK up to 10 mK. In Figure 5.1 we see that s-wave contributes to cross-section throughout the whole energy span and scales as $1/\sqrt{E}$. The remaining partial waves have higher contribution due to the factor (2l+1) in Equation 2.34 but their contributions drop as the collision energy falls below their centrifugal barrier. Figure 5.2 shows a thermally averaged sum of all partial waves that were used in the calculation. We see a departure from s-wave regime around 100nK. We also see that random-phase approximation begins to be a reasonable approximation for energies above 10 µK. To compare these results with experimental data a thermal averaging needs to employed. To get the spin-exchange rates, we convolve the total scattering cross-section (blue line) with a Maxwell-Boltzmann distribution (dashed purple line) (see Figure 5.2).

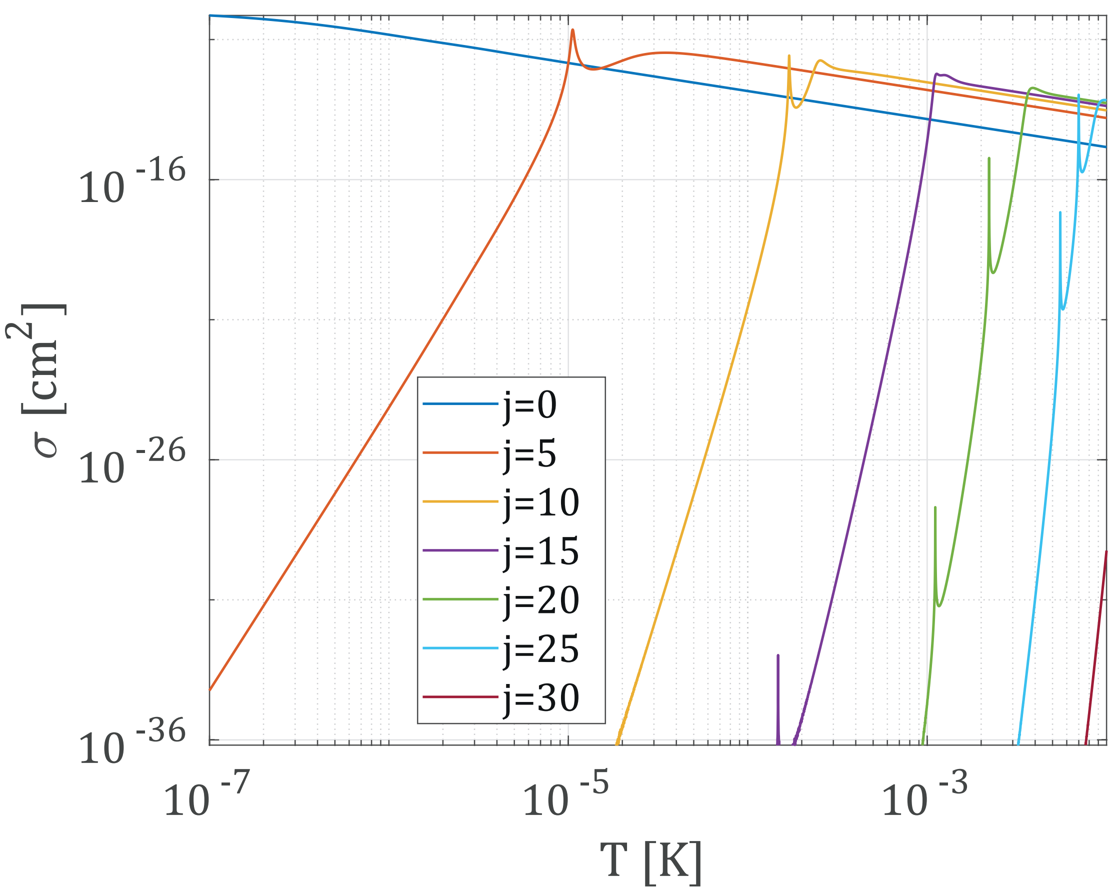

Figure 5.1: Quantum phase scattering calculations of spin-exchange cross-section for $|1,-1\rangle_{\mathrm{Rb}}\otimes|\uparrow\rangle_{\mathrm{Sr}^+} \to |1,0\rangle_{\mathrm{Rb}}\otimes|\downarrow\rangle_{\mathrm{Sr}^+}$ transition. Only contribution from selected partial waves is shown as a function of energy.

The Langevin spin-exchange rate constant for $|1,-1\rangle_{\mathrm{Rb}}\,|\uparrow\rangle_{\mathrm{Sr}^+} \to |1,0\rangle_{\mathrm{Rb}}\,|\downarrow\rangle_{\mathrm{Sr}^+}$ channel can be obtained by from Equation 2.5.

$$k_L{=}2\cdot\frac{1}{32}2\pi\sqrt{\frac{C_4}{\mu}} = 1.59\times10^{-10}\,\mathrm{cm}^3\,\mathrm{s}^{-1}. \tag{5.5}$$

The factor of $\frac{1}{32}$ comes from a projection of hyperfine states Equation 2.33 and a factor of 2 is a result of shadow scattering Equation 2.8. Equation 5.5 represents a random-phase approximation ($\sin^2(\phi_l) = 1/2$) to the spin-exchange rate constant in the presence of hyperfine interaction. The quantum rate constant can be obtained

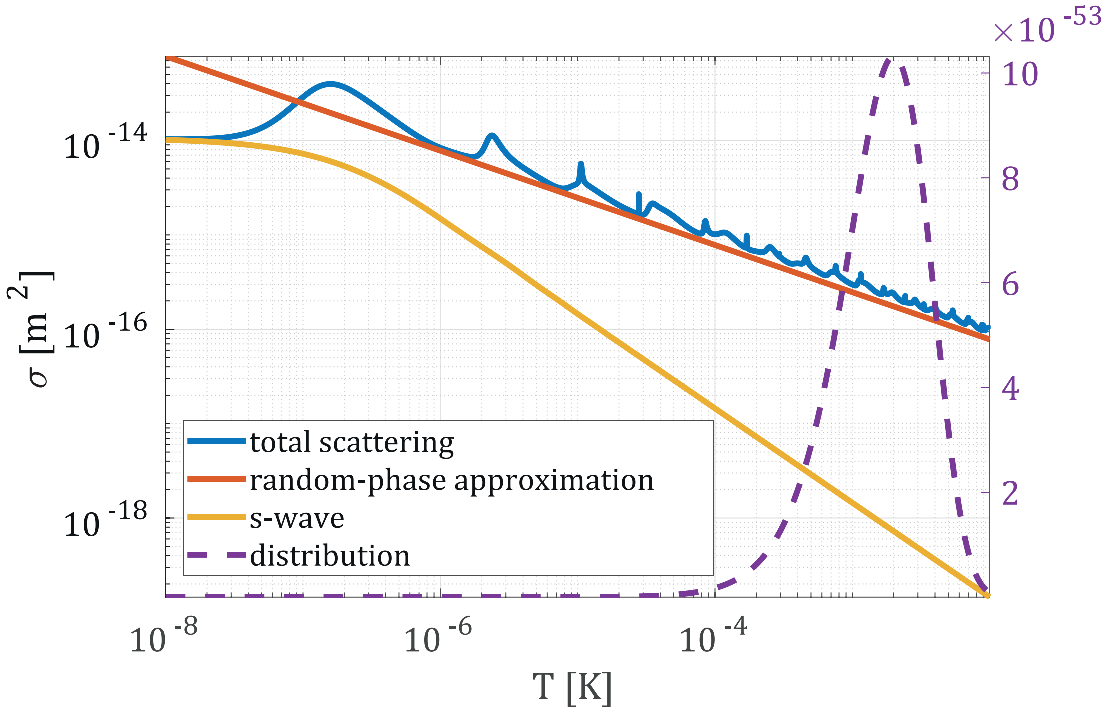

Figure 5.2: The blue line shows the sum of all 30 partial waves contribution to spin-exchange rate. The yellow line shows only the s-wave contribution. The random-phase approximation to cross-section is shown by the red line. The Maxwell-Boltzmann distribution that is used to evaluate the experimental rate is shown as the purple dashed line.

from cross-section by convolving it with the energy distribution:

$$k = \frac{1}{2(k_B T)^3} \int \sigma \sqrt{\frac{2E}{m}} E^2 exp\left(\frac{-E}{k_{\mathrm{B}} T}\right) dE. \tag{5.6}$$

In Figure 5.3 we see that the thermally averaged rate constant is energy independent for values above K and drops for temperatures below K.

To verify that 30 partial waves are enough for 1 mK collisions, we calculate the rate constant as a function of partial waves used in a summation. On Figure 5.4 we see that the calculation converges around 25 partial waves. We see that experimental data agree with theory within 20% and a within 30% with random-phase approximation. To estimate the error of quantum-phase calculations, we need to understand its sensitivity to potential energy curves. We calculated the thermally averaged rate constant for a 1 mK collision temperature with variously scaled

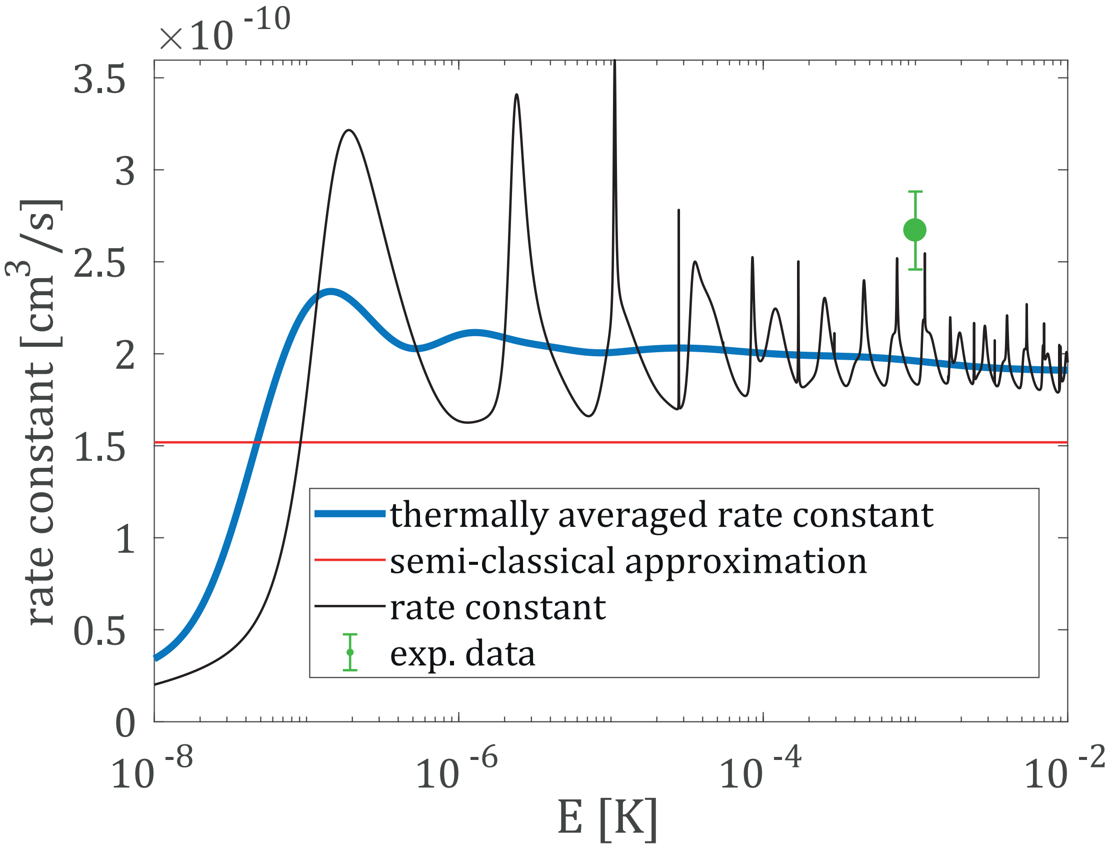

Figure 5.3: The blue line shows the spin-exchange rate constant as a function of temperature after thermal averaging with a Maxwell-Boltzmann distribution. The black line shows the rate without thermal averaging. The random-phase approximation rate constant is shown as a red line. The experimental data point is shown with 68% c.i. errorbar obtained from the statistical analysis of experimental data.

triplet potential. To maintain the physical behavior of PEC only the short-range part of the potential $V_{SR}(r)$ was scaled.

$$V(r) = V_{SR}(r) - \tfrac{C_4}{2r^4} \tag{5.7}$$

We see that as we scale the triplet potential, the rate constant oscillates around random-phase approximation value. The maximum value corresponds to twice the random-phase approximation value which is expected because of the absence of

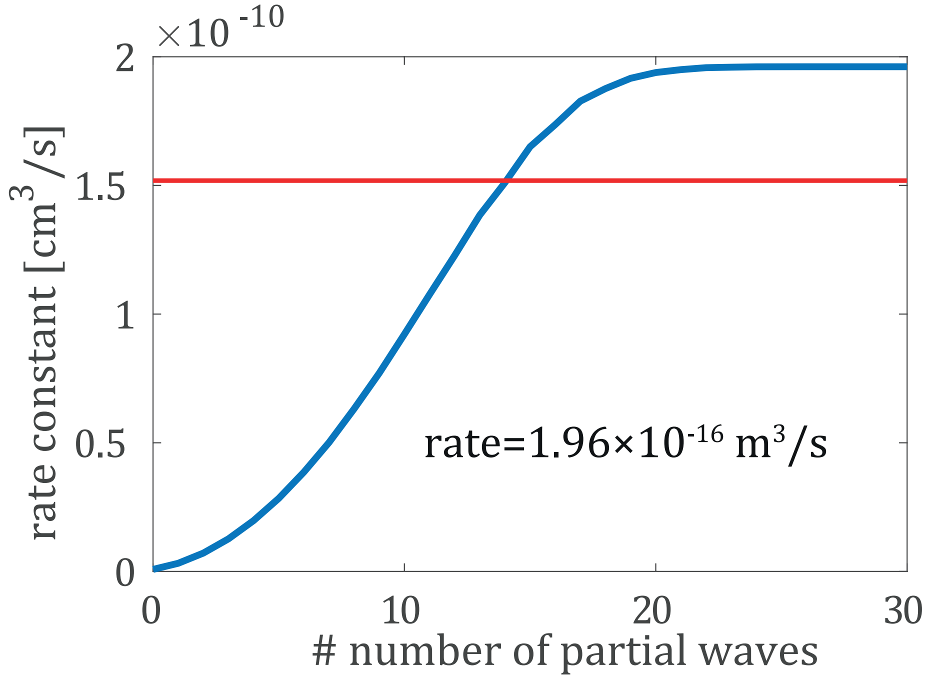

Figure 5.4: The spin-exchange rate constant as a function of partial waves included in a calculation. The red line shows a random-phase approximation.

shape resonances. We also see that scaling the potential by 10% changes the rate constant from minimum to maximum. This means that to trust these calculations we need to have potential curves with sub 1% accuracy. The high sensitivity of the spin-exchange rate on the potential curves is because phase differences for individual partial waves are highly correlated and do not randomize. This means that random-phase approximation is a bad approximation in our system.

5.3 Phase-locking between different partial waves

In the previous section, we saw that spin-exchange cross section is highly sensitive to this scaling. The inset of Figure 5.5 shows the cross-section periodically oscillating with full contrast which suggests coherent partial-wave phase-locking.

We, therefore, calculate the sine squared of individual phase shifts $\phi_l^{s/t}$ of singlet and triplet collisions and their difference ($\Delta\phi_l = \phi_l^t - \phi_l^s$). We observe that even though the $\sin^2(\phi_l^{s/t})$ for individual phase shifts change rapidly with l, their

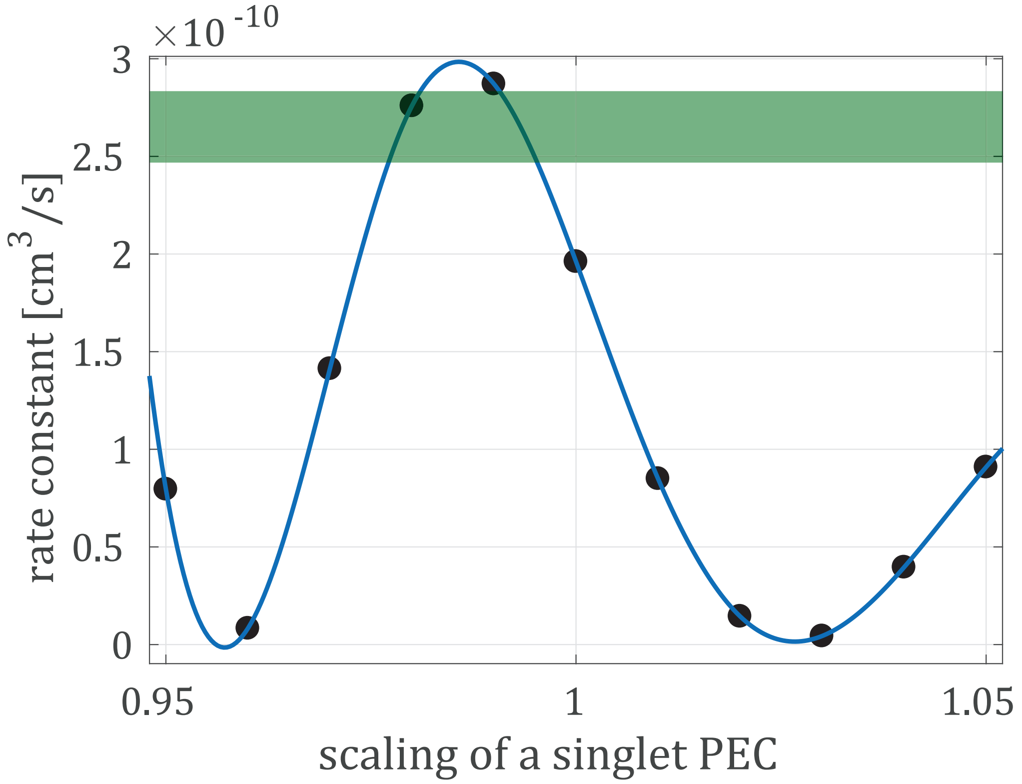

Figure 5.5: Thermally averaged rate constant at 1 mK Maxwell-Boltzmann distribution. The short-range part of the triplet PEC is scaled. The long-range part is unchanged. The green shaded area shows the experimental result.

difference $\sin^2(\Delta\phi_l)$ remains constant and drops to zero after the height of the centrifugal barrier exceeds the collision energy $l > \frac{1}{\hbar}(8\mu^2 C_4 E)^{1/4}$. This partial wave phase-locking is responsible for the oscillations in the spin-exchange cross-section when scaling the singlet PEC in Figure 5.6.

To elucidate the origin of partial-wave phase-locking, we evaluate the phase of the scattering wavefunction using the WKB approximation [39]

$$\begin{aligned}\eta_l^{s/t} = &\int_{R_0}^{\infty} \sqrt{k^2 - \frac{(l+1/2)^2}{R^2} - U_{s,t}(R)}\,\mathrm{d}R - \ldots \\ &\int_{R_0'}^{\infty} \sqrt{k^2 - \frac{(l+1/2)^2}{R^2}}\,\mathrm{d}R,\end{aligned} \tag{5.8}$$

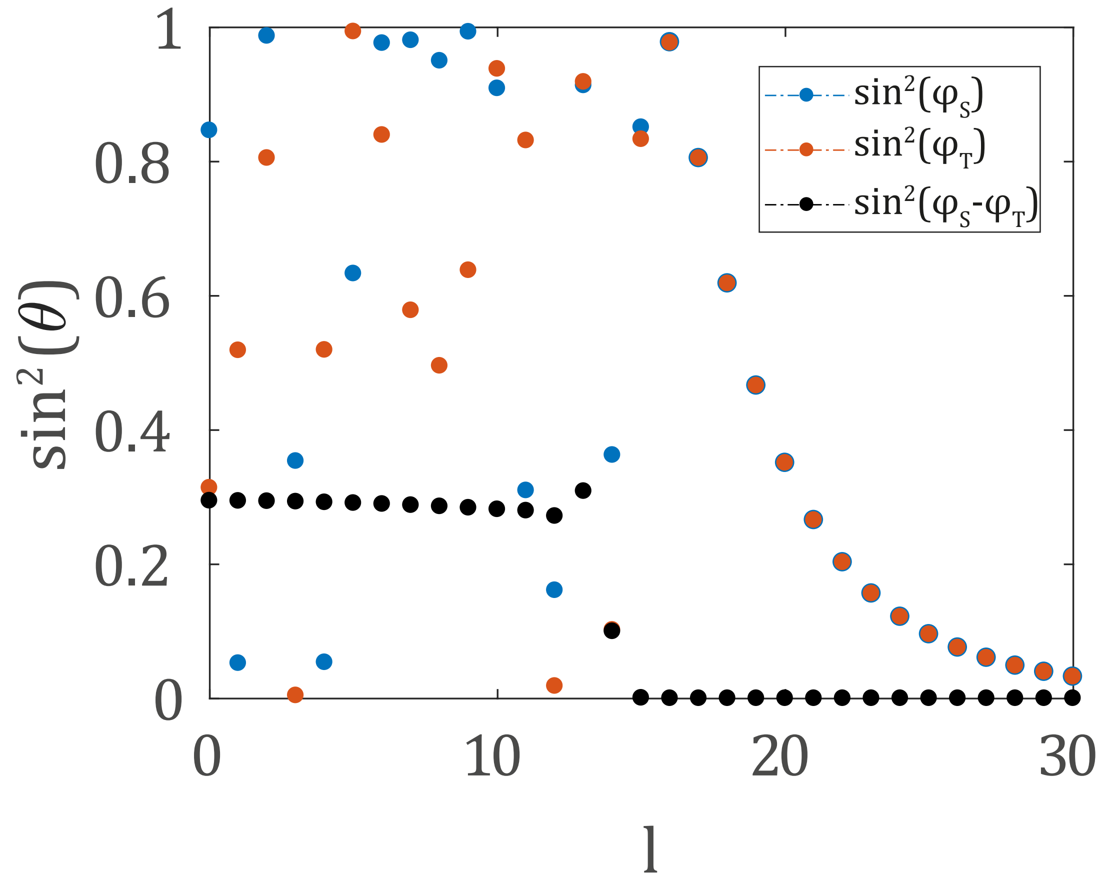

Figure 5.6: The square of sine for the difference of the scattering phase shifts, $\sin^2(\Delta\phi_l)$, as a function of l obtained using the quantum phase calculations at $E = 1\,\text{mK}$ by the black-filled circles. The squares of sine for the individual scattering phase shifts on the singlet and triplet potential energy curves, $\sin^2(\phi_l^s)$ and $\sin^2(\phi_l^t)$, are shown by the blue and red filled-circles, respectively.

where $k^2 = 2\mu E$, $U_{s,t}(R) = 2\mu V_{s,t}(R)$, R_0 and R_0' are the classical turning points in the presence and in the absence of the potential, and $\Delta\eta_l$ is given by $\Delta\eta_l = \eta_l^s - \eta_l^t$. Separating the integration range in Equation 5.8 into the short-range and long-range parts, we define the short-range phase $\eta_l^{s/t,SR} = \int_{R_0}^{R_\text{mid}} \sqrt{\dots}\,\mathrm{d}R - \int_{R_0'}^{R_\text{mid}} \sqrt{\dots}\,\mathrm{d}R$ and the long-range phase $\eta_l^{s/t,LR} = \int_{R_\text{mid}}^{\infty} \sqrt{\dots}\,\mathrm{d}R - \int_{R_\text{mid}}^{\infty} \sqrt{\dots}\,\mathrm{d}R$, with $R_\text{mid} = 30\,a_0$. Since $V_s(R) \simeq V_t(R)$ at long-range, $\eta_l^{s,LR} \simeq \eta_l^{t,LR}$ as illustrated in Figure 5.7. Thus, $\Delta\eta_l$ is determined entirely by the difference of the short-range phases as $\Delta\eta_l \simeq \eta_l^{s,SR} - \eta_l^{t,SR}$. In Figure 5.7, we observe that the individual short-range phases, as well as their difference, depend on l only very weakly due to the small

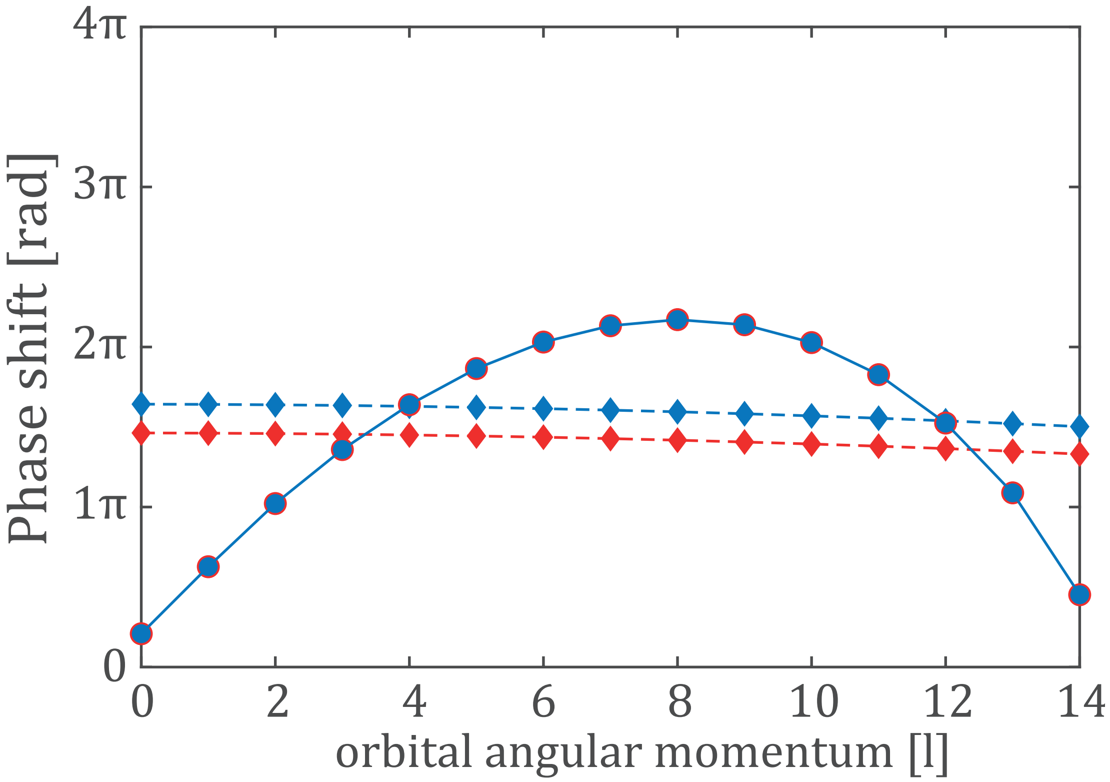

Figure 5.7: Short- (diamonds) and long- (circles) range phase shifts as a function of l for the scattering wave functions on the singlet (red) and triplet (blue) potential energy curves at $E = 1\,\mathrm{mK}$ with $R_{\mathrm{mid}} = 30\,a_0$. Modulus is 2π for short range and 4π for long range.

magnitude of the centrifugal potential compared with the potential well depth at short range. The physical origin of phase locking can thus be attributed to the short-range nature of the SE interaction and to the large potential well-depth which renders short-range physics independent of l. In other words, centrifugal forces play an important role only at atom-ion separations at which spin-exchange interaction is negligible. A sensitivity to the singlet-triplet gap could lead to a significant difference in the SE rate between different isotopes. The inset of Figure 5.7 shows a comparison between the calculated SE cross-sections of $^{86}\mathrm{Sr}^{+}$ and $^{88}\mathrm{Sr}^{+}$ colliding with $^{87}\mathrm{Rb}$ atoms indeed predicting a three-fold ratio between the cross-sections over a wide range of energies.

5.4 Spin-exchange dynamics

In ultracold collisions with the collision energy below mK, spin-exchange of Rb atoms prepared in the $|1,-1\rangle_{Rb}$ state is possible only with Sr$^+$ initialized in a $|\uparrow\rangle_{Sr^+}$ state (Equation 5.9 and Equation 5.10). A spin-exchange with $|\downarrow\rangle_{Sr^+}$ would leave the atom in a m$_F$=-2 spin projection, which is possible only for collision energies above the hyperfine barrier (328 mK) (Figure 5.8). Hence collisional pumping is possible even for atoms in non-stretched states in the F=1 ground state manifold. For stretched states of the F=2 manifold, collisional pumping can also be performed at higher energies because hyperfine barrier is not required for spin-pumping.

$$\begin{aligned}|1,-1\rangle_{\mathrm{Rb}}\otimes|\downarrow\rangle_{\mathrm{Sr^+}} &= \underbrace{\frac{\sqrt{3}}{2}\left|\tfrac{3}{2},-\tfrac{3}{2}\right\rangle_{\mathrm{nucl}}\otimes\overbrace{|\uparrow\rangle_{\mathrm{elec}}\otimes|\downarrow\rangle_{\mathrm{Sr^+}}}^{\text{anti}-\text{parallel spins}}}_{\text{spin exchange energetically suppresed}}-\frac{1}{2}\left|\tfrac{3}{2},-\tfrac{1}{2}\right\rangle_{\mathrm{nucl}}\otimes\overbrace{|\downarrow\rangle_{\mathrm{elec}}\otimes|\downarrow\rangle_{\mathrm{Sr^+}}}^{\text{parallel spins}}\\ &\overset{\text{spin exch.}}{\Longrightarrow}\frac{\sqrt{3}}{2}\underbrace{\left|\tfrac{3}{2},-\tfrac{3}{2}\right\rangle_{\mathrm{nucl}}\otimes|\downarrow\rangle_{\mathrm{elec}}}_{\cancel{|\mathrm{F{=}2,m_F{=}-2}\rangle_{\mathrm{Rb}}}}\otimes|\uparrow\rangle_{\mathrm{Sr^+}}-\frac{1}{2}\left|\tfrac{3}{2},-\tfrac{1}{2}\right\rangle_{\mathrm{nucl}}\otimes|\downarrow\rangle_{\mathrm{elec}}\otimes|\downarrow\rangle_{\mathrm{Sr^+}}\end{aligned}\tag{5.9}$$

$$\begin{aligned}|1,-1\rangle_{\mathrm{Rb}}\otimes|\uparrow\rangle_{\mathrm{Sr^+}} &= \frac{\sqrt{3}}{2}\left|\tfrac{3}{2},-\tfrac{3}{2}\right\rangle_{\mathrm{nucl}}\otimes\overbrace{|\uparrow\rangle_{\mathrm{elec}}\otimes|\uparrow\rangle_{\mathrm{Sr^+}}}^{\text{parallel spins}}\underbrace{-\frac{1}{2}\left|\tfrac{3}{2},-\tfrac{1}{2}\right\rangle_{\mathrm{nucl}}\otimes\overbrace{|\downarrow\rangle_{\mathrm{elec}}\otimes|\uparrow\rangle_{\mathrm{Sr^+}}}^{\text{anti}-\text{parallel spins}}}_{\text{spin exchange allowed}}\\ &\overset{\text{spin exch.}}{\Longrightarrow}\frac{\sqrt{3}}{2}\left|\tfrac{3}{2},-\tfrac{3}{2}\right\rangle_{\mathrm{nucl}}\otimes|\uparrow\rangle_{\mathrm{elec}}\otimes|\uparrow\rangle_{\mathrm{Sr^+}}-\frac{1}{2}\underbrace{\left|\tfrac{3}{2},-\tfrac{1}{2}\right\rangle_{\mathrm{nucl}}\otimes|\uparrow\rangle_{\mathrm{elec}}}_{\frac{1}{\sqrt{2}}|1,0\rangle_{\mathrm{Rb}}+\cancel{\frac{1}{\sqrt{2}}|\mathrm{F}=2,\mathrm{m_F}=0\rangle_{\mathrm{Rb}}}}\otimes|\downarrow\rangle_{\mathrm{Sr^+}}\end{aligned}\tag{5.10}$$

In the experiment, a single spin-polarized ion is trapped in a linear Paul trap, ground state cooled to $\sim$ 40 µK and then immersed in an ultra-cold ($\sim \mu K$), hyperfine spin-polarized Rb cloud. Due to non-equilibrium dynamics of atom-ion elastic collisions, the ion heats to mK temperature after few collisions [45]. We collisionally pump the spin of the Sr$^+$ ion to the $|\downarrow\rangle_{Sr^+}$ state with $\sim$ 90% fidelity (see Figure 5.8). Pumping is performed via spin-exchange between polarized atoms in the $|1,-1\rangle_{Rb}$ state and the ion[14]. Since the atoms are trapped in a shallow optical potential ($\sim \mu K$) and because the ion's temperature is ($\sim mK$), the spin-exchanged atoms leave the trap while the rest of the Rb cloud remains fully polarized. For comparison, we perform the same experiment with the atoms polarized to the $|1,0\rangle_{Rb}$ state Figure 5.8. Here, since spin-exchange is allowed for both Sr$^+$ spin states and the ion evolves to a fully mixed spin state.

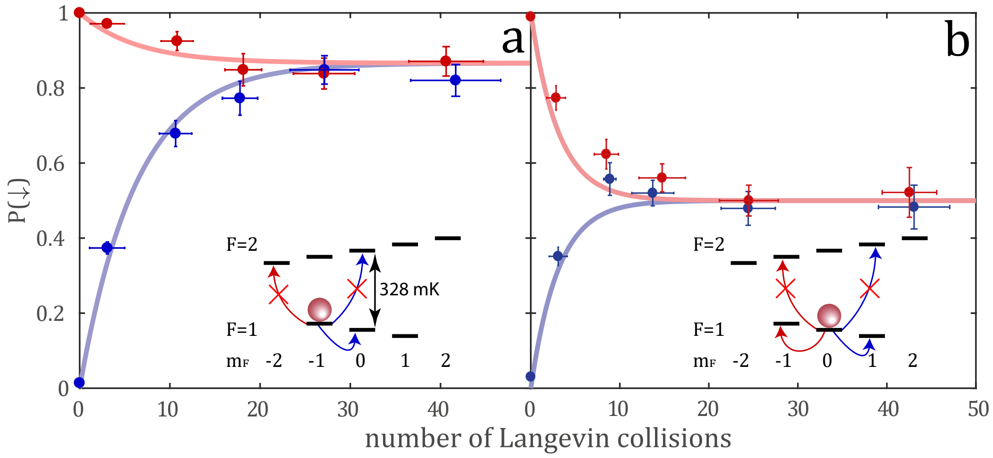

Figure 5.8: Sr^+ ion spin projection on the $|{\downarrow}\rangle_{\mathrm{Sr}^+}$ state, P(↓), as function of number of Langevin collisions (time). In blue (red) the ion is prepared in the $|{\uparrow}\rangle_{\mathrm{Sr}^+}$ ($|{\downarrow}\rangle_{\mathrm{Sr}^+}$) spin-state. The atoms are prepared in state $|1,-1\rangle_{\mathrm{Rb}}$ (a) or $|1,0\rangle_{\mathrm{Rb}}$ (b). Insets show energetically allowed and forbidden spin-exchange processes. Error bars represent one standard deviation.

For our choice of atom-ion mixture, spin-relaxation limits the fidelity of collisional pumping to ∼ 90%. Unlike previous experiments with Yb^+-Rb mixtures [56, 55], where spin-relaxation was dominating over the spin-exchange, and collisional pumping was almost not observed. Furst et al. [23] was able to achieve a similar spin-pumping fidelity with with Yb^+/Li (∼ 93%) than our system with Sr^+/Rb. The spin relaxation for $^{174}Yb^+$ Zeeman qubit occurs after 6.4(1.1) Langevin collisions on average when colliding with Rb atoms. In spite of this fast relaxation, spin-pumping was possible due to very fast spin-exchange rate.

Tscherbul et al. [68] identified a 2nd order spin-orbit coupling to be the main cause of spin-relaxation. They predicted that using lighter species should reduce the 2nd order spin-orbit coupling.

For Sr^+-Rb atom-ion mixture, spin-relaxation limits the fidelity of collisional pumping to ∼ 90%. From a fit to rate equations (Equation 5.11 and Equation 5.12) we found that the spin-exchange rate in our system is $\frac{k_L}{k_{SE}} = 9.1 \pm 0.59$ and spin-relaxation rate is $\frac{k_L}{k_{SR}} = 47.5 \pm 6.6$ where k_L is the Langevin collision rate.

The spin-exchange and spin-relaxation dynamics of the Sr^+ ion in the atomic bath is governed by two-level rate equations:

$$\begin{aligned} \dot{p_\downarrow} &= \gamma_{SE} \cdot p_\uparrow + \gamma_{SR} \cdot (p_\uparrow - p_\downarrow), \\ \dot{p_\uparrow} &= -\gamma_{SE} \cdot p_\uparrow + \gamma_{SR} \cdot (p_\downarrow - p_\uparrow), \end{aligned} \tag{5.11}$$

$$\begin{aligned} \dot{p_\uparrow} &= (\gamma_{SE} + \gamma_{SR}) \cdot (p_\downarrow - p_\uparrow), \\ \dot{p_\downarrow} &= (\gamma_{SE} + \gamma_{SR}) \cdot (p_\uparrow - p_\downarrow). \end{aligned} \tag{5.12}$$

Here, Equation 5.11 is for atoms in $|1,-1\rangle_{\mathrm{Rb}}$ state and Equation 5.12 is for atoms in $|1,0\rangle_{\mathrm{Rb}}$ state. γ_{SE} (γ_{SR}) are spin-exchange (spin-relaxation) constants and $p_\uparrow + p_\downarrow = 1$. The collisional rate constant is defined as $k = 1 - e^{-\gamma}$.

The fact that the spin-relaxation rate is $\sim$ 5 times slower than the spin-exchange rate allows us not only to control the spin state of the ion using atoms but also to maintain the spin state during multiple collisions.

To explore the dynamics further, we prepared Rb atoms in the $|1,0\rangle$ state with ions in either $|\uparrow\rangle$ or $|\downarrow\rangle$. Here, SE can work both ways: $|1,0\rangle_{\mathrm{Rb}} \otimes |\uparrow\rangle_{\mathrm{Sr}^+} \rightarrow |1,1\rangle_{\mathrm{Rb}} \otimes |\downarrow\rangle_{\mathrm{Sr}^+}$ and $|1,0\rangle_{\mathrm{Rb}} \otimes |\downarrow\rangle_{\mathrm{Sr}^+} \rightarrow |1,-1\rangle_{\mathrm{Rb}} \otimes |\uparrow\rangle_{\mathrm{Sr}^+}$. The evolution of the ions spin for both initial states is shown Figure 5.8. Because for atoms prepared in $|1,0\rangle_{\mathrm{Rb}}$ state the SE and SR are experimentally indistinguishable, we assumed same SR rates as for $|1,-1\rangle_{\mathrm{Rb}}$.

5.5 Effect of magnetic field on spin-exchange

We measured spin population dynamics at a higher magnetic field to investigate a possible dependence of the spin-exchange rate. At magnetic field of 9.61 Gauss, there are no significant differences for $|1,-1\rangle_{\mathrm{Rb}} \otimes |\uparrow\rangle_{\mathrm{Sr}^+} \rightarrow |1,0\rangle_{\mathrm{Rb}} \otimes |\downarrow\rangle_{\mathrm{Sr}^+}$ rate. However at 9.61 Gauss we found the rate constants for experiments with $|1,0\rangle_{Rb}$ atoms to differ from 3.02 Gauss. The endoenergetic transition $|1,0\rangle_{\mathrm{Rb}} \otimes |\downarrow\rangle_{\mathrm{Sr}^+} \rightarrow |1,-1\rangle_{\mathrm{Rb}} \otimes |\uparrow\rangle_{\mathrm{Sr}^+}$ spin-exchange rate is suppressed due to energetic barrier of $\sim$ 1.5 mK (see Figure 5.8 and Figure 5.9). Because quantum phase calculations assume degenerate initial and finals states, to study the effect of magnetic field we performed a coupled-channel (CC) calculations [65]. To match the experimental data with a theory we tuned the singlet PEC such that the experimental spin-exchange rate of $|1,-1\rangle_{\mathrm{Rb}} \otimes |\uparrow\rangle_{\mathrm{Sr}^+} \rightarrow |1,0\rangle_{\mathrm{Rb}} \otimes |\downarrow\rangle_{\mathrm{Sr}^+}$ transition matches the CC calculation. We see that while all rates match the theory the endoenergetic SE transition $|1,0\rangle_{\mathrm{Rb}} \otimes |\uparrow\rangle_{\mathrm{Sr}^+} \rightarrow |1,1\rangle_{\mathrm{Rb}} \otimes |\downarrow\rangle_{\mathrm{Sr}^+}$ at 9.61 Gauss is affected by Zeeman barrier. This effect is simply due to energy conservation. On Figure 5.10 we see the energy dependence of a spin-exchange cross-section for endo- and exo- energetic spin transitions. Also in left inset of Figure 5.9 we see that for 9.61 Gauss magnetic field the steady state $|\downarrow\rangle$ spin population is higher than in Figure 5.8. Up to now, SR rates were extracted from the steady-state spin population using rate equations (Equation 5.11 and Equation 5.12). Here, we use ion thermometry [63], to extract the SR rate of the system prepared in the $|2,-2\rangle_{\mathrm{Rb}} \otimes |\downarrow\rangle_{\mathrm{Sr}^+}$ state. We use the fact that most of the spin-relaxation channels from $|2,-2\rangle_{\mathrm{Rb}} \otimes |\downarrow\rangle_{\mathrm{Sr}^+}$ lead to Rb atoms

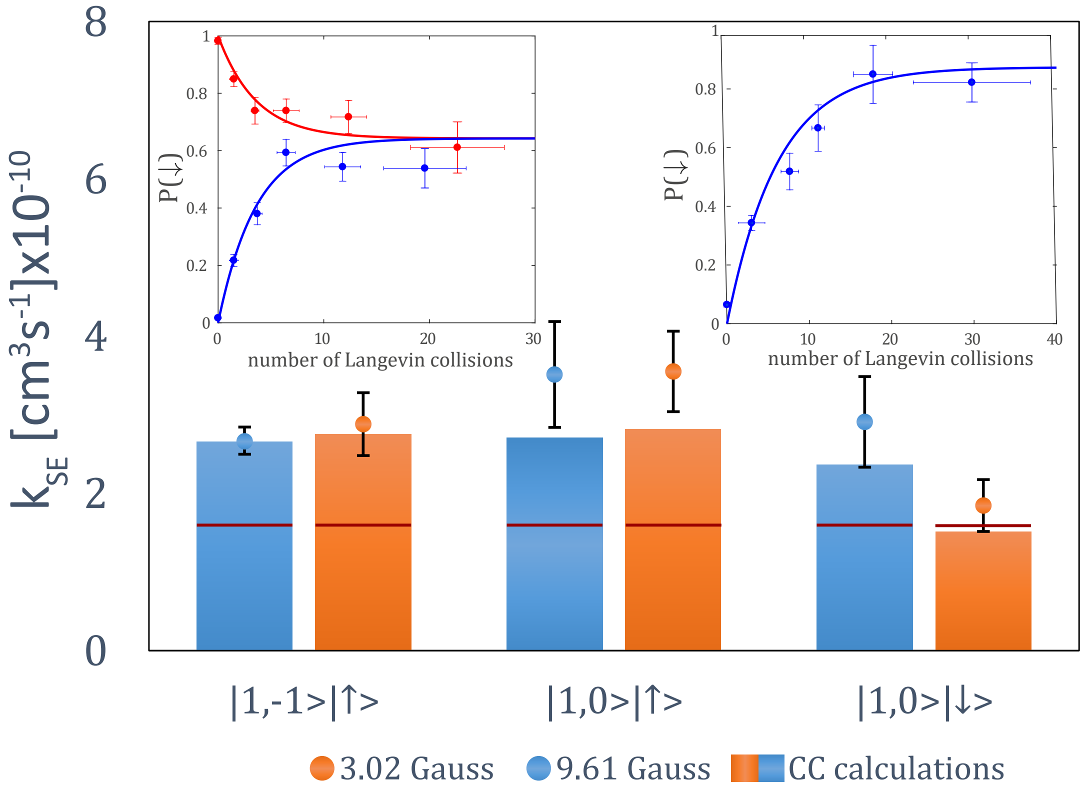

Figure 5.9: Experimental spin-exchange rate constants (k_{SE}) for various initial states and magnetic fields. Bars represent the rate constants obtained from CC calculated cross-sections convolved with a Tsallis energy distribution. Red line shows the random-phase approximation results. Insets show an example of the raw experimental data that were used to extract the rate constant. The left inset shows the evolution of the ion spin state prepared in either $|\uparrow\rangle_{\mathrm{Sr}^+}$ or $|\downarrow\rangle_{\mathrm{Sr}^+}$ state colliding with atoms in $|1,0\rangle_{\mathrm{Rb}}$ state. Right inset shows ion initialized in the $|\uparrow\rangle$ state colliding with atoms in $|1,-1\rangle_{\mathrm{Rb}}$. Both insets are for $B = 9.61$ Gauss.

in the $F = 1$ manifold which release 328 mK of energy. This leads to heating of the ion which we detect using Doppler cooling thermometry. From the fluorescence re-cooling curve (Figure 5.11) we can extract the probability that hyperfine energy is released during a collision p_{HF}.

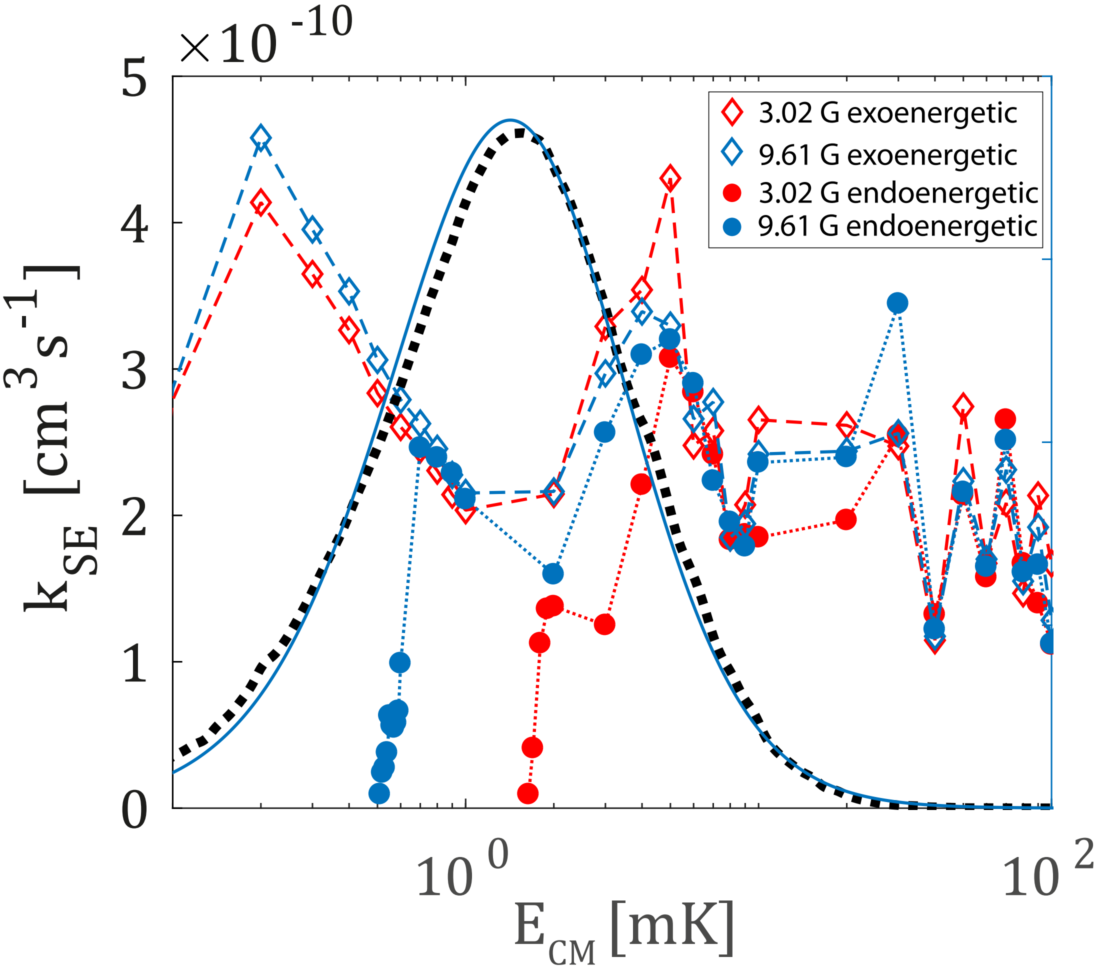

Figure 5.10: Energy distribution in the laboratory frame extracted from the simulation (black dashed line). Tsallis fit $n = 4.04$ $T = 0.43\,\mathrm{mK}$ (blue line). Endoenergetic $|1,0\rangle_{\mathrm{Rb}} \otimes |\uparrow\rangle_{\mathrm{Sr}^+} \rightarrow |1,1\rangle_{\mathrm{Rb}} \otimes |\downarrow\rangle_{\mathrm{Sr}^+}$ (diamonds) and exoenergetic $|1,0\rangle_{\mathrm{Rb}} \otimes |\downarrow\rangle_{\mathrm{Sr}^+} \rightarrow |1,-1\rangle_{\mathrm{Rb}} \otimes |\uparrow\rangle_{\mathrm{Sr}^+}$ (circles) SE cross-section for B=3.02 Gauss (blue) and B=9.61 Gauss (red).

5.6 Spin-relaxation dynamics

The hyperfine heating occurs directly when Rb atom spin-relaxes into the F=1 state during a collision, or indirectly when Sr^+ ion spin-relaxes into $|\uparrow\rangle$ state and following collisions spin-exchange the Rb atom to F=1 manifold Equation 5.13. In the experiment every collision occurs with different Rb atom, thus for the atoms prepared in $|2,-2\rangle_{\mathrm{Rb}}$ state the probability to relase hyperfine energy through SE after Sr$^+$ ion spin-relaxes into $|\uparrow\rangle$ state is $p_{HF} = 75\%$ subsection 2.4.3.

$$\begin{tikzcd}
|F=2\rangle_{\mathrm{Rb}} \otimes |\downarrow\rangle_{\mathrm{Sr}^+} \arrow[r, "\mathrm{SR}"] \arrow[dd, "\mathrm{SR}"] & |F=1\rangle_{\mathrm{Rb}} \otimes |\mathrm{all}\rangle_{\mathrm{Sr}^+} \\
 & |F=1\rangle_{\mathrm{Rb}} \otimes |\downarrow\rangle_{\mathrm{Sr}^+} \\
|\mathrm{all}\rangle_{\mathrm{Rb}} \otimes |\uparrow\rangle_{\mathrm{Sr}^+} \arrow[ur, "\mathrm{SE}"] \arrow[dr, "\mathrm{SE}"] & \\
 & |F=2\rangle_{\mathrm{Rb}} \otimes |\downarrow\rangle_{\mathrm{Sr}^+}
\end{tikzcd} \tag{5.13}$$

Hyperfine heating competes with sympathetic cooling [43] which leads to a non-equilibrium dynamics of ion energy and non-analytic energy distribution. We implemented hyperfine heating into molecular dynamics simulation [45] to extract this distribution subsection 2.4.3. The steady-state energy distribution depends on p_{HF}. We extract the energy distribution using Doppler cooling thermometry [63]. On Figure 5.11 we see Doppler cooling fluorescence curves after an interaction time of 500 ms, during which 100's of Langevin collisions occurred. We extracted from these fluorescence curves the p_{HF} probabilities.

Because $|2,-2\rangle_{\mathrm{Rb}}$ is a stretched state of the $F = 2$ hyperfine level, the p_{HF} probability can be linked to SR: $|2,-2\rangle_{\mathrm{Rb}} \otimes |\downarrow\rangle_{\mathrm{Sr}^+} \xrightarrow{\mathrm{SR}} |F=1\rangle_{\mathrm{Rb}} \otimes |\mathrm{all}\rangle_{\mathrm{Sr}^+}$ and $|2,-2\rangle_{\mathrm{Rb}} \otimes |\downarrow\rangle_{\mathrm{Sr}^+} \xrightarrow{\mathrm{SR}} |\mathrm{all}\rangle_{\mathrm{Rb}} \otimes |\uparrow\rangle_{\mathrm{Sr}^+} \xrightarrow{\mathrm{SE}} |F=1\rangle_{\mathrm{Rb}} \otimes |\downarrow\rangle_{\mathrm{Sr}^+}$.

Similarly, as in the previous section, we compare our results with theoretical calculations. Unfortunatelly same as for spin-exchange calculations here also the ab-initio data are not accurate enough to reproduce experimental results. For the calculation of spin relaxation, the spin-orbit coupling $\lambda_{\mathrm{SO}}(R)$ is scaled by multiplying by a constant of 0.45 to reproduce the experimental rate constant for the $|1,-1\rangle_{\mathrm{Rb}} \otimes |\downarrow\rangle_{\mathrm{Sr}^+} \to |1,0\rangle_{\mathrm{Rb}} \otimes |\uparrow\rangle_{\mathrm{Sr}^+}$ process at $B = 3.02$ Gauss.

We then repeated the CC spin-relaxation calculation for $|2,-2\rangle_{\mathrm{Rb}} \otimes |\downarrow\rangle_{\mathrm{Sr}^+} \xrightarrow{\mathrm{SR}} |F=1\rangle_{\mathrm{Rb}} \otimes |\mathrm{all}\rangle_{\mathrm{Sr}^+}$ spin-relaxation channel with scaled $\lambda_{\mathrm{SO}}(R)$. The result of the calculation agrees with the experiment Figure 5.11.

5.7 Charge exchange

Due to the Pauli exclusion principle, a radiative charge-exchange is only allowed for (RbSr)$^+$ colliding in the singlet state $^1\Sigma_0^+$. This is because after the charge-exchange transfers both valence electrons into Sr(1S) orbital. If spin-relaxation is not present, there is no mechanism to flip the spin of the electrons if they are aligned.

In a previous experiment [56], the authors reported suppressed charge exchange for a (RbYb)$^+$ mixtures, where the atoms prepared in the F=2 state compared

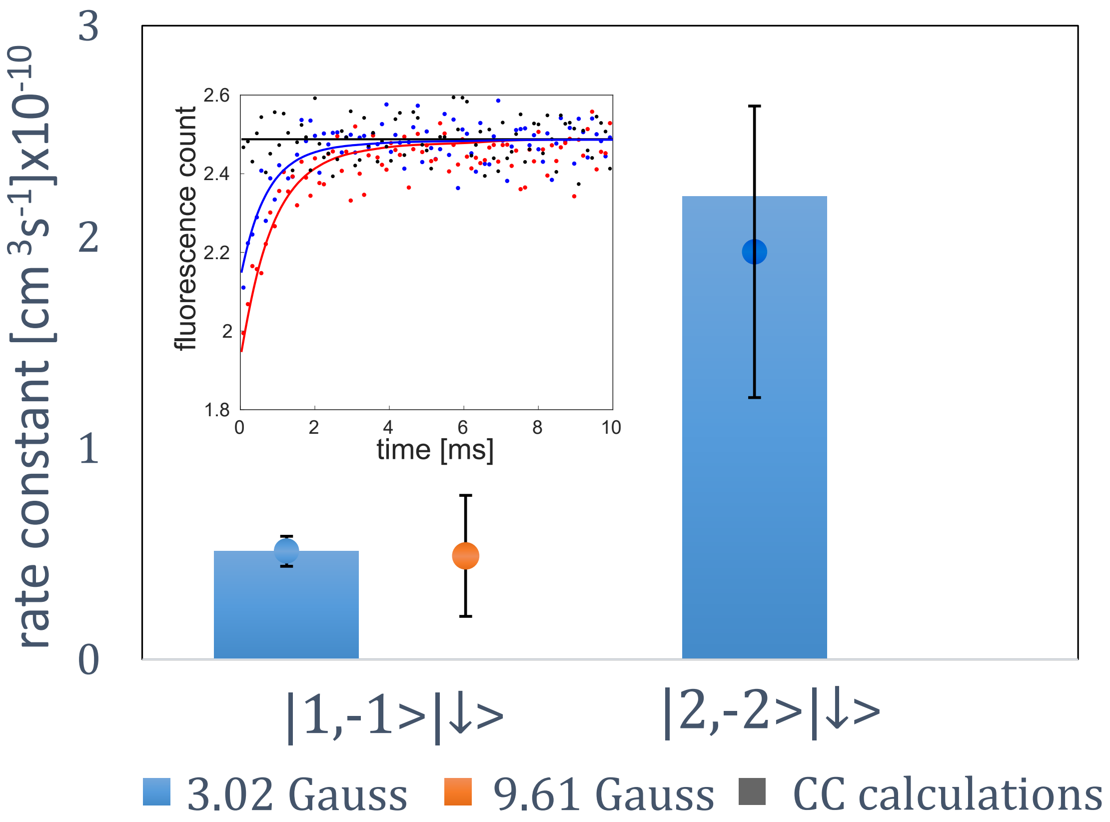

Figure 5.11: Comparison of experimental rates with theoretical calculations. $|1,-1\rangle_{\mathrm{Rb}} \otimes |{\downarrow}\rangle_{\mathrm{Sr}^+} \rightarrow |\mathrm{all}\rangle_{\mathrm{Rb}} \otimes |{\uparrow}\rangle_{\mathrm{Sr}^+}$ and direct (dark blue) $|2,-2\rangle_{\mathrm{Rb}} \otimes |{\downarrow}\rangle_{\mathrm{Sr}^+} \xrightarrow{\mathrm{SR}} |F=1\rangle_{\mathrm{Rb}} \otimes |\mathrm{all}\rangle_{\mathrm{Sr}^+}$ with indirect (light blue) $|2,-2\rangle_{\mathrm{Rb}} \otimes |{\downarrow}\rangle_{\mathrm{Sr}^+} \xrightarrow{\mathrm{SR}} |\mathrm{all}\rangle_{\mathrm{Rb}} \otimes |{\uparrow}\rangle_{\mathrm{Sr}^+} \xrightarrow{\mathrm{SE}} |F=1\rangle_{\mathrm{Rb}} \otimes |{\downarrow}\rangle_{\mathrm{Sr}^+}$ compared to CC theory calculations. Inset shows Sr^+ ion fluorescence during Doppler cooling after 500 ms interaction time with $|2,-2\rangle$ Rb atoms (blue). Red data are for atoms prepared in $|2,0\rangle$ state and black data are for $|1,-1\rangle$. We extract the SR rate constant from a single parameter fit.

to the F=1 manifold. We similarly measure suppression of charge-exchange for Rb atoms prepared in the $|2,-2\rangle_{\mathrm{Rb}}$ compared to the $|1,-1\rangle_{\mathrm{Rb}}$ state. However, we also measure a similar suppression for the $|2,0\rangle_{\mathrm{Rb}}$ state (Figure 16). This measurement suggests that suppression of charge exchange in the F=2 manifold is not only related to the spin configuration. One explanation is that in our case the charge-exchange rate is energy dependent and is suppressed due to the increased steady state temperature.

To further investigate this, we measure the charge-exchange rate also for atoms prepared in the $|1,-1\rangle_{\mathrm{Rb}}$ state, however, with ion's micromotion at the 25mK level.

We observe a similar suppression as in the F=2 manifold (see Figure 5.12). This suggests that charge-exchange suppression in the F=2 manifold is due to increased energy. Figure 17 shows a linear scaling of the charge-exchange rate with atom density, confirming that binary collisions are the main cause of the charge-exchange. To study the charge-exchange dependence on wavefunction symmetry and to circumvent the effect of temperature, we perform the charge-exchange experiments in the F=1 manifold. Initializing the atoms in various spin states affects the overlap of the collision wavefunction with the singlet manifold and should modify the reaction rate.

To obtain the projection to a singlet manifold we expand the atoms hyperfine state to the electronic spin basis (see Equation 5.14).

$$\begin{aligned} \left|\Big\langle \langle 1,-1|_{\mathrm{Rb}} \otimes \langle\downarrow|_{\mathrm{Sr}^+} \Big|\mathrm{singlet}\Big\rangle\right|^2 &= \frac{3}{4}\left|\Big\langle \langle \tfrac{3}{2},-\tfrac{3}{2}|_{\mathrm{nucl}} \otimes \langle\uparrow|_{\mathrm{elec}} \otimes \langle\downarrow|_{\mathrm{Sr}^+} \Big|\mathrm{singlet}\Big\rangle\right|^2 = 0.375 \\ \left|\Big\langle \langle 1,0|_{\mathrm{Rb}} \otimes \langle\downarrow|_{\mathrm{Sr}^+} \Big|\mathrm{singlet}\Big\rangle\right|^2 &= \frac{1}{2}\left|\Big\langle \langle \tfrac{3}{2},-\tfrac{1}{2}|_{\mathrm{nucl}} \otimes \langle\uparrow|_{\mathrm{elec}} \otimes \langle\downarrow|_{\mathrm{Sr}^+} \Big|\mathrm{singlet}\Big\rangle\right|^2 = 0.25 \end{aligned} \tag{5.14}$$

When atoms are initialized in the $|1,-1\rangle_{\mathrm{Rb}}$ state and the ion is collisionally pumped to $P(\downarrow)\sim 0.9$, the projection to a singlet manifold is $0.9\times 0.375+0.1\times 0.25 = 0.3625$. When the atoms are in a $|1,0\rangle_{\mathrm{Rb}}$ and the ion is in a fully mixed spin state this probability is 0.25. We therefore expect a ratio of 1.45 between the charge-exchange rates in the two cases.

In the experiment, we overlapped the atoms with the single ion for 1 s which is equivalent to $\sim 10^3$ Langevin collisions. This was repeated 1000 times in an interlaced manner, in which atoms are prepared alternatively in a $|1,-1\rangle$ and $|1,0\rangle$ states. During these 2000 repetitions, we recorded 104 charge-exchange events. 61 of these events were recorded when the atoms were prepared in $|1,-1\rangle_{\mathrm{Rb}}$ and 43 were with atoms in a $|1,0\rangle_{\mathrm{Rb}}$. This corresponds to a ratio of 1.42 ± 0.2 ratio between the rates as expected by the simple considerations above. The measured rates for the two states are shown in Figure 5.12.

Furthermore, to verify that in our experiment charge-exchange is a two-body process, which supports a radiative mechanism, we measured the charge-exchange rate at different densities and recovered a linear density dependence. We also performed a charge-exchange experiment at various YAG laser intensities and found no charge-exchange rate dependence on YAG laser power (see Figure 5.13).

5.8 Discussion

In this chapter, we studied the spin dynamics of a single Sr^+ ion. We have shown that if the ion is immersed in an ultracold spin-polarized Rb cloud, it reaches the

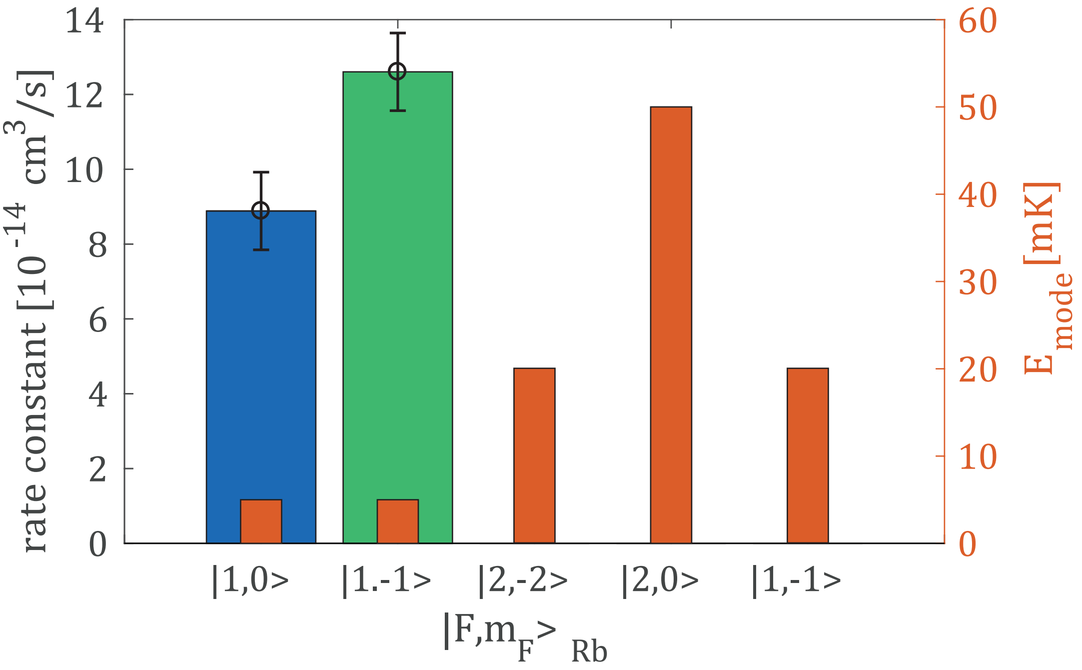

Figure 5.12: Charge-exchange rates and temperatures of an ion for various hyperfine states of the Rb atoms. Excess micromotion is compensated to a level of $\sim 0.1\,\mathrm{mK}$ for all but last column $\sim 25\,\mathrm{mK}$. F=2* and $|1,-1\rangle^*_{\mathrm{Rb}}$ null results are not shown on the chart. The upper $1\cdot\sigma$ confidence interval for these rates is $1\times10^{-15}\,\mathrm{cm}^3\,\mathrm{s}^{-1}$

steady-state spin state within several Langevin collisions Figure 5.8. The ion's spin steady-state aligns according to the Rb atoms spin state, and initial Sr^+ state preparation plays no role. From the dynamics and steady-state spin population, we were able to extract both spin-exchange and spin-relaxation rates Equation 5.11 and Equation 5.12. The spin-exchange rate shows a significant deviation from random-phase approximation Figure 5.3. This is an indication of quantum behavior with several partial waves contributing to scattering. Another indication for quantumness of spin-exchange is the strong sensitivity of DIS approximation calculations of the spin-exchange cross-section Figure 5.5. By tuning the PEC, we demonstrated that spin-exchange cross-section periodically oscillates between 0 and maximum value, where maximum corresponds to $\sin^2(\Delta\eta_l) = 1$.

Besides the collisional spin-pumping, we measured the dependence of the charge-exchange reaction rate on the atomic spin and found it to be in good agreement with simple theoretical predictions Figure 5.12, where the reaction rate should be proportional to the overlap with triplet state Equation 5.14.

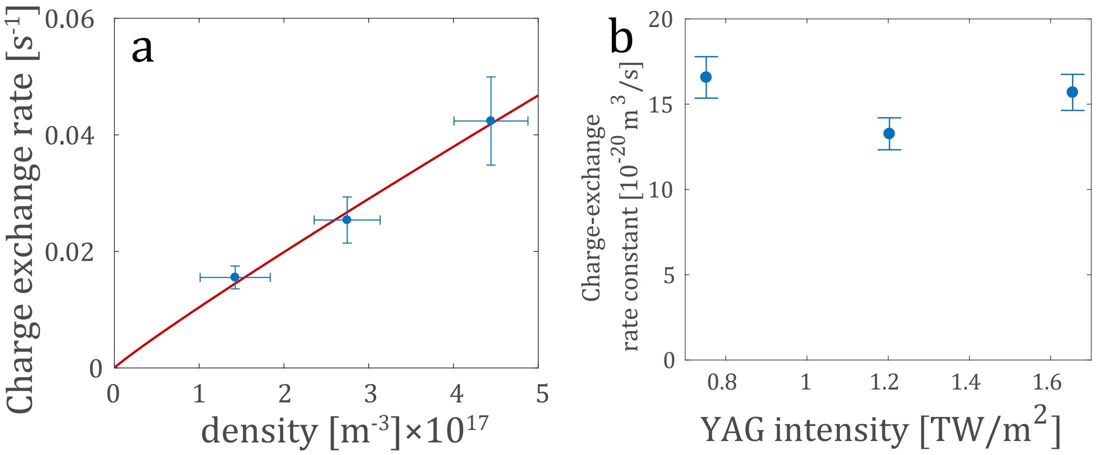

Figure 5.13: a) Density dependence of the charge-exchange rate averaged for $|1,0\rangle_{\mathrm{Rb}}$ and $|1,-1\rangle_{\mathrm{Rb}}$. From a fit to a power-law we estimate the charge-exchange scaling on the density to be $k_{CE} \propto \rho^{0.94(8)}$. b) Charge-exchange cross-section at various YAG laser intensities for atoms prepared in a $|1,-1\rangle_{\mathrm{Rb}}$ state. Error bars represent $1 \cdot \sigma$ deviation.

Chapter 6

Summary and outlook

This thesis outlines the experimental apparatus and summarizes the dynamics of Sr^+ ion interacting with ultracold atoms. The non-equilibrium dynamics was extensively described in the thesis of Ziv Meir. In this thesis, we thoroughly described the Doppler thermometry. The existing 2-level model was limited to only excess micromotion in the strong or weak binding limits [71]. Our extension includes multilevel Doppler cooling transitions and also both inherent and excess micromotion in an intermediate regime (timescale of the density matrix population Equation 4.16 comparable to the micromotion timescale) subsection 4.4.1. This is very useful because most of the trapped atomic ions worldwide involve multiple levels Doppler cooling schemes and also micromotion is very often in an intermediate regime.

The main topic of this thesis is spin dynamics, and it's applications. Demonstration of collisional pumping of Sr^+ Zeeman spin state with spin-polarized Rb atoms. While spin-pumping is not a very practical method, because optical pumping methods with either narrow-laser or circularly polarized light are superior. However collisional spin-pumping has the advantage that atoms stay in the electronic ground state (S). This is useful for example when multiple collisions of Sr^+ with Rb occur during which we want both species to be in the ground state. We demonstrated the usefulness of this effect where we performed multiple consecutive collisions with both atom and ion in the electronic ground state and monitored the charge-exchange chemical reactions. We demonstrated that we could control the rate of these reactions by spin-manipulation.

In this thesis, we already demonstrated the effect of the hyperfine and Zeeman barrier on the spin-exchange dynamics. We have demonstrated that hyperfine barrier (328 mK) completely shuts down endoenergetic channels. The Zeeman barrier which is (1.5 mK) for B=3 Gauss only decreases the rate. For higher magnetic field B=9.61 Gauss (see Figure 5.9). In future, we plan to increase the magnetic field by about an order magnitude. In this way, we could freeze the spin state of an Sr^+ ion during an atom-ion collision. Since the spin-relaxation for the F=1 state is small due to weak spin-orbit coupling, we can study the coherent effects of atom-ion on Sr^+ spin state by performing Ramsey spectroscopy with collisions during free precession time.

The future experiments on ultracold Sr^+/Rb mixture can take several avenues. For example, we can reduce the collisional heating of the ion by reducing the atomic cloud size. This would suppress the collision rate away from the rf null point and might reduce the heating. We are also trying to optimize the trap parameters to lower the heating rate. However, preliminary results show that collisional heating rate depends on a, q parameters weakly. Other experimental groups are pursuing using lighter atoms [36] or trapping ions in an optical trap during the interaction period [34].

We also study collisions of Sr^+ ion in the excited metastable D-state. We are investigating quench rates of the ion from the metastable state due to collisions with atoms. We observed that an energy release of 1500 K follows the quench. The energy release can be explained by a non-adiabatic excitation-exchange $\mathrm{Sr}^+(D)+\mathrm{Rb}(S)\leftarrow\mathrm{Sr}^+(S)+\mathrm{Rb}(P)$. We also plant o study the dependence of the quench spin states.

While so far we studied the spin-dynamics with ions in a power law energy distribution. In future, we plan to measure the dependence of the spin-exchange cross-section on the energy by limiting experiments to a single collision. We can change the collision energy between the atoms and the ion by sweeping the atomic cloud through the ground-state cooled ion at a specific velocity in a 1D optical lattice. If the density and interaction time are such that in every sweep there will be a negligible probability for more than one collision, then the collisional energy of the first collision will be fully determined by the 1D optical lattice velocity.

Bibliography

[1] O. Abah, J. Roßnagel, G. Jacob, S. Deffner, F. Schmidt-Kaler, K. Singer, and E. Lutz. Single-ion heat engine at maximum power. *Physical Review Letters*, 109(20), 2012.

[2] D. T. C. Allcock, J. A. Sherman, D. N. Stacey, A. H. Burrell, M. J. Curtis, G. Imreh, N. M. Linke, D. J. Szwer, S. C. Webster, A. M. Steane, and D. M. Lucas. Implementation of a symmetric surface-electrode ion trap with field compensation using a modulated Raman effect. *New Journal of Physics*, 12, 2010.

[3] M. H. Anderson, J. R. Ensher, M. R. Matthews, C. E. Wieman, and E. A. Cornell. Observation of Bose-Einstein Condensation in a Dilute Atomic Vapor. *Science*, 269(5221):198–201, 1995.

[4] M. Aymar, R. Guérout, and O. Dulieu. Structure of the alkali-metal-atom strontium molecular ions: Towards photoassociation and formation of cold molecular ions. *Journal of Chemical Physics*, 135(6):064305, 2011.

[5] D. J. Berkeland, J. D. Miller, J. C. Bergquist, W. M. Itano, and D. J. Wineland. Minimization of ion micromotion in a Paul trap. *Journal of Applied Physics*, 83(10):5025–5033, 1998.

[6] U. Bissbort, D. Cocks, A. Negretti, Z. Idziaszek, T. Calarco, F. Schmidt-Kaler, W. Hofstetter, and R. Gerritsma. Emulating solid-state physics with a hybrid system of ultracold ions and atoms. *Physical Review Letters*, 111(8):080501, 2013.

[7] R. B. Blakestad, C. Ospelkaus, A. P. Vandevender, J. M. Amini, J. Britton, D. Leibfried, and D. J. Wineland. High-fidelity transport of trapped-ion qubits through an X-junction trap array. *Physical Review Letters*, 102(15), 2009.

[8] M. Cetina, A. T. Grier, and V. Vuletić. Micromotion-induced limit to atom-ion sympathetic cooling in Paul traps. *Physical Review Letters*, 109(25):253201, 2012.

[9] K. Chen, S. T. Sullivan, and E. R. Hudson. Neutral Gas Sympathetic Cooling of an Ion in a Paul Trap. *Physical Review Letters*, 112(14):143009, 2014.

[10] C. Chin, R. Grimm, P. Julienne, and E. Tiesinga. Feshbach resonances in ultracold gases. *Reviews of Modern Physics*, 82(2):1225–1286, 2010.

[11] J. Cizek. On the Correlation Problem in Atomic and Molecular Systems. Calculation of Wavefunction Components in Ursell-Type Expansion Using Quantum-Field Theoretical Methods. *The Journal of Chemical Physics*, 45(11):4256, 1966.

[12] R. Côté and A. Dalgarno. Ultracold atom-ion collisions. *Physical Review A - Atomic, Molecular, and Optical Physics*, 62(1):6, 2000.

[13] R. Côté, V. Kharchenko, and M. D. Lukin. Mesoscopic Molecular Ions in Bose-Einstein Condensates. *Physical Review Letters*, 89(9), 2002.

[14] H. Da Silva, M. Raoult, M. Aymar, and O. Dulieu. Formation of molecular ions by radiative association of cold trapped atoms and ions. *New Journal of Physics*, 17, 2015.

[15] A. Dalgarno. Spin-Change Cross-Sections. *Proceedings of the Royal Society of London. Series A. Mathematical and Physical Sciences*, 262(1308):132–135, 1961.

[16] a. Dalgarno, M. R. C. McDowell, and a. Williams. The Mobilities of Ions in Unlike Gases. *Philosophical Transactions of the Royal Society A: Mathematical, Physical and Engineering Sciences*, 250(April):411–425, 1958.

[17] N. Daniilidis, S. Narayanan, S. A. Möller, R. Clark, T. E. Lee, P. J. Leek, A. Wallraff, S. Schulz, F. Schmidt-Kaler, and H. Häffner. Fabrication and heating rate study of microscopic surface electrode ion traps. *New Journal of Physics*, 13, 2011.

[18] H. Dehmelt. Experiments with an Isolated Subatomic Particle at Rest (Nobel Lecture), 1990.

[19] H. G. Dehmelt and F. L. Walls. "bolometric" technique for the rf spectroscopy of stored ions. *Physical Review Letters*, 21(3):127–131, 1968.

[20] R. G. DeVoe. Power-law distributions for a trapped ion interacting with a classical buffer gas. *Physical Review Letters*, 102(6), 2009.

[21] H. Doerk, Z. Idziaszek, and T. Calarco. Atom-ion quantum gate. *Physical Review A - Atomic, Molecular, and Optical Physics*, 81(1):012708, 2010.

[22] R. J. Epstein, S. Seidelin, D. Leibfried, J. H. Wesenberg, J. J. Bollinger, J. M. Amini, R. B. Blakestad, J. Britton, J. P. Home, W. M. Itano, J. D. Jost, E. Knill, C. Langer, R. Ozeri, N. Shiga, and D. J. Wineland. Simplified motional heating rate measurements of trapped ions. *Physical Review A - Atomic, Molecular, and Optical Physics*, 76(3), 2007.

[23] H. Fürst, T. Feldker, N. V. Ewald, J. Joger, M. Tomza, and R. Gerritsma. Dynamics of a single ion spin impurity in a spin-polarized atomic bath. *arXiv preprint arXiv:1712.07873*, 2017.

[24] J. J. García-Ripoll, P. Zoller, and J. I. Cirac. Quantum information processing with cold atoms and trapped ions. *Journal of Physics B: Atomic, Molecular and Optical Physics*, 38(9), 2005.

[25] R. Gerritsma, A. Negretti, H. Doerk, Z. Idziaszek, T. Calarco, and F. Schmidt-Kaler. Bosonic Josephson junction controlled by a single trapped ion. *Physical Review Letters*, 109(8), 2012.

[26] A. T. Grier, Marko, F. Orusevic, and V. Vuletic. Observation of cold collisions between trapped ions and trapped atoms. *PhysicalCetina Review Letters*, 102(22):223201, 2009.

[27] H. Häffner, C. F. Roos, and R. Blatt. Quantum computing with trapped ions. *Physics Reports*, 469(4):155–203, 2008.

[28] F. H. J. Hall, M. Aymar, N. Bouloufa-Maafa, O. Dulieu, and S. Willitsch. Light-assisted ion-neutral reactive processes in the cold regime: Radiative molecule formation versus charge exchange. *Physical Review Letters*, 107(24):243202, dec 2011.

[29] T. W. Hänsch and A. L. Schawlow. Cooling of gases by laser radiation. *Optics Communications*, 13(1):68–69, 1975.

[30] A. Härter and J. Hecker Denschlag. Cold atom-ion experiments in hybrid traps. *Contemporary Physics*, 55(1):33–45, 2014.

[31] A. Härter, A. Krükow, A. Brunner, W. Schnitzler, S. Schmid, and J. H. Denschlag. Single ion as a three-body reaction center in an ultracold atomic gas. *Physical Review Letters*, 109(12), 2012.

[32] S. Haze, R. Saito, M. Fujinaga, and T. Mukaiyama. Charge-exchange collisions between ultracold fermionic lithium atoms and calcium ions. *Physical Review A - Atomic, Molecular, and Optical Physics*, 91(3), 2015.

[33] G. Huber, T. Deuschle, W. Schnitzler, R. Reichle, K. Singer, and F. Schmidt-Kaler. Transport of ions in a segmented linear Paul trap in printed-circuit-board technology. *New Journal of Physics*, 10, 2008.

[34] T. Huber, A. Lambrecht, J. Schmidt, L. Karpa, and T. Schaetz. A far-off-resonance optical trap for a Ba + ion. *Nature Communications*, 5, 2014.

[35] N. Huntemann, C. Sanner, B. Lipphardt, C. Tamm, and E. Peik. Single-Ion Atomic Clock with 310-18 Systematic Uncertainty. *Physical Review Letters*, 116(6):063001, 2016.

[36] J. Joger, H. Fürst, N. Ewald, T. Feldker, M. Tomza, and R. Gerritsma. Observation of collisions between cold Li atoms and Yb+ ions. *Physical Review A*, 96(3), 2017.

[37] B. R. Johnson. New numerical methods applied to solving the one-dimensional eigenvalue problem. *The Journal of Chemical Physics*, 67(9):4086, 1977.

[38] K. M. Jones, E. Tiesinga, P. D. Lett, and P. S. Julienne. Ultracold photoassociation spectroscopy: Long-range molecules and atomic scattering. *Reviews of Modern Physics*, 78(2):483–535, 2006.

[39] R. E. Langer. On the connection formulas and the solutions of the wave equation. *Physical Review*, 51(8):669–676, 1937.

[40] D. Leibfried, R. Blatt, C. Monroe, and D. Wineland. Quantum dynamics of single trapped ions, 2003.

[41] V. S. Letokhov, V. G. Minogin, and B. D. Pavlik. Cooling and trapping of atoms and molecules by a resonant laser field. *Optics Communications*, 19(1):72–75, 1976.

[42] F. Major and H. G. Dehmelt. Exchange-Collision Technique for the rf Spectroscopy of Stored Ions. *Physical Review*, 1:91–107, 1968.

[43] Z. Meir, M. Pinkas, T. Sikorsky, R. Ben-shlomi, N. Akerman, and R. Ozeri. Direct observation of atom-ion non-equilibrium sympathetic cooling. *arXiv preprint arXiv:1801.06839*, 2018.

[44] Z. Meir, T. Sikorsky, N. Akerman, R. Ben-shlomi, M. Pinkas, and R. Ozeri. Single-shot energy measurement of a single atom and the direct reconstruction of its energy distribution. *Physical Review A*, 96(2):020701, aug 2017.

[45] Z. Meir, T. Sikorsky, R. Ben-Shlomi, N. Akerman, Y. Dallal, and R. Ozeri. Dynamics of a Ground-State Cooled Ion Colliding with Ultracold Atoms. *Physical Review Letters*, 117(24), 2016.

[46] Z. Meir, T. Sikorsky, R. Ben-shlomi, N. Akerman, M. Pinkas, Y. Dallal, and R. Ozeri. Experimental apparatus for overlapping a ground-state cooled ion with ultracold atoms, 2018.

[47] F. Mies, C. Williams, P. Julienne, and M. Krauss. Estimating bounds on collisional relaxation rates of spin-polarized 87Rb atoms at ultracold temperatures. *Journal of Research of the National Institute of Standards and Technology*, 101(4):521, 1996.

[48] T. Monz, P. Schindler, J. T. Barreiro, M. Chwalla, D. Nigg, W. A. Coish, M. Harlander, W. Hänsel, M. Hennrich, and R. Blatt. 14-qubit entanglement: Creation and coherence. *Physical Review Letters*, 106(13), 2011.

[49] W. Neuhauser, M. Hohenstatt, P. Toschek, and H. Dehmelt. Optical-sideband cooling of visible atom cloud confined in parabolic well. *Physical Review Letters*, 41(4):233–236, 1978.

[50] H. R. Noh and W. Jhe. Analytic solutions of the optical Bloch equations. *Optics Communications*, 283(11):2353–2355, 2010.

[51] H. Oberst. *Resonance fluorescence of single barium ions.* thesis, Universität Hamburg, 1999.

[52] S. Ospelkaus, K. K. Ni, D. Wang, M. H. De Miranda, B. Neyenhuis, G. Quéméner, P. S. Julienne, J. L. Bohn, D. S. Jin, and J. Ye. Quantum-state controlled chemical reactions of ultracold potassium-rubidium molecules. *Science*, 327(5967):853–857, 2010.

[53] W. Paul. Electromagnetic traps for charged and neutral particles. *Reviews of Modern Physics*, 62(3):531–540, 1990.

[54] W. Paul and H. Steinwedel. Ein neues Massenspektrometer ohne Magnetfeld, 1953.

[55] L. Ratschbacher, C. Sias, L. Carcagni, J. M. Silver, C. Zipkes, and M. Köhl. Decoherence of a single-ion qubit immersed in a spin-polarized atomic bath. *Physical Review Letters*, 110(16):160402, 2013.

[56] L. Ratschbacher, C. Zipkes, C. Sias, and M. Köhl. Controlling chemical reactions of a single particle. *Nature Physics*, 8(9):649–652, 2012.

[57] K. Ravi, S. Lee, A. Sharma, G. Werth, and S. A. Rangwala. Cooling and stabilization by collisions in a mixed ion-atom system. *Nature Communications*, 3, 2012.

[58] W. G. Rellergert, S. T. Sullivan, S. Kotochigova, A. Petrov, K. Chen, S. J. Schowalter, and E. R. Hudson. Measurement of a large chemical reaction rate between ultracold closed-shell 40Ca atoms and open-shell 174Yb+ ions held in a hybrid atom-ion trap. *Phys. Rev. Lett.*, 107(24):243201, dec 2011.

[59] I. Rouse and S. Willitsch. Superstatistical Energy Distributions of an Ion in an Ultracold Buffer Gas. *Physical Review Letters*, 118(14), 2017.

[60] S. Schmid, A. Härter, and J. H. Denschlag. Dynamics of a cold trapped ion in a Bose-Einstein condensate. *Physical Review Letters*, 105(13):133202, 2010.

[61] S. J. Schowalter, A. J. Dunning, K. Chen, P. Puri, C. Schneider, and E. R. Hudson. Blue-sky bifurcation of ion energies and the limits of neutral-gas sympathetic cooling of trapped ions. *Nature Communications*, 7, 2016.

[62] S. Schwarz. Simulations for ion traps - Buffer gas cooling. *Lecture Notes in Physics*, 749:97–117, 2008.

[63] T. Sikorsky, Z. Meir, N. Akerman, R. Ben-shlomi, and R. Ozeri. Doppler cooling thermometry of a multilevel ion in the presence of micromotion. *Physical Review A*, 96(1):012519, jul 2017.

[64] T. Sikorsky, Z. Meir, R. Ben-shlomi, N. Akerman, and R. Ozeri. Spin-controlled atomion chemistry. *Nature Communications*, 9(1):920, 2018.

[65] T. Sikorsky, M. Morita, Z. Meir, A. Buchachenko, R. Ben-shlomi, N. Akerman, E. Narevicius, T. Tscherbul, and R. Ozeri. Phase-locking between different partial-waves in atom-ion spin-exchange collisions.

[66] M. Steiner, H. M. Meyer, C. Deutsch, J. Reichel, and M. K??hl. Single ion coupled to an optical fiber cavity. *Physical Review Letters*, 110(4), 2013.

[67] M. Tomza, C. P. Koch, and R. Moszynski. Cold interactions between an Yb+ ion and a Li atom: Prospects for sympathetic cooling, radiative association, and Feshbach resonances. *Physical Review A - Atomic, Molecular, and Optical Physics*, 91(4), 2015.

[68] T. V. Tscherbul, P. Brumer, and A. A. Buchachenko. Spin-Orbit Interactions and Quantum Spin Dynamics in Cold Ion-Atom Collisions. *Phys. Rev. Lett.*, 117(14):143201, sep 2016.

[69] A. Walther, F. Ziesel, T. Ruster, S. T. Dawkins, K. Ott, M. Hettrich, K. Singer, F. Schmidt-Kaler, and U. Poschinger. Controlling fast transport of cold trapped ions. *Physical Review Letters*, 109(8), 2012.

[70] D. S. Weiss, B. C. Young, and S. Chu. Precision measurement of the photon recoil of an atom using atomic interferometry. *Physical Review Letters*, 70(18):2706–2709, 1993.

[71] J. H. Wesenberg, R. J. Epstein, D. Leibfried, R. B. Blakestad, J. Britton, J. P. Home, W. M. Itano, J. D. Jost, E. Knill, C. Langer, R. Ozeri, S. Seidelin, and D. J. Wineland. Fluorescence during Doppler cooling of a single trapped atom. *Physical Review A - Atomic, Molecular, and Optical Physics*, 76(5), 2007.

[72] R. Wester. Radiofrequency multipole traps: Tools for spectroscopy and dynamics of cold molecular ions. *Journal of Physics B: Atomic, Molecular and Optical Physics*, 42(15), 2009.

[73] W. Williams and M. Saffman. Two-dimensional atomic lithography by submicrometer focusing of atomic beams. *Journal of the Optical Society of America B*, 23(6):1161, 2006.

[74] D. J. Wineland and H. Dehmelt. "Proposed 1014 delta upsilon less than upsilon laser fluorescence spectroscopy on t1+ mono-ion oscillator iii.". *Bulletin of the American Physical Society*, 20(4), 1975.

[75] D. J. Wineland, R. E. Drullinger, and F. L. Walls. Radiation-pressure cooling of bound resonant absorbers. *Physical Review Letters*, 40(25):1639–1642, 1978.

[76] D. J. Wineland, C. Monroe, W. M. Itano, D. Leibfried, B. E. King, and D. M. Meekhof. Experimental issues in coherent quantum-state manipulation of trapped atomic ions. *Journal of Research of the National Institute of Standards and Technology*, 103(3):259, 1998.

[77] H. Zhang, M. Gutierrez, G. H. Low, R. Rines, J. Stuart, T. Wu, I. Chuang, S. U, S. M. Jiang D, Arora B, C. C. W, G. C. W, Johnson, F. N, D. V. V, Flambaum, D. N. N. S, Majumder, K. S. O. L. O. E. S. N. L. H. G. Caffau E, Andrievsky S, B. P, H. T. et Al, J. S. G. L. D. S. Brage T, Wahlgren G M, P. C. R, I. K. H. H. Bautista M, Gull T, D. K, G. R. C, Sneden, B. B. S. M. S. F. Siqueira-Mello C, Andrievsky S, K. S, B. M. Bergemann M, Hansen C, R. G, Y. J. P. E. Ludlow A D, Boyd M M, S. P. O, Z. Z. B. J. E. Madej A A, Dubé P, G. M, N. N. L. R. Weyers S, Gerginov V, G. K, T. M.

Dubé P, Madej A A, B. J. E, G. A, K. M. T. I. Ramm M, Pruttivarasin T, H. H, G. S. Likforman J P, Tugayé V, G. L, Z. F. B. J. B. R. Gerritsma R, Kirchmair G, R. C, R. R. De Munshi D, Dutta T, M. M, K. H. R. C. S. C. S.-K. F. Hettrich M, Ruster T, P. U, M. E. A. B. M. F. S. P. R. R. W. S. X. C. I. L. Monz T, Nigg D, B. R, S. G. B. R. S. J. M. V. Kurz N, Dietrich M, B. B, D. B. C. R. Sahoo B, Islam M R, M. D, P. T, C. C. et Al, B. D. M, Boshier, G. A. A, Lurio, F. U. H, M. J, M. C. P, Siegel, H. M. R. W. S. R. Auchter C, Noel T W, B. B. B, S. M. U, Safronova, S. U. M, Safronova, B. R. Pinnington E, L. M, O. W. et Al, L. B. T. C. Huntemann N, Sanner C, and P. E. Iterative precision measurement of branching ratios applied to 5 <i>P</i> states in ⁸⁸ Sr ⁺. *New Journal of Physics*, 18(12):123021, dec 2016.

[78] C. Zipkes, S. Palzer, L. Ratschbacher, C. Sias, and M. K??hl. Cold heteronuclear atom-ion collisions. *Physical Review Letters*, 105(13), 2010.

[79] C. Zipkes, S. Palzer, C. Sias, and M. Köhl. A trapped single ion inside a Bose-Einstein condensate. *Nature*, 464(7287):388–391, 2010.

[80] C. Zipkes, L. Ratschbacher, C. Sias, and M. Kohl. Kinetics of a single trapped ion in an ultracold buffer gas. *New Journal of Physics*, 13, 2011.